

# **Field and Model Investigations of Freshwater Lenses in Coastal Aquifers**

**Pieter S. Pauw**

# **Field and Model Investigations of Freshwater Lenses in Coastal Aquifers**

**Pieter S. Pauw**

## **Thesis committee**

### **Promotor**

Prof. Dr S.E.A.T.M. van der Zee  
Personal chair Ecohydrology  
Wageningen University

### **Co-promotors**

Dr G.H.P. Oude Essink  
Associate professor, Department of Physical Geography  
Utrecht University

Prof. Dr A. Leijnse  
Professor, Soil Physics and Land Management Group  
Wageningen University

### **Other members**

Prof. Dr J. Molenaar, Wageningen University  
Prof. Dr M.Th. van Genuchten, Federal University of Rio de Janeiro, Brazil  
Prof. Dr S.M. Hassanizadeh, Utrecht University  
Prof. Dr T.N. Olsthoorn, Delft University of Technology

This research was conducted under the auspices of the Graduate School for Socio-Economic and Natural Sciences of the Environment (SENSE)

# Field and Model Investigations of Freshwater Lenses in Coastal Aquifers

**Pieter S. Pauw**

## **Thesis**

submitted in fulfilment of the requirements for the degree of doctor  
at Wageningen University  
by the authority of the Academic Board,  
in the presence of the  
Thesis Committee appointed by the Academic Board  
to be defended in public  
on Monday 8 June 2015  
at 4 p.m. in the Aula.

Pieter S. Pauw  
Field and Model Investigations of Freshwater Lenses in Coastal Aquifers,  
159 pages.

PhD thesis, Wageningen University, Wageningen, NL (2015)  
With references, with summary in English

ISBN 978-94-6257-292-8

# Contents

|          |   |           |
|----------|---|-----------|
| <b>1</b> | <b>Introduction</b>   | <b>1</b>  |
| 1.1      | Freshwater lenses, from concept to reality . . . . .                          | 1         |
| 1.2      | Motivation and general objectives of this thesis . . . . .                    | 4         |
| 1.3      | Focus and outline . . . . .   | 5         |
| 1.3.1    | Chapter 2 . . . . .   | 5         |
| 1.3.2    | Chapter 3 . . . . .   | 6         |
| 1.3.3    | Chapter 4 . . . . .   | 8         |
| 1.3.4    | Chapter 5 . . . . .   | 9         |
| <b>2</b> | <b>Low-resolution modeling of dense drainage networks in confining layers</b> | <b>11</b> |
| 2.1      | Introduction . . . . .  | 11        |
| 2.2      | Material and methods . . . . .  | 14        |
| 2.2.1    | Conductance expressions . . . . .   | 14        |
| 2.2.2    | Grid resolution comparison . . . . .  | 17        |
| 2.2.3    | Base comparison . . . . .   | 17        |
| 2.2.4    | Influence of variable groundwater density . . . . .                           | 19        |
| 2.2.5    | Influence of vertical discretization . . . . .                                | 20        |
| 2.2.6    | Simulation of ditches and drain tiles . . . . .                               | 20        |
| 2.2.7    | Salt load to the ditches and drain tiles . . . . .                            | 20        |
| 2.3      | Results . . . . .   | 21        |
| 2.3.1    | Base comparison . . . . .   | 21        |
| 2.3.2    | Variable groundwater density . . . . .  | 23        |
| 2.3.3    | Vertical discretization . . . . .   | 24        |
| 2.3.4    | Simulation of ditches and drain tiles . . . . .                               | 25        |
| 2.3.5    | Salt loads toward the ditches and drain tiles . . . . .                       | 26        |
| 2.4      | Discussion . . . . .  | 27        |
| 2.4.1    | Conductance expressions . . . . .   | 27        |
| 2.4.2    | Limitations and generic applicability of $C_{DL}$ . . . . .                   | 28        |
| 2.5      | Conclusions . . . . .   | 30        |
| 2.6      | Appendix . . . . .  | 31        |

|          |  |           |
|----------|--|-----------|
| <b>3</b> | <b>Increasing a freshwater lens below a creek ridge using a controlled artificial recharge and drainage system: a case study in the Netherlands.</b> | <b>35</b> |
| 3.1      | Introduction . . . . .   | 35        |
| 3.1.1    | Hydrogeology of the Walcheren peninsula . . . . .  | 35        |
| 3.1.2    | Freshwater lenses below creek ridges . . . . .   | 36        |
| 3.2      | Material and methods . . . . .   | 38        |
| 3.2.1    | Theory and definitions . . . . .   | 38        |
| 3.2.2    | Design of the CARD system at the study area . . . . .  | 38        |
| 3.2.3    | Field measurements . . . . .   | 40        |
| 3.2.4    | Monitoring . . . . .   | 41        |
| 3.2.5    | Numerical model . . . . .  | 43        |
| 3.3      | Results . . . . .  | 46        |
| 3.3.1    | Field measurements . . . . .   | 46        |
| 3.3.2    | Numerical simulations . . . . .  | 52        |
| 3.4      | Discussion . . . . .   | 58        |
| 3.5      | Conclusions . . . . .  | 59        |
| 3.6      | Appendix . . . . .   | 60        |
| 3.6.1    | Additional information of the CARD system . . . . .  | 60        |
| 3.6.2    | Numerical simulation of drainage and infiltration by drain tiles and ditches using the DRAIN and RIVER packages . . . . .                            | 62        |
| 3.6.3    | Simulation of the CARD system in the scenario simulations . . . . .  | 63        |
| 3.6.4    | Additional results of the comparison between the CPTs and the initialization simulation with the optimized groundwater recharge . . . . .            | 65        |
| 3.6.5    | Results of scenarios B and C . . . . .   | 66        |
| <b>4</b> | <b>Saltwater upconing due to cyclic pumping by finite horizontal wells in freshwater lenses</b>  | <b>69</b> |
| 4.1      | Introduction . . . . .   | 69        |
| 4.2      | Material and methods . . . . .   | 71        |
| 4.2.1    | Two-dimensional (2D) and three-dimensional (3D) conceptual models . . . . .  | 71        |
| 4.2.2    | Cyclic pumping (2D conceptual model) . . . . .   | 71        |
| 4.2.3    | Dispersion (2D conceptual model) . . . . .   | 75        |
| 4.2.4    | Horizontal wells with a finite length in a finite domain (3D conceptual model) . . . . .   | 77        |
| 4.3      | Results . . . . .  | 81        |
| 4.3.1    | Groundwater flow patterns and mixing in the 2D numerical simulation with the reference values . . . . .  | 81        |
| 4.3.2    | Cyclic pumping (2D conceptual model) . . . . .   | 84        |
| 4.3.3    | Dispersion (2D conceptual model) . . . . .   | 85        |
| 4.3.4    | Horizontal wells with a finite length in a finite domain (3D conceptual model) . . . . .   | 89        |
| 4.4      | Discussion and conclusions . . . . .   | 93        |
| 4.4.1    | Accuracy aspects . . . . .   | 93        |

|          |  |            |
|----------|--|------------|
| 4.4.2    | Considerations for applying the analytical solutions in practice                                 | 95         |
| 4.5      | Appendix : Parameter variations in the 2D model concept . . . . .                                | 96         |
| <b>5</b> | <b>Regional scale impact of tidal forcing on groundwater flow in unconfined coastal aquifers</b> | <b>99</b>  |
| 5.1      | Introduction . . . . .   | 99         |
| 5.2      | Material and methods . . . . .   | 103        |
| 5.2.1    | SEAWAT . . . . .   | 103        |
| 5.2.2    | Boundary conditions . . . . .  | 103        |
| 5.2.3    | Constant model parameters . . . . .  | 107        |
| 5.2.4    | Freshwater lens in the deep aquifer . . . . .  | 107        |
| 5.2.5    | Freshwater lens in the shallow aquifer . . . . .   | 110        |
| 5.2.6    | Freshwater lens in the heterogeneous subsurface . . . . .  | 112        |
| 5.3      | Results . . . . .  | 113        |
| 5.3.1    | Validation of the step-wise approach . . . . .   | 113        |
| 5.3.2    | Freshwater lens in the deep aquifer . . . . .  | 115        |
| 5.3.3    | Freshwater lens in the shallow aquifer . . . . .   | 120        |
| 5.3.4    | Freshwater lens in the heterogeneous subsurface . . . . .  | 122        |
| 5.4      | Discussion . . . . .   | 124        |
| 5.5      | Summary and conclusions . . . . .  | 126        |
| 5.6      | Appendix . . . . .   | 126        |
| <b>6</b> | <b>Discussion</b>  | <b>129</b> |
| 6.1      | Modeling of freshwater lenses . . . . .  | 129        |
| 6.1.1    | Application of groundwater models . . . . .  | 129        |
| 6.1.2    | Examples of improved insights . . . . .  | 131        |
| 6.2      | Measures to increase freshwater supply . . . . .   | 134        |
| 6.2.1    | Example of improved insight . . . . .  | 134        |
| 6.2.2    | Additional insights . . . . .  | 135        |
| 6.3      | Recommendations for future studies . . . . .   | 136        |
| <b>7</b> | <b>English summary</b>   | <b>139</b> |
|          | <b>Na- en dankwoord</b>  | <b>143</b> |
|          | <b>Bibliography</b>  | <b>147</b> |



# Chapter 1

## Introduction

### 1.1 Freshwater lenses, from concept to reality

Freshwater lenses are convex bodies of fresh groundwater that are underlain by groundwater with a significant higher salinity. In coastal areas, freshwater lenses are of vital importance for ecosystems and freshwater supply (Custodio and Bruggeman, 1987; FAO, 1997). A sound understanding of freshwater lenses is essential for a proper management of these systems. Before the relevance of understanding freshwater lenses is further discussed, some basic insights are first introduced here.

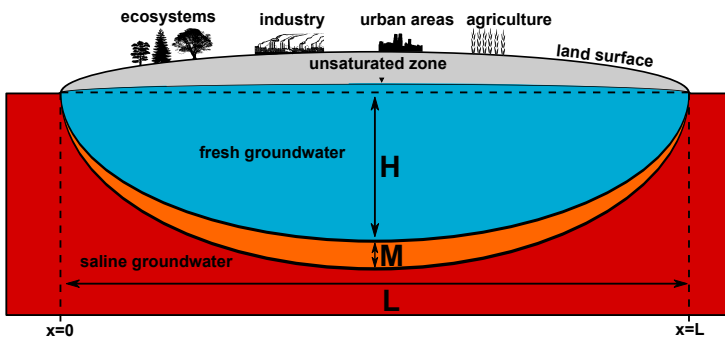


Figure 1.1: Concept of a freshwater lens in vertical cross section. The lens terminates on the left ( $x = 0$ ) and right ( $x = L$ ) at a draining feature (a stream, a canal, or a marine water). The dashed line indicates a reference level, such as mean sea level.

In Figure 1.1 a concept of a freshwater lens in vertical cross section is shown.  $H$  indicates the thickness of the lens relative to a reference level (e.g., mean sea level),  $M$  is the thickness of a transition zone where the groundwater salinity increases from fresh to the maximum salinity of the ambient saline groundwater,  $x$

is the horizontal coordinate, and  $L$  is the width of the lens. In coastal aquifers, the ratio  $H/L$  is commonly lower than 0.1 (e.g., Schneider and Kruse, 2005; White and Falkland, 2009; Ataie-Ashtiani et al., 2014). Therefore, in reality (at scale) a freshwater lens appears much thinner than the lens shown in Figure 1.1. Furthermore, in large scale systems where  $L$  is larger than  $\sim 10^2$  m,  $M$  is often small compared to  $H$  (e.g., Voss and Souza, 1987; Oude Essink, 1996).

Freshwater lenses float on the underlying saline groundwater because the density of fresh groundwater is lower than the density of saline groundwater. In many coastal aquifers the density of fresh groundwater is close to  $1000 \text{ kg m}^{-3}$  and the density of saline groundwater is between  $1022$  and  $1028 \text{ kg m}^{-3}$  (Reilly and Goodman, 1985). In the classical Badon Ghijben-Herzberg principle<sup>1</sup>, where the fresh and saline groundwater are considered as two immiscible fluids in which the vertical pressure distribution is hydrostatic, the densities of fresh and saline groundwater and the thickness of the freshwater lens are related to the elevation of the groundwater table  $h$ :

$$h = \delta H. \quad (1.1)$$

$h$  and  $H$  are relative to a reference level, such as mean sea level.  $\delta$  is the relative density difference between fresh and saline groundwater:

$$\delta = \frac{\rho_s - \rho_f}{\rho_f}, \quad (1.2)$$

where  $\rho_f$  is the density of the fresh groundwater and  $\rho_s$  is the density of the saline groundwater. This principle indicates that the higher the groundwater table and the smaller the relative density difference, the thicker the freshwater lens. Furthermore, it indicates that most of the volume of a freshwater lens is situated below the reference level.

The Badon Ghijben-Herzberg principle can be combined with Darcy's law and the continuity principle to derive a one-dimensional analytical solution for the thickness of the freshwater lens (Van Dam, 1983):

$$H = \sqrt{\frac{xN(-x + L)}{\delta K(1 + \delta)}}, \quad (1.3)$$

in which  $N$  is the recharge rate and  $K$  is the homogeneous and isotropic hydraulic conductivity (Figure 1.1). This equation indicates that a high groundwater recharge, a large width of the lens, and a low hydraulic conductivity also have a positive effect on the thickness of the freshwater lens.

Although Equations 1.1 and 1.3 give important insights into the governing factors for the thickness of the freshwater lens, their application to reality is often limited. An important reason for this is that vertical hydraulic head gradients

---

<sup>1</sup>As Davis (1978) pointed out, Du Commun (1828) presented the first scientific publication on this principle, several decades before Herzberg (1901) and Drabbe and Badon Ghijben (1888).

are commonly present in coastal aquifers due to resistance to vertical flow, such that the pressure distribution in the vertical is not hydrostatic. Verruijt (1968) and later Van der Veer (1977) studied the significance of vertical hydraulic head gradients in a freshwater lens in a homogeneous aquifer. Van der Veer (1977) compared Equation 1.3 with a two-dimensional analytical solution that takes into account the resistance to vertical flow. He showed that the differences between the two expressions are small near the center of the freshwater lens as vertical flow is negligible here, but that the differences are large near the outflow zone of the freshwater lens, where vertical flow is significant due to the convergence of the streamlines.

Significant vertical hydraulic head gradients are also typically caused by low-permeable layers (Bakker, 1981). Furthermore, low-permeable layers can influence the freshwater lens in the following ways:

- *Three-dimensional groundwater flow and recharge of confined aquifers.* Stuyfzand (1993) showed that below the coastal dunes of the Netherlands, the complex spatial distribution of the low-permeable layers can lead to: 1) significant horizontal flow perpendicular to the concept shown in Figure 1.1 and 2) 'recharge focus areas', which function as a preferential pathways where groundwater flows to deeper, confined aquifers. Evidently, in these situations the groundwater flow in the freshwater lens should be considered in three dimensions rather than in two.
- *Offshore continuation of the freshwater lens.* Low-permeable layers in the nearshore and offshore regions can induce a continuation of the flow of fresh groundwater below the seabed<sup>2</sup>, instead of terminating at the shore. The continuation of the flow of fresh groundwater leads to a submarine tongue of fresh groundwater, which can extend several kilometers from the shore (Voss and Souza, 1987; Krantz et al., 2004; Mulligan et al., 2007). The length of this tongue depends amongst others on the offshore extent, coherence, and distribution of the low-permeable layers (Kooi and Groen, 2001).
- *Freshening and salinization rates.* Coastal areas, especially low-lying deltas, have been subjected to former transgressions and regressions. The reaction time of freshwater lenses (i.e., freshening and salinization rates) to these changing boundary conditions can be significantly influenced by low-permeable layers, because of their great impact on the flow patterns (Oude Essink, 1996; Post, 2003).

Other aspects that make Equations 1.1 and 1.3 hard to apply in reality and that make freshwater lenses more complex than Figure 1.1 suggests are tides (Lebbe, 1983; Nielsen, 1990), spatiotemporal variations in groundwater recharge (Ruppel et al., 2000; Houben et al., 2014), groundwater - surface water interaction

---

<sup>2</sup>Note that fresh groundwater below the seabed can also be disconnected from active groundwater flow systems (i.e., paleo groundwater) (Kooi et al., 2000; Kooi and Groen, 2003; Post et al., 2013).

(Masterson, 2004; De Louw et al., 2011), mixing (Barlow et al., 2003; Price et al., 2003), pumping (Reilly et al., 1987b; Stuyfzand, 1993), and upward groundwater flow (Maas, 2007; De Louw, 2013). These aspects are important to consider in investigations of freshwater lenses in coastal aquifers.

## **1.2 Motivation and general objectives of this thesis**

In many coastal areas, freshwater supply depends to a large extent on freshwater lenses (FAO, 1997; White and Falkland, 2009). Investigations of the sustainable exploitation of freshwater lenses are commonly aimed at quantifying, preventing or minimizing saltwater intrusion, i.e., the invasion of saline groundwater into a fresh groundwater body. Saltwater intrusion is a worldwide problem; in many coastal areas overexploitation of fresh groundwater volumes has led to well closure and reduced freshwater supply. Custodio and Bruggeman (1987) described various cases of saltwater intrusion due overexploitation, including those in the Llobregat delta (Catalonia, Spain), the coastal dune area of the Netherlands, and Mar del Plata (Province of Buenos Aires, Argentina). Barlow and Reichard (2009) described cases of saltwater intrusion in the United States of America (USA), Canada, and Mexico.

In the future, saltwater intrusion is expected to increase due to various anticipated stresses. Sea level rise has been accepted as a major contributor to saltwater intrusion (Post, 2005; Werner et al., 2013). Langevin and Zygnerski (2013) showed the effect of historical sea level rise on lateral saltwater intrusion in northern Broward County (Florida, USA). Ataie-Ashtiani et al. (2013) showed how land-surface inundation due to sea level rise can influence saltwater intrusion. In addition to sea level rise, the ongoing land subsidence in low-lying coastal deltas will likely be of major importance (Oude Essink et al., 2010; Pauw et al., 2012) for saltwater intrusion. Furthermore, climate change is expected to lead to longer periods of droughts in many coastal areas, thereby increasing the demand of fresh groundwater (Green et al., 2011).

In the Netherlands, these stresses will also have a severe impact on the fresh coastal groundwater reserves (Oude Essink et al., 2010). For this reason, a research project within the Dutch program 'Knowledge for Climate' was defined in 2010, with the following objectives:

1. To improve the insight into the modeling of freshwater lenses.
2. To define measures to increase freshwater supply from freshwater lenses.

These two objectives are also the main objectives of this thesis. In relation to these two objectives, four studies were conducted, which are presented in Chapters 2-5 of this thesis. In the remaining sections of this introduction, these four studies and their research questions are further described.

## 1.3 Focus and outline

### 1.3.1 Chapter 2

The motivation for the study that is presented in Chapter 2 is related to thin rainwater lenses. Thin rainwater lenses are found in areas where the upward flow of saline groundwater limits the downward flow of the groundwater recharge (Figure 1.2). In the Netherlands, these areas comprise the low-lying catchments around or below mean sea level where the groundwater level is artificially controlled (the so-called polders) and where saline groundwater is present within a few meters below the surface. In these polders, a confining layer often constitutes the upper hydrogeological unit.

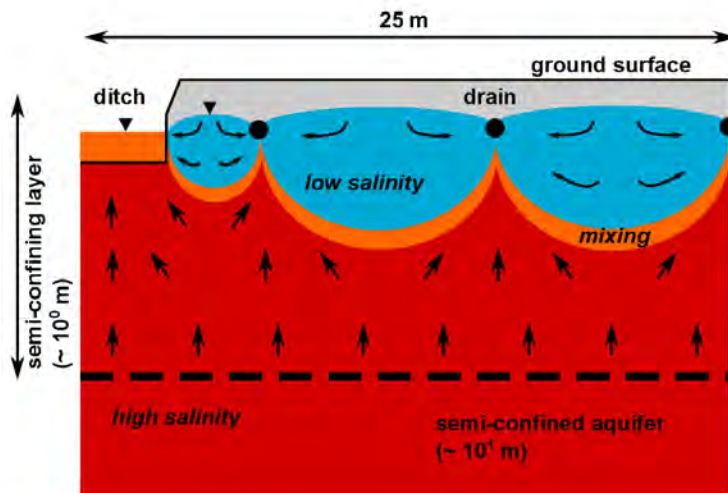


Figure 1.2: Left: Concept of thin rainwater lenses in vertical cross section. Only three agricultural drain tiles and thin rainwater lenses are shown, but in general more drain tiles are present between ditches.

Thin rainwater lenses are present between agricultural drain tiles, and are no more than a few meters thick. They have been studied thoroughly by De Louw (2013), who found amongst others that in the Netherlands, the lowest salinity in this type of lens often exceeds that of freshwater. This is caused by the mixing of the fresh rainwater with saline pore water in the unsaturated zone, resulting in brackish groundwater recharge. Therefore, the term 'rainwater lens' is used here rather than 'freshwater lens'. Thin rainwater lenses are important to study, as vegetation that depends on the limited amount of freshwater is at risk by a high salinity in the root zone, which may reduce plant growth or even cause plant death (Maas and Hoffman, 1977; Maas, 1990).

Previous related studies (Maas, 2007; De Louw et al., 2011; Eeman et al., 2011;

De Louw et al., 2013a) have considered thin rainwater lenses only on a local scale (i.e., at the scale of Figure 1.2). In the Netherlands, a practical question that followed from these local scale studies was how thin rainwater lenses will develop in the future on a larger scale, e.g., the regional scale. For such a regional scale investigation, it is important that regional scale groundwater flow is properly quantified, as it determines the upward flow of saline groundwater, which is one of the dominant processes that determine the thickness of the thin rainwater lens.

Regional scale groundwater flow in coastal aquifers is often quantified using numerical models (Cobaner et al., 2012; Faneca Sánchez et al., 2012; Langevin and Zygnerski, 2013). In such numerical models, an appropriate simulation of the upward flow of saline groundwater amongst others requires a decent simulation of the groundwater-surface water interaction. However, the simulation of GW-SW interaction is not straightforward, in particular when the grid resolution is low, as is usually the case in regional scale models. One of the difficulties lies in the parameterization of the so-called 'conductance' value of the Cauchy boundary conditions, which are generally used to simulate GW-SW interaction (Bear, 1972). Mehl and Hill (2010) indicated that so far, quantitative guidelines for determining the conductance appear to be missing in the literature, and that existing and commonly used methods can lead to significant errors in the simulation of GW-SW interaction.

Furthermore, Mehl and Hill (2010) stressed the importance of accounting for the resistance to GW-SW interaction below the surface water bed in the parameterization of the conductance in regional scale model with a low grid resolution. In Chapter 2, three conductance expressions that take this resistance into account are considered: two that were presented by Mehl and Hill (2010) and the one that was presented by De Lange (1999). The accuracy of these conductance expressions was assessed in numerical models with a low grid resolution regarding salt and water fluxes to a dense drainage network in a confined aquifer system for a wide range of hydrogeological conditions, representative for thin rainwater lenses. The research question in Chapter 2 is:

*Which of the three conductance expressions performs best in quantifying GW-SW interaction, regarding the influence of (1) variable groundwater density, (2) vertical grid discretization, and (3) simulation of both ditches and drain tiles in a single model cell?*

### **1.3.2 Chapter 3**

In the polders of the southwestern part of the Netherlands, sandy tidal creek deposits lie up to 2 meters higher than the surroundings (Figure 1.3). These geomorphological features are called creek ridges. Below the creek ridges freshwater lenses are present with a maximum thickness between 5 and 30 meters, depending mainly on the drainage (i.e., ditches and drain tiles) and the width of the creek ridge. The freshwater lenses are exploited for irrigation, but at many places

the permissible rate and amount of fresh groundwater extraction is insufficient to meet the irrigation demand during droughts, which leads to freshwater scarcity and, hence, crop damage. Moreover, these freshwater lenses are jeopardized by future stresses and increasing water demand (De Louw, 2013).

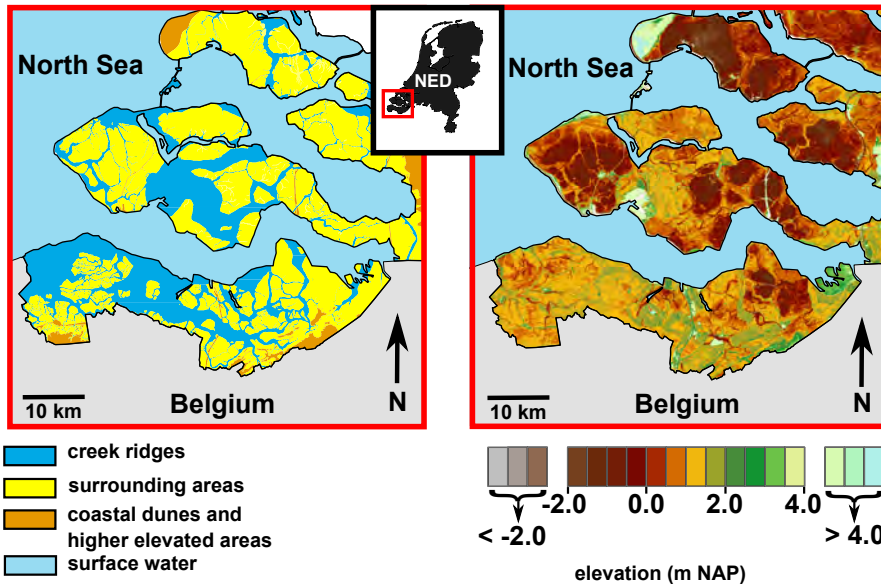


Figure 1.3: Location of creek ridges (left) and elevation (right) in the southwestern part of the Netherlands. NAP is the Dutch ordnance datum. 0 m NAP approximately corresponds with mean sea level.

Previous work on freshwater lenses below creek ridges is rather limited. In 1983, the project group 'Projektgroep Zoetwateronderzoek' started an aquifer storage and recovery (ASR) project in Kapelle, in the southwestern part of the Netherlands (Van Meerten, 1986). The goal of the project was to investigate the feasibility (both hydrologically and economically) of ASR below creek ridges using surplus fresh surface water. A vertical well was installed to infiltrate the water during winter and extract the water in summer. The results of this project indicated that the measure was not economically feasible; although the infiltration led to a significant local expansion of the freshwater lens, the infiltration was plagued by clogging problems and, therefore, high maintenance costs. Moreover, the recovery of the fresh groundwater led to a relatively fast rise of the saline groundwater, yielding a low recovery efficiency<sup>3</sup>.

Since the infiltration test of the Projektgroep Zoetwateronderzoek in the 1980's, little direct practical knowledge on freshwater lenses below creek ridges has been

<sup>3</sup>In this context the recovery efficiency can be defined as the fraction of injected freshwater that is recovered while meeting a freshwater quality criterion.

developed, although the irrigation shortage during droughts has not decreased. In Chapter 1.3, a new artificial recharge method for increasing a freshwater lens below creek ridges is presented. The method consists of a controlled drainage system, which is used for artificial recharge below the higher parts of the creek ridge and for keeping the groundwater level below the lower parts as well as higher parts of the creek ridge as high as possible. Based on the Badon Ghijben-Herzberg principle (Equation 1.1), an increase of the freshwater lens can be expected. The research question that is addressed in Chapter 1.3 is:

*Can artificial recharge using a controlled drainage system on the long term lead to a significant increase of the freshwater lens below a creek ridge?*

### 1.3.3 Chapter 4

When fresh groundwater is extracted from a freshwater lens, the underlying saline groundwater moves upward below the well screen (Figure 1.4), a process known as saltwater upconing (Dagan and Bear, 1968; Werner et al., 2009). Excessive saltwater upconing increases the risk of an undesired salinity of the extracted groundwater. In freshwater lenses the extraction of fresh groundwater using a horizontal well is often preferred over a vertical well, as a horizontal well induces less draw-down of the groundwater table per unit volume of extracted groundwater (Yeh and Chang, 2013), and therefore also less saltwater upconing.

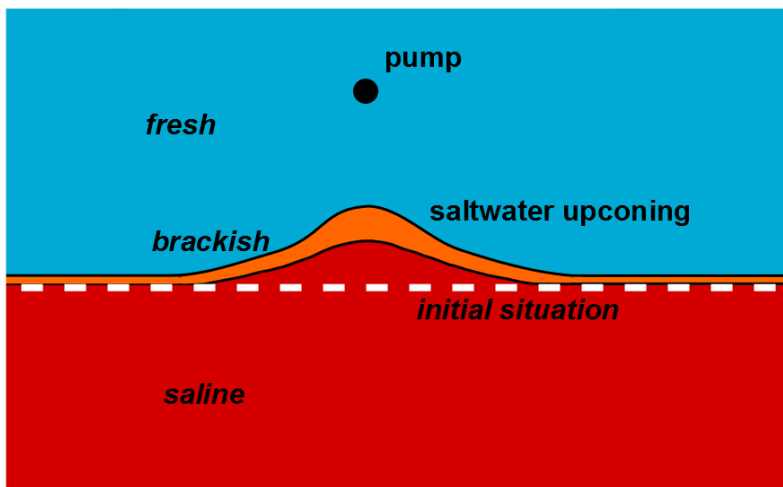


Figure 1.4: Conceptual cross section of saltwater upconing.

Saltwater upconing below horizontal wells can be quantified using analytical solutions and numerical models. The main advantage of using analytical solutions

over numerical codes is their shorter computation time, which allows for easy and fast estimation of the influence of parameters on saltwater upconing. The drawback of analytical solutions is their inability to account for complexities, such as coupled variable density groundwater flow and salt transport. In Chapter 4, the accuracy of analytical solutions for quantifying saltwater upconing below horizontal wells with a finite extent in case of cyclic pumping is assessed. The research question in Chapter 4 is:

*How accurate are analytical solutions in calculating saltwater upconing regarding 1) cyclic pumping, 2) dispersion, and 3) horizontal wells with a finite extent, in a freshwater lens of finite extent?*

### **1.3.4 Chapter 5**

Chapter 5 deals with the influence of tides on groundwater flow in an unconfined coastal aquifer. Among the previous related studies, Philip (1973) showed for the first time that in case tides influence groundwater flow in an unconfined aquifer, the inland time-averaged hydraulic heads are higher than mean sea level. Philip (1973) considered a rather unrealistic case where there is no groundwater recharge inland en where the intertidal area is vertical. His theoretical analysis was verified by Smiles and Stokes (1976) using laboratory measurements. Lebbe (1983), and later Nielsen (1990) showed that in case of a sloping intertidal area (Figure 1.5), the effect of tides on time-averaged hydraulic heads is much larger, and that the combination of tides and a sloping intertidal has a large influence on submarine groundwater discharge and the near-shore groundwater salinity distribution. Submarine groundwater discharge has gained considerable attention in the scientific literature since Moore (1996) showed its importance regarding nutrient input into marine waters (Nielsen, 1990; Vandenbohede and Lebbe, 2005; Robinson et al., 2006).

In many quantitative groundwater flow studies where tides and a sloping intertidal area have been considered, the investigation scale was in the order of the length of the intertidal area. In studies where the investigation scale is larger, the elevated time-averaged hydraulic heads in the near-shore region are often ignored, thereby accepting the underestimated hydraulic heads near the shore. When numerical models are used in such studies, the main reason for ignoring the effect of tides is to reduce the complexity and the computational effort. Instead of simulating periodic groundwater flow, a static boundary condition based on mean sea level is then often used at the land-ocean boundary.



Figure 1.5: Photo of a beach along the coast of the Netherlands, taken by the author. During ebb, the time-averaged groundwater levels in the higher part of the intertidal area (i.e., the wet part in the photo) are considerably higher than mean sea level.

However, this assumption may not only lead to underestimated hydraulic heads near the intertidal area, but also further inland. In Chapter 5 this assumption is quantitatively addressed. The research question in this chapter is:

*What is the regional scale impact of tides on groundwater flow in unconfined coastal aquifers involving a sloping intertidal area?*

## Chapter 2

# Low-resolution modeling of dense drainage networks in confining layers

This chapter is based on: *Pauw, P.S., Van der Zee, S.E.A.T.M., Leijnse, A., Delsman, J.R., De Louw, P.G.B., De Lange, W.J., and Oude Essink, G.H.P., 2014. Low-Resolution Modeling of Dense Drainage Networks in Confining Layers. Groundwater, <http://dx.doi.org/10.1111/gwat.12273>*

### 2.1 Introduction

Fresh groundwater reserves in coastal areas are jeopardized by future stresses such as sea level rise, climate change, and land subsidence (Custodio and Bruggeman, 1987; Overeem and Syvitski, 2009). These effects are often quantified using numerical models (Oude Essink et al., 2010; Cobaner et al., 2012; Faneca Sánchez et al., 2012; Langevin and Zygnerski, 2013). When investigating large-scale (more than 100 km<sup>2</sup>) problems, a low grid resolution is inevitable in view of the computational demand. A low grid resolution requires the upscaling of hydraulic parameters (Bierkens, 1994; Renard and de Marsily, 1997; Dagan et al., 2013) and boundary conditions. Vermeulen et al. (2006) showed that in case of a dense drainage network, the upscaling of hydraulic parameters is less important than the parameterization of the boundary condition that describes the groundwater-surface water (GW-SW) interaction. Appropriate simulation of GW-SW interaction in coastal areas with a dense drainage network is important for the quantification of advection in the aquifer (e.g., saltwater intrusion), salt and nutrient loads to the surface water, and for providing information for downscaled models that are used to describe local scale systems.

GW-SW interaction is generally simulated using a Cauchy boundary condition,

which is in the form of:

$$Q = (h_{sw} - h_n)C \quad (2.1)$$

where  $Q$  is the volumetric flow rate between the surface water and the aquifer [ $L^3 T^{-1}$ ],  $h_{sw}$  is the surface water level [L],  $h_n$  is the hydraulic head of the node where the Cauchy boundary condition is applied [L], and  $C$  is a coefficient [ $L^2 T^{-1}$ ], often referred to as the 'conductance'. McDonald and Harbaugh (1988) described how the conductance can be determined from the dimensions of the surface water bed (i.e., its length, width, and thickness) and its hydraulic resistance (i.e., the thickness of the bed divided by its vertical hydraulic conductivity). This approach is often adopted in groundwater flow models. However, McDonald and Harbaugh (1988) also described that this approach should only be used if the majority of the total hydraulic head loss due to GW-SW interaction occurs across the surface water bed and that the hydraulic head loss in the aquifer can be neglected. This has also been indicated in later studies (De Lange, 1998; Hunt et al., 2003; Anderson, 2005; Rushton, 2007; Mehl and Hill, 2010).

For the purpose of illustration, an example is given here to emphasize that in case of simulating a dense surface water network in a confining layer using a low model resolution, neglecting the resistance to GW-SW interaction in the confining layer leads to erroneous model results. Only the main features of this example are discussed, as similar details will be presented further in this chapter.

Figure 2.1a shows the result of a variable density groundwater flow and coupled salt transport model of a confined aquifer system in vertical cross section, using a high grid resolution (i.e., 0.1 m, both for the width of the columns and the thickness of the layers). The drainage system consists of drain tiles and shallow ditches, which were simulated using the conductance expression of McDonald and Harbaugh (1988). In this case, the conductance can be based on the resistance across the surface water bed only, as the additional resistance in the confining layer is accounted for by the high resolution grid. The streamlines show a regional flow of saline groundwater in the aquifer from the left to the right, and part of the water flows up through the 4 m thick confining layer. The fresh groundwater recharge results in thin rainwater lenses between the drain tiles.

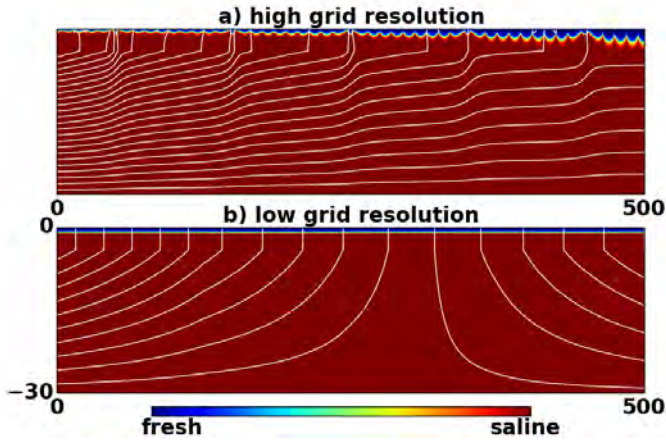


Figure 2.1: Illustrative example on simulating GW-SW interaction using a high grid resolution (a) and low grid resolution (b), where the conductance is only based on the dimensions and hydraulic resistance of the surface water bed (i.e., the conductance expression of McDonald and Harbaugh (1988)). The colors indicate concentrations, and the white lines indicate streamlines. The unit of the horizontal and vertical extent indications is meter.

Figure 2.1b shows the result of a corresponding model with the same model layer thickness but with a column width of 100 m. Again, the conductance expression of McDonald and Harbaugh (1988) is used by summing the widths of the individual drain tiles and ditches in the cell, so that only the resistance to flow across the streambed is accounted for. The streamlines indicate that all saline groundwater that enters the model on the left boundary flows to the upper boundary, and that there is also inflow from the right boundary. This illustrates that the resistance to GW-SW interaction is greatly underestimated. In this case, the total flux toward the surface water is overestimated by a factor of 6. Such significant errors can also be expected in similar hydrogeological conditions.

Expressions for the conductance that take into account the resistance to GW-SW interaction below the surface water bed are scarce in the international literature. In this chapter, the performance of three existing conductance expressions that each take into account the resistance below the surface water bed in a different way are evaluated. These are the two conductance expressions that were presented by Mehl and Hill (2010) and the conductance expression of De Lange (1999). Morel-Seytoux (2009) and Morel-Seytoux et al. (2014) presented a method to account for the resistance below the surface water bed, which is based on combining an analytical expression that accounts for all the resistance due to GW-SW interaction, with the numerical solution at a 'far' distance. However, this method cannot be directly applied as a Cauchy boundary condition in cases where multiple surface water have to be accounted for in a single model cell or the aquifer is discretized in the vertical direction. Because these aspects are crucial for the work that is presented in this chapter, the methods of Morel-Seytoux

(2009) and Morel-Seytoux et al. (2014) are not considered.

The objective of this chapter is to assess the accuracy of the two conductance expressions of Mehl and Hill (2010), and the conductance expression of De Lange (1999) when applied in simulations with a low grid resolution. The influence of (1) variable groundwater density, (2) vertical grid discretization, and (3) simulation of ditches and drain tiles in a single model cell, on the accuracy of quantifying water fluxes and salt loads to ditches and drain tiles is considered for a wide range of hydrogeological conditions, and the differences between the methods are discussed.

## 2.2 Material and methods

### 2.2.1 Conductance expressions

Mehl and Hill (2010) presented two expressions for the conductance that, besides the resistance across the surface water bed, also account for the resistance below it. For convenience, 'surface water' refers to both ditches and drain tiles in this chapter, and 'surface water bed' refers to the hydraulically resistive unit directly below the surface water (e.g., a streambed). The first expression for the conductance (equation 3 of Mehl and Hill (2010)) is denoted here with  $C_{MH3}$ :

$$C_{MH3} = \left( \frac{c_0}{B_l B} + \frac{0.5 \Delta z}{k_v A} \right)^{-1} \quad (2.2)$$

$c_0$  is the entry resistance of the surface bed [T]. The entry resistance is defined as the thickness of the surface water bed divided by its vertical hydraulic conductivity. Furthermore,  $B_l$  is the length of the surface water in the grid cell [L],  $B$  is the width of the surface water in the grid cell [L],  $A$  is the area of the grid cell [L<sup>2</sup>],  $\Delta z$  is the thickness of the model layer in which the boundary condition is applied [L], and  $k_v$  is the vertical hydraulic conductivity of the hydrogeological unit below the surface water bed [L T<sup>-1</sup>]. Note that the numerator in the second term of Equation 2.2 is different than the expression by Mehl and Hill (2010), because it is assumed here that the surface water does not penetrate (deep) into the confining layer. Moreover, it is assumed that the thickness of the surface water bed can then be neglected relative to the thickness of the confining layer and that the bottom of the surface water bed is located close to the top of the saturated thickness of the confining layer.

The first term on the right-hand side of Equation 2.2 is equal to the 'river' conductance expression of McDonald and Harbaugh (1988). Note that in case of multiple ditches or drain tiles in one grid cell, their total length ( $B_l$ ) and total width ( $B$ ) are summed. Here, only cases where the drain tiles or ditches have equal properties are considered, such as  $c_0$  and  $B$ . The second term on the right-hand side of Equation 2.2 is a correction for the vertical flow resistance below the surface water bed. In this correction, it is assumed that the total cell area

contributes to the flow between the surface water bed and the node where the boundary condition is applied.

The second expression for the conductance presented by Mehl and Hill (2010) (equation 4 in their work) is denoted here with  $C_{MH4}$  and is defined as:

$$C_{MH4} = \left( \frac{c_0}{B_l B} + \frac{0.5 \Delta z}{k_v B_l B} \right)^{-1} \quad (2.3)$$

The difference with Equation 2.2 is related to the correction for the vertical flow resistance below the surface water bed; in Equation 2.3, it is assumed that only the area below the surface water bed contributes to the flow between the bottom of the surface water bed (i.e., the top of the saturated thickness of the confining layer) and the node where the boundary condition is applied, whereas in Equation 2.2, this is the total cell area.

The conductance expression of De Lange (1999) is based on an analytical solution of a representative local flow system; the interaction between a regional aquifer, a relatively thin upper aquifer (in this case, a confining layer), and surface water (Figure 2.2). In his work, De Lange (1999) first derived an expression for the resistance to GW-SW interaction, based on the parameters  $B$ ,  $c_0$ ,  $c_1$  (vertical resistance of the layer below the confining layer [T]),  $H$  (thickness of the confining layer [L]),  $k_h$  (horizontal hydraulic conductivity in the confining layer [L T<sup>-1</sup>]),  $k_v$  (vertical hydraulic conductivity in the confining layer), and  $L$  (the distance between the surface waters [L]). This resistance is called the phreatic leakage resistance ( $c_{PL}$ ) and is defined as:

$$c_{PL} = \frac{1}{\frac{\omega}{c_B^* (c_L^* + c_{rad})} + \frac{(1-\omega)}{(c_L^* + c_{rad})} \frac{1}{E}} - c_1' \quad (2.4)$$

$\omega$  is the areal percentage of the surface water in the grid cell. In two-dimensional (2D) cross section,  $\omega$  is equal to  $B/(L + B)$ .  $E$  is a correction if  $L$  is larger than the width of the grid cells. In this chapter,  $L$  is always smaller than or equal to the width of the grid cells, and  $E$  equals 1. The remaining expressions are:

$$c_B^* = \frac{(c_0 + c_1')}{c_L^* - \frac{c_0 L}{B}} \quad (2.5a)$$

$$c_L^* = (c_0 + c_1') F_L + \left( \frac{c_0 L}{B} \right) F_B \quad (2.5b)$$

$$F_i = \frac{i}{2\lambda} \operatorname{cotan} \left( \frac{i}{2\lambda} \right), \quad (i = B, L) \quad (2.5c)$$

$$\lambda_B = \sqrt{\frac{kHc_0c'_1}{c_0 + c'_1}} \quad (2.5d)$$

$$\lambda_L = \sqrt{c'_1 H k_h} \quad (2.5e)$$

$$c'_1 + \frac{H}{k_v} \quad (2.5f)$$

$$c_{rad} = \frac{L}{\pi\sqrt{k_h k_v}} \ln \left( \frac{4H}{\pi B} \sqrt{\frac{k_h}{k_v}} \right) \quad (2.5g)$$

$c'_1$  [T] and  $c_{rad}$  [T] account for the vertical flow resistance and radial flow resistance (i.e., the resistance to flow due to convergence of flow lines) within the confining layer, respectively. These terms are corrections for the Dupuit assumption. De Lange (1999) implemented these terms empirically using the superposition principle. The results of the solution with these empirical corrections have been verified with the results of a 2D analytical solution (Bruggeman, 1972), which does exactly account for the resistance to vertical and radial flow. Note that  $c_{rad}$  accounts for anisotropy by replacing the isotropic hydraulic conductivity  $k$  by  $\sqrt{k_h k_v}$  and by multiplication of  $H$  by  $\sqrt{k_h/k_v}$ . Similar transformation procedures were presented by Bear and Dagan (1965).

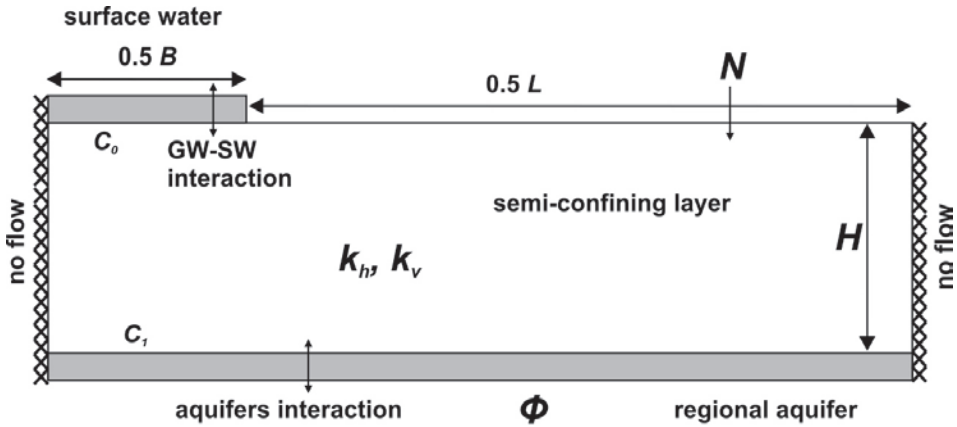


Figure 2.2: Concept that De Lange (1999) used to derive  $c_{PL}$  (Equation 2.4).

The conductance for a given type of surface water (e.g., with a comparable width and drainage level) using the method of De Lange (1999) is equal to the

planar area of the grid cell divided by  $c_{PL}$  and is denoted in this chapter with  $C_{DL}$ . In three-dimensional (3D) models,  $L$  is equal to the planar area of the grid cell divided by the total length of that surface water in the grid cell. Further details on the use  $C_{DL}$  in 3D models can be found in De Lange (1996) and De Lange (1999). Note that although  $C_{DL}$  is an overlooked conductance expression in the literature, it is successfully applied in the national hydrological instrument of the Netherlands (De Lange et al., 2014).

Besides that  $C_{DL}$  is based on an analytical solution of a flow problem (Figure 2.2), it differs from  $C_{MH3}$  and  $C_{MH4}$  by two main aspects. First,  $C_{DL}$  takes into account, in addition to the vertical flow resistance, the resistance to horizontal flow and radial flow. Second, the correction for the vertical flow resistance is not related to the distance between the node where the boundary condition is applied and the bottom of the surface water bed, but on an analytical expression for the concept shown in Figure 2.2.

## 2.2.2 Grid resolution comparison

SEAWAT (Langevin et al., 2007) was used for the numerical simulations. How the influence of variable groundwater density, vertical grid discretization, and the simulation of both ditches and drains in a single model cell on the accuracy of  $C_{DL}$ ,  $C_{MH3}$ , and  $C_{MH4}$  regarding water and salt fluxes was analyzed is explained in the next sections. The groundwater flow equation in SEAWAT was solved using the PCG package with an hydraulic head convergence criterion of  $10^{-6}$  m and the dispersion and sink and source terms of solute transport equation were solved using the GCG package with a convergence criterion of  $10^{-6}$ . Advection was simulated using the MOC method with a Courant number of 0.75 and a minimum number of 9 and a maximum number of 27 particles per grid cell.

## 2.2.3 Base comparison

In a 'base comparison', the model concept shown in Figure 2.3 was used. It represents a section halfway between the two drain tiles in a confining layer that overlies a regional aquifer. The left and right boundaries are no-flow boundaries. The lower boundary is a constant-head boundary condition with hydraulic head  $\phi$  [L], which is higher than the drainage level. This results in upward flow from the bottom of the model. Related studies on thin rainwater lenses (e.g., (De Louw et al., 2011; Eeman et al., 2011) have also used a similar boundary condition at depth to simulate the upward flow of saline groundwater. A drain tile is present in the region  $0.5B_{dr}$ . In the region  $0.5L_{dr}$ , there is fresh groundwater recharge with a rate  $N$  [L T<sup>-1</sup>].

A high (reference) grid resolution and a low grid resolution were used for this model. In the reference grid resolution, the columns have a width ( $\Delta x$ ) of 0.05 m and a layer thickness ( $\Delta z$ ) of 0.1 m in the confining layer. In the underlying aquifer,  $\Delta z$  increases steadily with depth. For the conductance of the drain tile, the

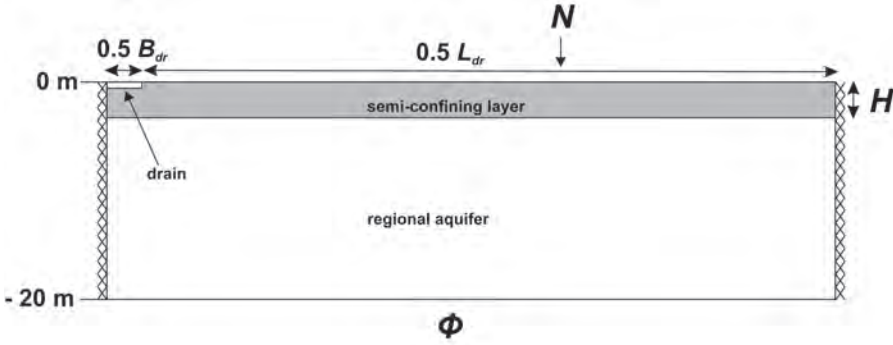


Figure 2.3: Model concept for the base comparison and for investigating the influence of vertical discretization and variable groundwater density on the accuracy of  $C_{DL}$ ,  $C_{MH3}$ , and  $C_{MH4}$ .

method of McDonald and Harbaugh (1988) was used. A comparison with a higher grid resolution with a  $\Delta x$  of 0.01 m indicated a relative difference in fluxes of less than 1%, which indicates that a sufficiently fine grid for the reference resolution was used.

For the low grid resolution, the same layer thickness as in the reference grid resolution was used, but with a column width ( $\Delta x$ ) equal to  $0.5(L_{dr} + B_{dr})$ . For the conductance,  $C_{MH3}$ ,  $C_{MH4}$ , and  $C_{DL}$  were used. In what follows,  $C_{MH3}$ ,  $C_{MH4}$ , and  $C_{DL}$  will refer to the low grid resolution.

The two grid resolutions were compared by analyzing a relative error in the flux toward the drain tile  $\epsilon$  [-] for  $C_{MH3}$ ,  $C_{MH4}$ , and  $C_{DL}$ :

$$\epsilon = \frac{Q_{low} - Q_{ref}}{Q_{ref}} 100\% \quad (2.6)$$

$Q_{ref}$  [ $L^3 T^{-1}$ ] is the volumetric flux toward the drain tile using the reference grid resolution and  $Q_{low}$  [ $L^3 T^{-1}$ ] is the volumetric flux toward the drain tile using the low grid resolution.

In the base comparison, variable density groundwater flow and dispersive salt transport take place in a regional confined aquifer system. The isotropic aquifer has a hydraulic conductivity of  $20 \text{ m d}^{-1}$ . The longitudinal dispersivity in the system is 0.1 m, and the horizontal and vertical transversal dispersivity are both 0.01 m. Salt content is expressed as chloride concentration. The chloride (Cl) concentration varies between 0 (freshwater) and  $18.63 \text{ g l}^{-1}$  (salt groundwater), corresponding to a groundwater density of 1000 and  $1025 \text{ kg m}^3$ , respectively. Cl varies linearly with groundwater density. The initial Cl concentration in the model domain is  $18.63 \text{ g l}^{-1}$ . Fresh groundwater recharge with a rate of  $0.001 \text{ m d}^{-1}$  takes place in the upper model layer. The hydraulic head  $\phi$  in the bottom

layer is 0.5 m, and the drainage level in the top layer is 0 m. The drain tile was implemented using the DRAIN package of SEAWAT. The thickness of the drain tile envelope divided by the hydraulic conductivity of the drain envelope (this ratio is referred to as the entry resistance) was assumed to be 1 d, and the drain tile has a perimeter of 0.3 m. The models were analyzed at steady state regarding the total mass in the model domain.

A wide range of hydrogeological conditions representative for confined systems in deltaic coastal areas was considered, using a sensitivity analysis based on variation of the parameters  $H$ ,  $L_{dr}$  (the distance between the drain tiles), and homogeneous and isotropic  $k$  (i.e., for the confining layer). These parameters were related based on the Hooghoudt relationship (Hooghoudt, 1940), which is common in the drainage design, avoids unrealistic parameter combinations, and reduces the parameters space in the sensitivity analysis:

$$N = \frac{8kd\Delta h + 4k(\Delta h)^2}{L_{dr}^2} \quad (2.7)$$

where  $N$  is the recharge rate,  $\Delta h$  is the difference in maximum hydraulic head between the drain tiles, and  $d$  is the effective depth of groundwater flow.  $d$  was calculated using the equation of Moody (1966):

$$d = \frac{H}{1 + \frac{8H}{\pi L_{dr}} \ln \frac{H}{B_{dr}}} \quad (2.8)$$

Because  $d$  also depends on  $L_{dr}$ , Equations 2.7 and 2.8 should be solved iteratively to calculate  $L_{dr}$  for a given  $N$ ,  $\Delta h$ ,  $k$ ,  $B_{dr}$ , and  $H$ . In this relationship between  $H$ ,  $L_{dr}$ , and  $k$ ,  $N$  and  $\Delta h$  were assumed to be  $0.007 \text{ m d}^{-1}$  and  $0.5 \text{ m}$ , respectively (common values in the tile drainage design (ILRI, 1973)), and  $B_{dr}$  was held constant at  $0.3 \text{ m}$ .  $H$  varies between  $2$ ,  $4$ , and  $6 \text{ m}$ , and  $k$  ranges from  $0.05$  to  $0.5 \text{ m d}^{-1}$ .

## 2.2.4 Influence of variable groundwater density

The influence of variable groundwater density was investigated by comparing all simulations of the base comparison with the corresponding constant groundwater density simulations. In addition, the influence of a lower hydraulic head ( $0.1 \text{ m}$ ) at the bottom of the model was investigated. The rationale of investigating the influence of a lower hydraulic head is that it influences the variable groundwater density flow, because a system of mixed convection was considered. Amongst others, the different hydraulic head at the bottom of the model affects the thickness of the thin freshwater lens that forms between drain tiles (Figure 2.1).

### 2.2.5 Influence of vertical discretization

For the influence of vertical discretization, the same approach as in the base comparison was used, but with a layer thickness  $\Delta z$  of 2 m in the low grid resolution. An influence of vertical discretization can be expected as  $C_{MH3}$  and  $C_{MH4}$  depend on  $\Delta z$ , and because  $C_{DL}$  was derived for situations where the confining layer is not discretized vertically. Note that in variable density groundwater flow and solute transport models, more layers are generally used compared to constant density models (Langevin, 2003).

### 2.2.6 Simulation of ditches and drain tiles

The motivation for investigating the influence of simulating both ditches and drain tiles in a single model cell on the accuracy  $C_{MH3}$ ,  $C_{MH4}$  and  $C_{DL}$  was twofold. First, ditches may have different dimensions and properties than drain tiles in the model cell. These different properties might affect the accuracy of the conductance expressions. Second, the horizontal influence lengths of ditches and drain tiles may interfere, which influences the distribution of the fluxes and therefore the accuracy of the three conductance expressions.

The model concept shown in Figure 2.4 was used to investigate the simulation of both ditches and drain tiles in a single model cell. This concept is comparable to the concept of the base comparison, but spans a larger area as it represents a section halfway between the two ditches. In between the ditches, drain tiles are present. The model setup and constant parameters are similar to those of the base comparison, although with some exceptions. The cell size in the low grid resolution model is equal to  $0.5(L_{dt} + B_{dt})$ . The drainage level of the drain tiles is 0.25 m higher than the water level in the ditch. The ditch has an entry resistance (i.e., the thickness of the ditch bed divided by its vertical hydraulic conductivity) of 1 d and is simulated using the GHB package of SEAWAT. Furthermore, the sensitivity analysis comprises variations of parameters related to the ditch; three different values for the width of the ditch ( $B_{dt} = 5, 10, \text{ and } 15 \text{ m}$ ), distance between the ditches ( $L_{dt} = 60, 120, \text{ and } 180 \text{ m}$ ), and thickness of the confining layer ( $H = 2, 4, \text{ and } 6 \text{ m}$ ). In addition, three different values of the hydraulic conductivity of the confining layer ( $k = 0.05, 0.25, \text{ and } 0.5 \text{ m d}^{-1}$ ) were used. Similar to the base comparison, the drain tile distance ( $L_{dr}$ ) was related to  $H$  and  $k$  according to Equations 2.7 and 2.8.

### 2.2.7 Salt load to the ditches and drain tiles

In addition to water fluxes, the previous simulations were also analyzed regarding salt loads to the ditches and drain tiles. The total salt load for the ditches or drain tiles equals the product of the volumetric flux toward the drain tile or ditch with the concentration of the cell, summed for every cell where the boundary condition

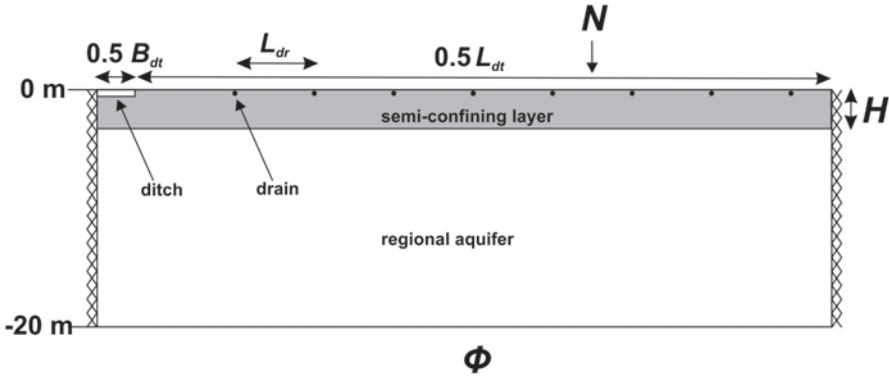


Figure 2.4: Model setup to investigate the influence of simultaneous simulation of ditches and drain tiles on the accuracy of  $C_{MH3}$ ,  $C_{MH4}$  and  $C_{DL}$ .

is applied. The relative error in the salt load  $\epsilon_c$  [-] is:

$$\epsilon_c = \frac{QC_{low}QC_{ref}}{QC_{ref}} 100\% \quad (2.9)$$

where  $QC_{ref}$  [ $M T^{-1}$ ] is the total salt load (either for the ditch or drain tiles) in the reference grid resolution and  $QC_{low}$  [ $M T^{-1}$ ] is the total salt load in the low grid resolution. In addition to investigating relative errors in salt load, the absolute total salt loads to the ditch and drain tiles were investigated by analyzing the simulations on the difference in total salt load between the low grid resolution and reference grid resolution, per unit area ( $\Delta QC$  [ $M L^{-2} T^{-1}$ ]):

$$\Delta QC = \frac{QC_{crs}}{A_{crs}} - \frac{QC_{ref}}{A_{crs}} \quad (2.10)$$

where  $A_{crs}$  [ $L^2$ ] is the area of the cell in the low grid resolution model.

## 2.3 Results

For convenience, the discussion of the results regarding  $C_{DL}$ ,  $C_{MH3}$ , and  $C_{MH4}$  is based on resistances.

### 2.3.1 Base comparison

Figure 2.5 shows  $\epsilon$  for all the parameter combinations in the base comparison, where the reference grid resolution was compared with a low grid resolution (in which  $\Delta x$  was equal to  $0.5(L_{dr} + B_{dt})$ ). The most important observation from

Figure 2.5 is the difference between  $C_{DL}$ ,  $C_{MH3}$ , and  $C_{MH4}$ ;  $C_{DL}$  performs much better than  $C_{MH3}$  and  $C_{MH4}$ . This is also indicated in Table 2.1, where the average absolute value of  $\epsilon$  among all parameter combinations ( $|\epsilon_{av}|$ ) is given.

In the remainder of this section, the behavior of  $\epsilon$  as a function of  $k$  in the sensitivity analysis for  $C_{DL}$ ,  $C_{MH3}$ , and  $C_{MH4}$  is discussed. Note that  $k$  and  $L_{dr}$ , considering Equations 2.7 and 2.8, co-vary about linearly. Therefore,  $\epsilon$  is shown as a function of  $k$  in Figure 2.5; plotting  $\epsilon$  as a function of  $L_{dr}$  would yield similar results. For  $C_{DL}$ ,  $\epsilon$  is negative and increases upon an increase in  $k$  and a decrease in  $H$ . This can be explained by the vertical discretization. Because the confining layer is discretized vertically, parts of the vertical and radial flow resistances in  $C_{DL}$  are already accounted for. The empirical corrections to account for the radial and vertical flow resistance in  $C_{DL}$  lead to a too high resistance, a too low upward groundwater flux, and therefore, a negative  $\epsilon$ .

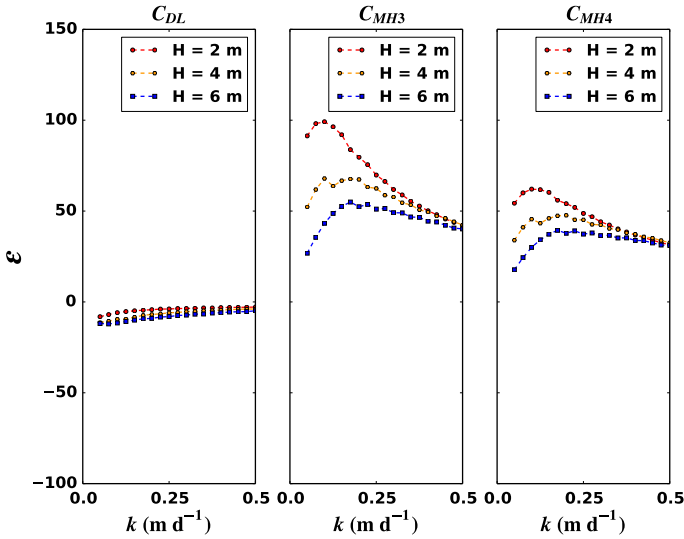


Figure 2.5:  $\epsilon$  for the simulations in the base comparison, where variable groundwater density flow was simulated and the hydraulic head at the bottom of the model was 0.5 m.

For  $C_{MH3}$ ,  $\epsilon$  is positive for all parameter combinations, so the resistance to GW-SW interaction using  $C_{MH3}$  is underestimated. Hence, correcting for the vertical flow resistance using the second term on the right-hand side in Equation 2.2 is in this case not sufficient to correct for the total resistance to GW-SW interaction. This effect decreases with an increase in  $H$ .

The three lines for the different values of  $H$  for the  $C_{MH3}$  models show the same pattern;  $\epsilon$  first increases and then decreases upon an increase of  $k$ . The increase of  $\epsilon$  is related to the increase of the drain tile spacing  $L_{dr}$  (which increases as  $k$  increases) and the horizontal influence length of the drain tile in the aquifer.

Table 2.1:  $|\epsilon_{av}|$  for  $C_{DL}$ ,  $C_{MH3}$ , and  $C_{MH4}$ , for the simulations in the base comparison (indicated by \*) and for the simulations to investigate the influence of variable groundwater density. CD refers to the simulations with constant groundwater density, VD refers to the simulations with variable groundwater density.  $\phi$  refers to the hydraulic head at the bottom of the aquifer.

| Conductance expression | Groundwater flow | $\phi$ (m) | $ \epsilon_{av} $ (%) |
|------------------------|------------------|------------|-----------------------|
| $C_{DL}$               | CD               | 0.1        | 3.9                   |
| $C_{DL}$               | CD               | 0.5        | 5.9                   |
| $C_{DL}$               | VD               | 0.1        | 10.0                  |
| $C_{DL}^*$             | VD               | 0.5        | 6.2                   |
| $C_{MH3}$              | CD               | 0.1        | 38.0                  |
| $C_{MH3}$              | CD               | 0.5        | 57.6                  |
| $C_{MH3}$              | VD               | 0.1        | 28.5                  |
| $C_{MH3}^*$            | VD               | 0.5        | 57.2                  |
| $C_{MH4}$              | CD               | 0.1        | 26.9                  |
| $C_{MH4}$              | CD               | 0.5        | 40.8                  |
| $C_{MH4}$              | VD               | 0.1        | 18.2                  |
| $C_{MH4}^*$            | VD               | 0.5        | 40.4                  |

De Lange (1999) showed that the horizontal influence length of surface water can be estimated by  $3\lambda_L$ , which is in this case approximately equal to  $3H$ . If the spacing of the drain tiles increases within the distance  $3\lambda_L$ , the resistance is further underestimated. Beyond  $3\lambda_L$ , there is no influence of the drain tile and the increase of  $k$  leads to a value of  $\epsilon$  closer to 0. The reason that  $\epsilon$  is closer to 0 at higher values of  $k$  is that an increase in  $k$  leads to a decrease in the contribution of the resistance below the surface bed to the total resistance to GW-SW interaction, and therefore a smaller error in the accuracy of  $C_{MH3}$ . The larger the  $H$ , the larger the drain tile spacing at which the turning point is present.

The behavior of  $\epsilon$  as a function of  $k$  and  $H$  is comparable between the simulations using  $C_{MH3}$  and  $C_{MH4}$ , but  $C_{MH4}$  performs better. This is caused by a higher resistance to GW-SW interaction in the simulations using  $C_{MH4}$  compared with  $C_{MH3}$ , as  $C_{MH4}$  assumes that only the area below the surface water contributes to vertical flow, instead of the total cell area in  $C_{MH3}$ .

### 2.3.2 Variable groundwater density

For the simulations to investigate the influence of variable groundwater density, the relative behavior of  $\epsilon$  as a function of  $k$  is comparable to the results of the base comparison. For brevity, the corresponding figures are given in the Appendix of this chapter. The absolute errors, however, show differences. Table 2.1 shows the average of the absolute  $\epsilon$  of the simulations ( $|\epsilon_{av}|$ ). The most important observation from Table 2.1 is the difference in  $|\epsilon_{av}|$  between  $C_{MH3}$ ,  $C_{MH4}$ , and  $C_{DL}$ ;  $C_{DL}$  performs much better than  $C_{MH3}$  and  $C_{MH4}$  for the different values of  $\phi$ , independent of whether variable density groundwater flow is simulated or not.

The influence of variable groundwater density on  $C_{MH3}$ ,  $C_{MH4}$ , and  $C_{DL}$  is

small in case of  $\phi = 0.5$  m. For  $\phi = 0.1$  m, variable groundwater density leads to an increase of  $|\epsilon_{av}|$  using  $C_{DL}$ , but a decrease using either  $C_{MH3}$  or  $C_{MH4}$ . The higher influence of variable groundwater density at lower values of  $\phi$  could be expected, as the influence of variable groundwater density in this mixed convection setting increases with decreasing values of  $\phi$ . The influence of a higher hydraulic head at the bottom of the aquifer on  $|\epsilon_{av}|$  using  $C_{DL}$  is moderate for  $C_{DL}$  relative to  $C_{MH3}$  and  $C_{MH4}$ .

### 2.3.3 Vertical discretization

Figure 2.6 shows  $\epsilon$  for all the considered parameter combinations where in the low grid resolution,  $\Delta x$  was equal to  $0.5(L_{dr} + B_{dr})$  and  $\Delta z$  was equal to 2 m. The most important observation from Figure 2.6 is that  $C_{DL}$  performs best.  $|\epsilon_{av}|$  for  $C_{DL}$  is 2.9 %, whereas for  $C_{MH3}$  and  $C_{MH4}$  this is 57.6 and 43.2 %, respectively.

Vertical discretization influences the accuracy of  $C_{DL}$ . This can be deduced by comparing Figures 2.5 and 2.6;  $\epsilon$  is always positive, whereas in the base comparison  $\epsilon$  was negative and the  $C_{DL}$  was less accurate. This can be expected, as  $C_{DL}$  was derived for cases where the confining layer is not discretized. For  $C_{MH3}$ , there is little influence of vertical discretization on its accuracy for the conditions that have been considered, as can be deduced by comparing Figures 2.5 and 2.6 and the values of  $|\epsilon_{av}|$ . Despite that  $C_{MH3}$  depends on the layer thickness, the errors that are introduced in using  $C_{MH3}$  are much larger than the influence of vertical discretization. In contrast, for  $C_{MH4}$  the influence of vertical discretization is much larger;  $\epsilon$  in this case is always negative. This can be attributed to the difference in correction for the vertical flow resistance. In  $C_{MH3}$ , it is assumed that the entire cell surface area contributes to the flow toward the surface water, whereas in  $C_{MH4}$  this is only the area of the surface water in the cell. The correction for the vertical flow resistance using  $C_{MH4}$  leads to an overestimation of the resistance, due to increased  $\Delta z$ .

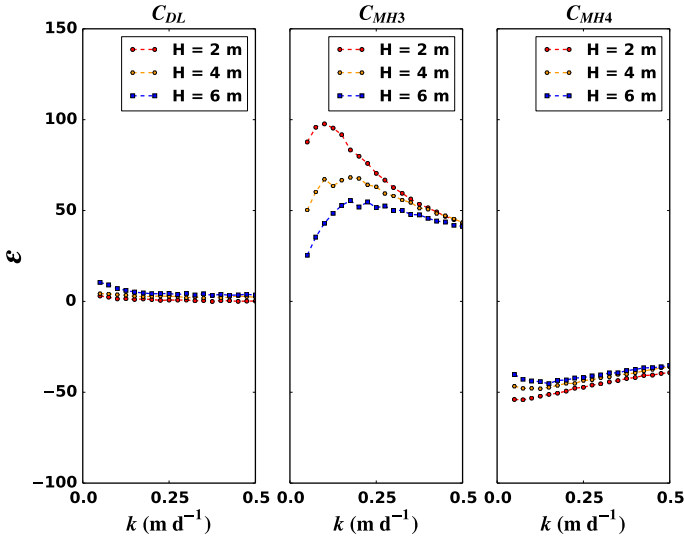


Figure 2.6:  $\epsilon$  for all considered system parameter combinations in the comparison where the effect of vertical discretization was investigated, where the low grid resolution models have a layer thickness  $\Delta z$  of 2 m. Note that the layer thickness in the base comparison is 0.1 m.

### 2.3.4 Simulation of ditches and drain tiles

Figure 2.7 shows  $\epsilon$  in case of drainage by both drain tiles and a ditch, for all models with the parameter combinations as listed in Table 2.2 of the Appendix of this chapter. The parameter combinations were numbered and they were used to plot the results for two reasons. First, there are only three variations per parameter in the sensitivity analysis. Plotting  $\epsilon$  relative to a parameter, therefore, leads to clustered results. Second, the purpose of this investigation was to cover a wide range of hydrogeological conditions, and not to obtain thorough understanding of the relationship between  $\epsilon$  and the different model parameters.

For the drain tiles using  $C_{DL}$ ,  $|\epsilon_{av}|$  is 19%, whereas for the ditch this is 10%. For  $C_{MH3}$  and  $C_{MH4}$ ,  $|\epsilon_{av}|$  is much higher. For  $C_{MH3}$ ,  $|\epsilon_{av}|$  is 67% for the drain tiles and 562% for the ditch. Using  $C_{MH4}$  resulted in  $|\epsilon_{av}|$  of 62% for the drain tiles and 465% for the ditch. Especially, the errors in the flux toward the ditch are remarkably high for  $C_{MH3}$  and  $C_{MH4}$ . This is due to the large underestimation of the resistance to GW-SW interaction for both the ditch and drain tiles in combination with the dominant drainage of the ditch, as it has a lower drainage level. Therefore, nearly all the upward flowing groundwater from the aquifer and the groundwater recharge in the confining layer are discharged by the ditch. The higher the hydraulic conductivity of the confining layer, indicated by the increasing simulation number in Figure 2.7, the less significant this effect is. For higher

values of  $k$ , the relative contribution of the resistance to GW-SW interaction below the surface water bed to the total resistance decreases, and therefore also the contribution of its error.

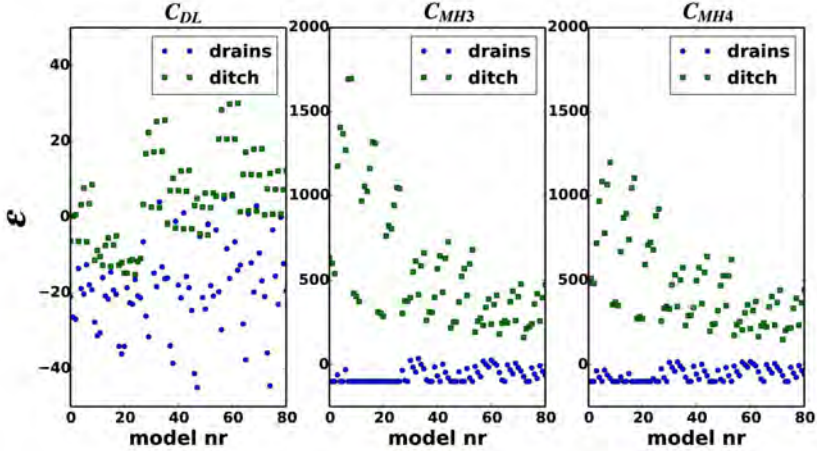


Figure 2.7:  $\epsilon$  for the drain tiles and for the ditch in the investigation of the influence of simulating both a ditch and drain tiles using a single model cell. Note the difference in vertical scale between  $C_{DL}$  and  $C_{MH3}$  and  $C_{MH4}$ .

In this investigation in which the drainage by the drain tiles and the ditch was simulated using a single model cell,  $|\epsilon_{av}|$  for the drain tiles using  $C_{DL}$  is much higher (19%), then in the cases using only one drain tile (8 to 9%). These differences are the result of the interference between the influence zones of the drain tiles and the ditch. The influence zone can be estimated by  $3\lambda_L$  (De Lange, 1999). It appeared that the larger the number of drain tiles between the ditches, the lower the relative impact on the total fluxes toward the drain tiles is, and the lower the value of  $\epsilon$ . The values of  $\epsilon$  using  $C_{DL}$  are still acceptable, especially relative to the values of  $\epsilon$  for  $C_{MH3}$  and  $C_{MH4}$ .

### 2.3.5 Salt loads toward the ditches and drain tiles

The relative error in the salt load towards the ditch and drain tiles  $\epsilon_c$  showed a comparable pattern as in Figure 2.7. Also, the values for the average absolute error ( $|\epsilon_c|$ ) are comparable; for  $C_{DL}$ ,  $|\epsilon_c|$  is 19% for the drain tiles and 10% for the ditch. For  $C_{MH3}$ ,  $|\epsilon_c|$  is 67% for the drain tiles and 569% for the ditch.  $|\epsilon_c|$  using  $C_{MH4}$  resulted in 61% for the drain tiles and 471% for the ditch. This indicates that for the investigated parameter combinations, the salt loads are dominated by fluxes rather than by concentrations.

Figure 2.8 shows  $\Delta QC$ , the absolute error in salt loads, for the drain tiles and ditch using  $C_{MH3}$ ,  $C_{MH4}$ , and  $C_{DL}$ . In general,  $C_{MH3}$ ,  $C_{MH4}$ , and  $C_{DL}$

overestimate the salt loads for the ditch (positive  $\Delta QC$ ) but underestimate it for the drain tiles.  $\Delta QC$  for  $C_{MH3}$  and  $C_{MH4}$  regarding the ditch increases with increasing values of  $k$ . Based on the previous results, this may seem counter-intuitive, as the relative error in the flux toward the surface water system decreases upon an increase of  $k$ . However, the absolute errors are higher because a higher  $k$  leads to a larger water and salt flux to the drain tiles and ditch.

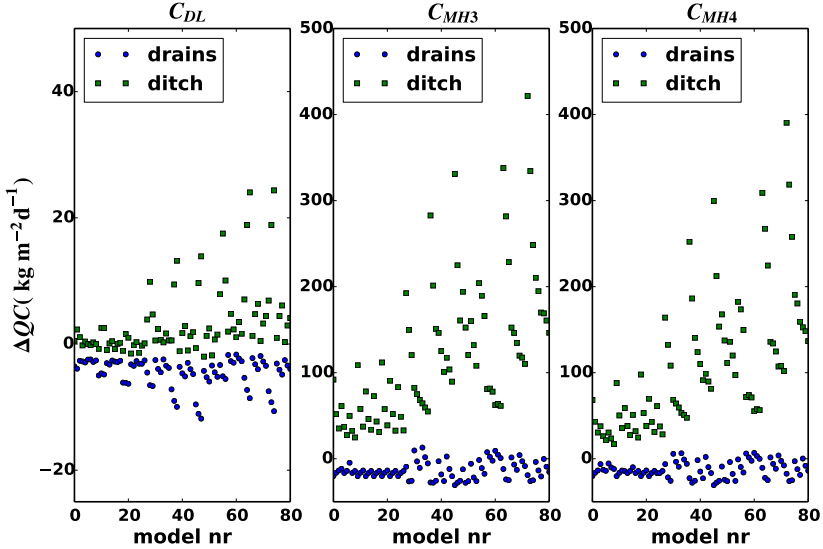


Figure 2.8:  $\Delta QC$  for the drain tiles and the ditch. Note the difference in vertical scale between  $C_{DL}$  and  $C_{MH3}$  and  $C_{MH4}$ .

## 2.4 Discussion

### 2.4.1 Conductance expressions

In all simulations,  $C_{DL}$  performed better than  $C_{MH3}$  and  $C_{MH4}$ , as the resistance to GW-SW interaction in the confining layer is better accounted for. This has two reasons. The first reason is that in  $C_{DL}$  the resistances to horizontal flow and radial flow are taken into account, whereas in  $C_{MH3}$  and  $C_{MH4}$ , these are neglected. The result is that in many simulations using  $C_{MH3}$  and  $C_{MH4}$ , the fluxes toward the ditch and drain tiles were overestimated. The second reason is that  $C_{DL}$  is less sensitive to vertical discretization. In  $C_{MH3}$  it is assumed that the total width of the grid cell area contributes to the vertical flow to or from the surface water. This assumption resulted in a severe underestimation of the resistance to GW-SW interaction, such that the influence of the vertical discretization was negligible. In contrast, in  $C_{MH4}$  only the area directly below the surface water contributes to

the flow to or from the surface water, which resulted in an overestimation of the resistance in case of a 2 m thick model layer.

Mehl and Hill (2010) already indicated the limitations of  $C_{MH3}$  and  $C_{MH4}$  in cases where the area of the surface water in the cell is much smaller than the planar surface area of the cell, such as was the case in all simulations with a low grid resolution. Moreover,  $C_{MH3}$  and  $C_{MH4}$  were derived for a single type of surface water, whereas  $C_{DL}$  was applied for multiple surface water in a cell, by lumping the individual widths of the drain tiles and ditches. Therefore, the large differences between  $C_{DL}$  on the one hand, and  $C_{MH3}$  and  $C_{MH4}$  on the other hand could be expected beforehand. This chapter indicates that for the resistance to GW-SW interaction below the surface water bed, the radial flow, horizontal flow, and vertical flow resistance below the surface water have to be taken into account.

As was mentioned in the introduction of this chapter, Morel-Seytoux (2009) and Morel-Seytoux et al. (2014) have presented an analytical approach to account for the resistance due to GW-SW interaction, which shows similarities with the approach of De Lange (1999). The main difference between the two approaches is that De Lange (1999) derived an expression for a Cauchy boundary condition, whereas the works of Morel-Seytoux (2009) and Morel-Seytoux et al. (2014) are aimed at matching a numerical solution at a 'far' distance with an analytical solution that accounts for the resistance to GW-SW interaction. An advantage of the approach of Morel-Seytoux et al. (2014) is that it accounts for partial penetration of the surface water in the aquifer, as well as the geometry of the surface water bed. However, these conditions were not considered in this study. A comparison between the methods for cases where the surface water partially penetrates the aquifer is beyond the scope of this chapter, and is left for further work.

## 2.4.2 Limitations and generic applicability of $C_{DL}$

SEAWAT was used to model variable density groundwater flow and salt transport, but  $C_{DL}$  can also be applied in other (finite element) codes (De Lange, 1999). Although the upscaling method using  $C_{DL}$  can be used in an anisotropic confining layer, the accuracy of the method regarding this aspect was not analyzed. In addition, it is assumed that the hydraulic conductivity of the confining layer was spatially constant. The effect of upscaling heterogeneity regarding  $k_h$  and  $k_v$  as input parameters for  $C_{DL}$  was not considered and is left for further study.

The use of  $C_{DL}$  requires the determination of seven model parameters:  $c_0$ ,  $c_1$ ,  $B$ ,  $L$ ,  $k_h$ ,  $k_v$ , and  $H$ . In addition to the aforementioned potential difficulty in determining  $k_h$  and  $k_v$ , the thickness of the confining layer ( $H$ ) and the resistance of the layer under the confining layer ( $c_1$ ) may in some cases be difficult to determine and may vary within the grid cell. If case  $c_1$  is not clearly present and the vertical resistance of the confining layer is likely much higher,  $c_1$  can be assumed to be negligible, as it was assumed in this chapter.

It has been shown how different types of surface water (i.e., each with their

own  $L$ ,  $B$ ,  $c_0$ , and surface water level) can be simulated simultaneously in a model cell. This requires distinguishing different types of surface water, and determining  $L$ ,  $B$ ,  $c_0$ , and drainage level. Although this has been shown for two types of surface water (i.e., drain tiles and ditches), it is expected that  $C_{DL}$  also works when more than two types of surface water are present in the cell. The width of the surface water  $B$  is relatively easy to determine. This is also the case for the distance between the surface water  $L$  in 2D models. In 3D models,  $L$  is the planar area of the cell divided by the total length of the surface water in the cell. De Lange (1996) showed that this is also appropriate for surface waters that have an irregular shape. For very complex surface water distributions in a cell, like a meandering stream, inaccuracies can be expected, but this was not investigated. 3D models were not investigated due to the long computation times when using the reference grid resolution. Note that in this chapter, a horizontal grid cell size larger than or equal to the distance between the ditches or drain tiles is considered.  $C_{DL}$  can also be used if the horizontal grid cell size is smaller (De Lange, 1999).

The entry resistance of the surface water bed  $c_0$  may be hard to determine in the field. However, for the hydrogeological conditions that were considered in this chapter, the thickness of the streambed is assumed to be small and its hydraulic conductivity is assumed to be equal to or higher than the hydraulic conductivity of the confining layer. Under these conditions,  $c_0$  is much lower than the resistance to GW-SW interaction in the underlying aquifer. No references could be found on the hydraulic resistance of surface water beds in case the surface water is located in low-permeable sediment of confining layers. In confining layers, it is expected that the compacted sediments (i.e., clay, peat, or silt) have a much lower hydraulic conductivity than the unconsolidated sediment of the surface water bed. In situations where this is not the case, it is advised to investigate  $c_0$  for a correct determination of the conductance.

As a final note on the performance of  $C_{DL}$ , recall the illustrative example that was shown in Figure 2.1. Figure 2.9 shows the results of this example again, but now also with the results in case  $C_{DL}$  is used. The streamlines indicate that regional groundwater flow is much better simulated. In addition, the errors in the fluxes towards the ditches and drains are relatively minor, especially compared to the conventional upscaling (using the upscaling method of McDonald and Harbaugh (1988)); the discrepancy in the total water flux towards the drains is 6.6% and for the ditches 8.6%.

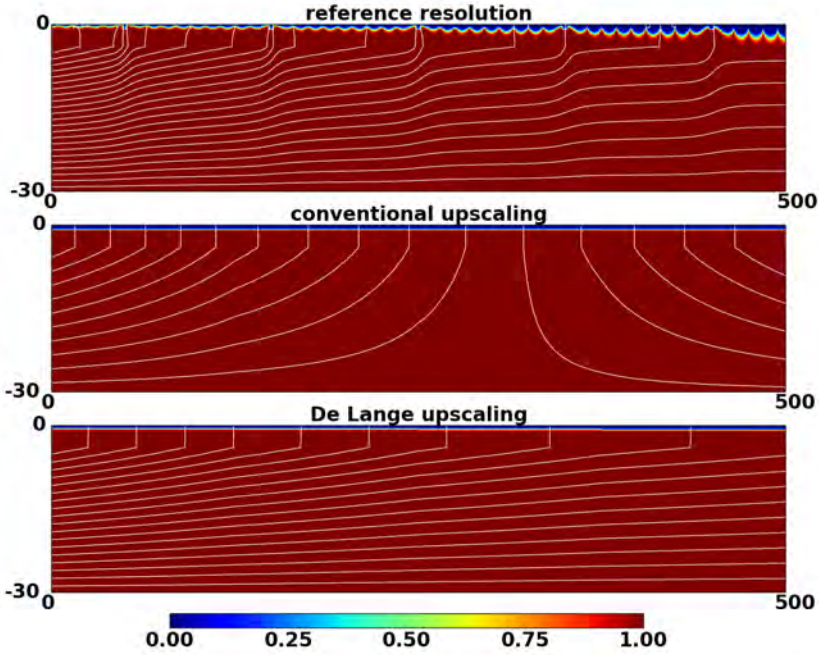


Figure 2.9: Results of the illustrative example in the introduction of this chapter (section 2.1), but now also including the results using  $C_{DL}$ . Note that the concentrations are scaled between 0 and 1.

## 2.5 Conclusions

In numerical groundwater flow models of confined aquifers using a low grid resolution, the resistance to GW-SW interaction below the surface water bed is important to take into account for determining the conductance. For the different aspects and hydrogeological conditions that were considered in this chapter, the conductance expression  $C_{DL}$  performed better than the expressions  $C_{MH3}$  and  $C_{MH4}$  as it better accounts for the horizontal, vertical, and radial flow resistance to GW-SW interaction in the confining layer. The influence of variable groundwater density and vertical grid discretization on the accuracy of quantifying water and salt fluxes using  $C_{DL}$  was small.

## 2.6 Appendix

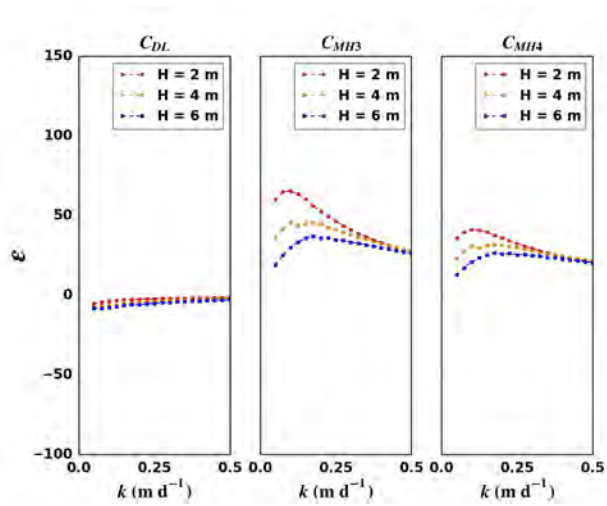


Figure 2.10:  $\epsilon$  for all considered system parameter combinations in the simulations with constant groundwater density flow and a constant hydraulic head at the bottom of the aquifer of 0.5 m.  $k$  is the hydraulic conductivity of the confining layer and  $H$  is thickness of the confining layer.

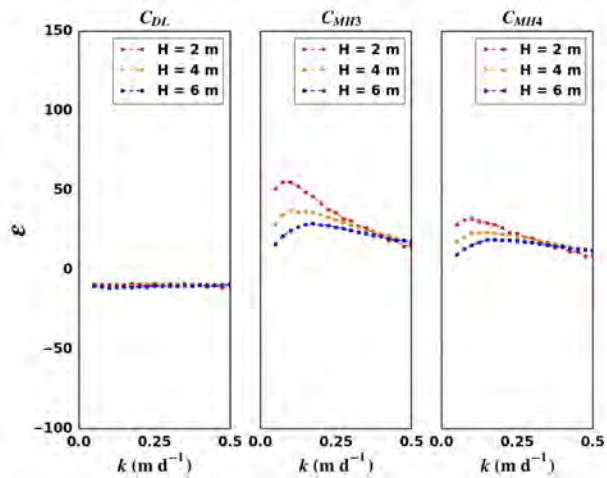


Figure 2.11:  $\epsilon$  for all considered system parameter combinations in the simulations with variable groundwater density flow and a constant hydraulic head at the bottom of the aquifer of 0.1 m.  $k$  is the hydraulic conductivity of the confining layer and  $H$  is thickness of the confining layer.

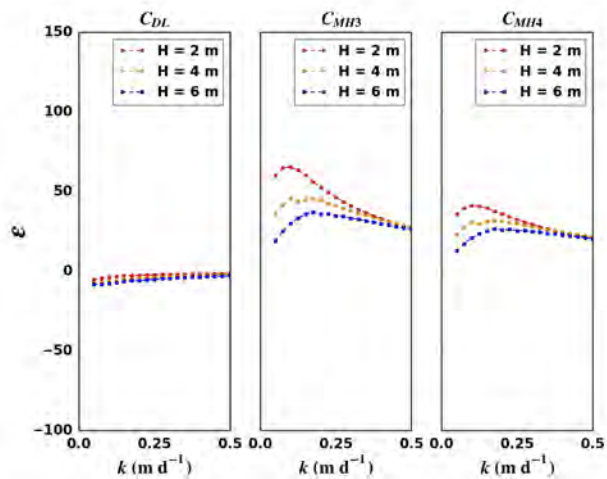


Figure 2.12:  $\epsilon$  for all considered system parameter combinations in the simulations with constant groundwater density flow and a constant hydraulic head at the bottom of the aquifer of 0.1 m.  $k$  is the hydraulic conductivity of the confining layer and  $H$  is thickness of the confining layer.

Table 2.2: Parameter combinations for the investigation of the influence of the simultaneous simulation of ditches and drain tiles, per model number.  $k$  is the hydraulic conductivity of the confining layer,  $L_{dr}$  is the distance between the drains,  $B_{dt}$  is the width of the ditch,  $L_{dt}$  is the distance between the ditches and  $H$  is the thickness of the confining layer.

| Model nr. | $k$ (m d <sup>-1</sup> ) | $L_{dr}$ (m) | $B_{dt}$ (m) | $L_{dt}$ (m) | $H$ (m) |
|-----------|--------------------------|--------------|--------------|--------------|---------|
| 1         | 0.05                     | 5.0          | 5.0          | 60.0         | 2.0     |
| 2         | 0.05                     | 5.0          | 5.0          | 60.0         | 4.0     |
| 3         | 0.05                     | 5.0          | 5.0          | 60.0         | 6.0     |
| 4         | 0.05                     | 5.0          | 5.0          | 180.0        | 2.0     |
| 5         | 0.05                     | 5.0          | 5.0          | 180.0        | 4.0     |
| 6         | 0.05                     | 5.0          | 5.0          | 180.0        | 6.0     |
| 7         | 0.05                     | 5.0          | 5.0          | 240.0        | 2.0     |
| 8         | 0.05                     | 5.0          | 5.0          | 240.0        | 4.0     |
| 9         | 0.05                     | 5.0          | 5.0          | 240.0        | 6.0     |
| 10        | 0.05                     | 5.0          | 10.0         | 60.0         | 2.0     |
| 11        | 0.05                     | 5.0          | 10.0         | 60.0         | 4.0     |
| 12        | 0.05                     | 5.0          | 10.0         | 60.0         | 6.0     |
| 13        | 0.05                     | 5.0          | 10.0         | 180.0        | 2.0     |
| 14        | 0.05                     | 5.0          | 10.0         | 180.0        | 4.0     |
| 15        | 0.05                     | 5.0          | 10.0         | 180.0        | 6.0     |
| 16        | 0.05                     | 5.0          | 10.0         | 240.0        | 2.0     |
| 17        | 0.05                     | 5.0          | 10.0         | 240.0        | 4.0     |
| 18        | 0.05                     | 5.0          | 10.0         | 240.0        | 6.0     |
| 19        | 0.05                     | 5.0          | 15.0         | 60.0         | 2.0     |
| 20        | 0.05                     | 5.0          | 15.0         | 60.0         | 4.0     |
| 21        | 0.05                     | 5.0          | 15.0         | 60.0         | 6.0     |
| 22        | 0.05                     | 5.0          | 15.0         | 180.0        | 2.0     |
| 23        | 0.05                     | 5.0          | 15.0         | 180.0        | 4.0     |
| 24        | 0.05                     | 5.0          | 15.0         | 180.0        | 6.0     |
| 25        | 0.05                     | 5.0          | 15.0         | 240.0        | 2.0     |
| 26        | 0.05                     | 5.0          | 15.0         | 240.0        | 4.0     |
| 27        | 0.05                     | 5.0          | 15.0         | 240.0        | 6.0     |
| 28        | 0.25                     | 10.0         | 5.0          | 60.0         | 2.0     |
| 29        | 0.25                     | 10.0         | 5.0          | 60.0         | 4.0     |
| 30        | 0.25                     | 10.0         | 5.0          | 60.0         | 6.0     |
| 31        | 0.25                     | 10.0         | 5.0          | 180.0        | 2.0     |
| 32        | 0.25                     | 10.0         | 5.0          | 180.0        | 4.0     |
| 33        | 0.25                     | 10.0         | 5.0          | 180.0        | 6.0     |
| 34        | 0.25                     | 10.0         | 5.0          | 240.0        | 2.0     |
| 35        | 0.25                     | 10.0         | 5.0          | 240.0        | 4.0     |
| 36        | 0.25                     | 10.0         | 5.0          | 240.0        | 6.0     |
| 37        | 0.25                     | 10.0         | 10.0         | 60.0         | 2.0     |
| 38        | 0.25                     | 10.0         | 10.0         | 60.0         | 4.0     |
| 39        | 0.25                     | 10.0         | 10.0         | 60.0         | 6.0     |
| 40        | 0.25                     | 10.0         | 10.0         | 180.0        | 2.0     |

Table 2.3: (continuation of Table 2.2)

| Model nr. | $k$ (m d <sup>-1</sup> ) | $L_{dt}$ (m) | $B_{dt}$ (m) | $L_{dt}$ (m) | $H$ (m) |
|-----------|--------------------------|--------------|--------------|--------------|---------|
| 41        | 0.25                     | 10.0         | 10.0         | 180.0        | 4.0     |
| 42        | 0.25                     | 10.0         | 10.0         | 180.0        | 6.0     |
| 43        | 0.25                     | 10.0         | 10.0         | 240.0        | 2.0     |
| 44        | 0.25                     | 10.0         | 10.0         | 240.0        | 4.0     |
| 45        | 0.25                     | 10.0         | 10.0         | 240.0        | 6.0     |
| 46        | 0.25                     | 10.0         | 15.0         | 60.0         | 2.0     |
| 47        | 0.25                     | 10.0         | 15.0         | 60.0         | 4.0     |
| 48        | 0.25                     | 10.0         | 15.0         | 60.0         | 6.0     |
| 49        | 0.25                     | 10.0         | 15.0         | 180.0        | 2.0     |
| 50        | 0.25                     | 10.0         | 15.0         | 180.0        | 4.0     |
| 51        | 0.25                     | 10.0         | 15.0         | 180.0        | 6.0     |
| 52        | 0.25                     | 10.0         | 15.0         | 240.0        | 2.0     |
| 53        | 0.25                     | 10.0         | 15.0         | 240.0        | 4.0     |
| 54        | 0.25                     | 10.0         | 15.0         | 240.0        | 6.0     |
| 55        | 0.5                      | 15.0         | 5.0          | 60.0         | 2.0     |
| 56        | 0.5                      | 15.0         | 5.0          | 60.0         | 4.0     |
| 57        | 0.5                      | 15.0         | 5.0          | 60.0         | 6.0     |
| 58        | 0.5                      | 15.0         | 5.0          | 180.0        | 2.0     |
| 59        | 0.5                      | 15.0         | 5.0          | 180.0        | 4.0     |
| 60        | 0.5                      | 15.0         | 5.0          | 180.0        | 6.0     |
| 61        | 0.5                      | 15.0         | 5.0          | 240.0        | 2.0     |
| 62        | 0.5                      | 15.0         | 5.0          | 240.0        | 4.0     |
| 63        | 0.5                      | 15.0         | 5.0          | 240.0        | 6.0     |
| 64        | 0.5                      | 15.0         | 10.0         | 60.0         | 2.0     |
| 65        | 0.5                      | 15.0         | 10.0         | 60.0         | 4.0     |
| 66        | 0.5                      | 15.0         | 10.0         | 60.0         | 6.0     |
| 67        | 0.5                      | 15.0         | 10.0         | 180.0        | 2.0     |
| 68        | 0.5                      | 15.0         | 10.0         | 180.0        | 4.0     |
| 69        | 0.5                      | 15.0         | 10.0         | 180.0        | 6.0     |
| 70        | 0.5                      | 15.0         | 10.0         | 240.0        | 2.0     |
| 71        | 0.5                      | 15.0         | 10.0         | 240.0        | 4.0     |
| 72        | 0.5                      | 15.0         | 10.0         | 240.0        | 6.0     |
| 73        | 0.5                      | 15.0         | 15.0         | 60.0         | 2.0     |
| 74        | 0.5                      | 15.0         | 15.0         | 60.0         | 4.0     |
| 75        | 0.5                      | 15.0         | 15.0         | 60.0         | 6.0     |
| 76        | 0.5                      | 15.0         | 15.0         | 180.0        | 2.0     |
| 77        | 0.5                      | 15.0         | 15.0         | 180.0        | 4.0     |
| 78        | 0.5                      | 15.0         | 15.0         | 180.0        | 6.0     |
| 79        | 0.5                      | 15.0         | 15.0         | 240.0        | 2.0     |
| 80        | 0.5                      | 15.0         | 15.0         | 240.0        | 4.0     |
| 81        | 0.5                      | 15.0         | 15.0         | 240.0        | 6.0     |

## Chapter 3

# Increasing a freshwater lens below a creek ridge using a controlled artificial recharge and drainage system: a case study in the Netherlands.

This chapter is based on: *Pauw, P.S., Van Baaren, E.S., Visser, M. De Louw, P.G.B and Oude Essink, G.H.P., 2015. Increasing a freshwater lens below a creek ridge using a controlled artificial recharge and drainage system: a case study in the Netherlands. Accepted for publication in Hydrogeology Journal*  
*<http://dx.doi.org/10.1007/s10040-015-1264-z>*

### 3.1 Introduction

#### 3.1.1 Hydrogeology of the Walcheren peninsula

On the Walcheren peninsula, situated in the southwestern part of the Netherlands (Figure 3.1), large areas currently lie at or below mean sea level (MSL). The upper hydrogeological unit in these low-lying areas is an up to 10 m thick semi-confining layer, which consists of Holocene peat, clay, and silt deposits. Below this unit, sandy deposits from the Quarternary and Neogene Periods form a 10 - 80 m thick semi-confined aquifer (Goes et al., 2009; De Louw et al., 2011; Stafleu et al., 2011). In the semi-confined aquifer low-permeable layers are present, but they don't form a coherent confining unit. The Oligocene marine clay that is present below the semi-confined aquifer is considered as the hydrogeological base (TNO,

1997).

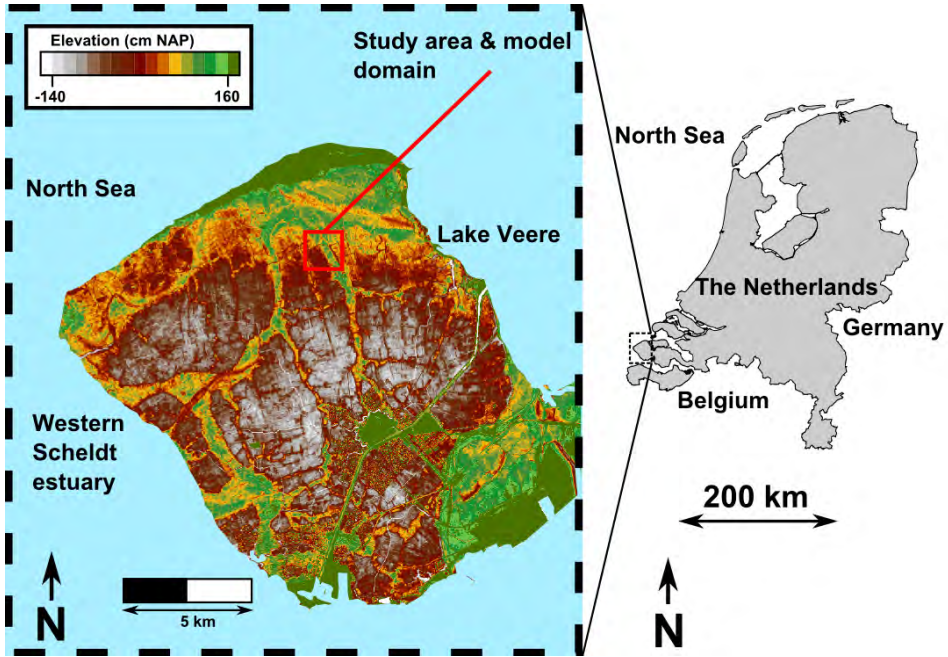


Figure 3.1: Location of the study area (red box), located on the Walcheren peninsula in the southwestern part of the Netherlands. The Walcheren peninsula is surrounded by three surface waters: the North Sea, the Western Scheldt estuary, and Lake Veere.

At many locations of the Walcheren peninsula, Holocene sandy tidal creek deposits fully incise the semi-confining layer and partly incise the underlying aquifer up to a depth of -35 m MSL. A fining up sequence from medium sand to clayey silt is typically present in the upper 2 meters of the sandy tidal creek deposits (Van Meerten, 1986). This is related to the filling up of the tidal creeks, which were present between 700 BC and 750 AD. Around 1200 AD, natural and man-made drainage led to compaction of peat and clay deposits of the tidal flat, which initiated an inversion of the landscape (Figure 3.2) (Ervynck et al., 1999; Vandenhede and Lebbe, 2002). Currently, the sandy creek deposits lie up to 2 m higher than the tidal flat deposits and appear as elevated ridges in the landscape. These geomorphological features are known as 'creek ridges'.

### 3.1.2 Freshwater lenses below creek ridges

Below the creek ridges on the Walcheren peninsula, 5 - 30 m thick freshwater lenses are present. These lenses are an important source for irrigation, as the majority of the groundwater and the surface waters are brackish to saline and there is no transport of fresh surface water from other areas (De Louw et al., 2011). The

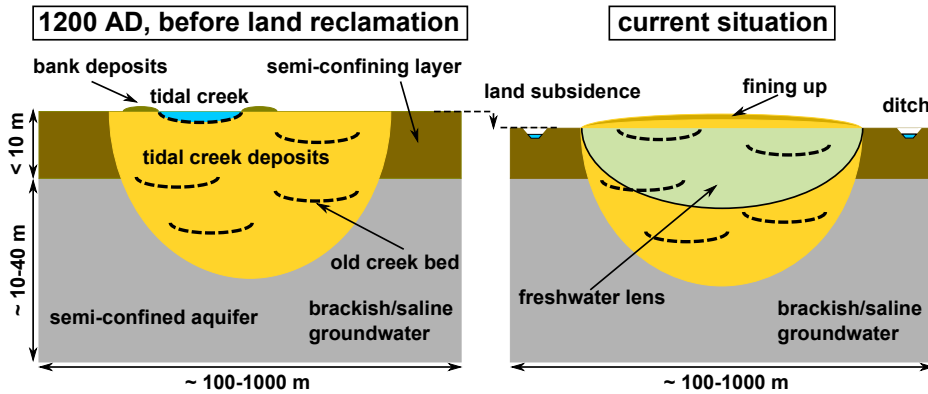


Figure 3.2: Inversion in the landscape due to filling up of the tidal creek followed by drainage of the peat and clay deposits in the semi-confining layer.

amount and rate of fresh groundwater extraction is regulated by the local water board to prevent saltwater upconing and excessive drawdown of the groundwater table (Province of Zeeland, 2002). Currently, the irrigation demand already exceeds the permissible groundwater extraction, which leads to crop damage. As the anticipated sea level rise, climate change, and land subsidence will further jeopardize fresh groundwater resources in the future (Oude Essink et al., 2010; Pauw et al., 2012), measures are necessary to assure a sustainable freshwater supply.

A potential measure for increasing freshwater supply is to increase the freshwater lenses below creek ridges by artificial recharge. Artificial recharge can be achieved by a wide range of methods and is successfully applied in many coastal areas (Stuyfzand, 1993; Bouwer, 2002; Tredoux et al., 2003; Pyne, 2005). In addition to artificial recharge, aquifer storage and recovery (ASR) using wells is a popular method for storing water when available and extracting it when needed (Ward et al., 2007). Recent studies (Miotlinski et al., 2013; Ginkel et al., 2014; Zurbier et al., 2014b) have presented innovative extraction and injection techniques to improve the recovery efficiency of ASR in coastal areas.

In this chapter a new Controlled Artificial Recharge and Drainage (CARD) system is presented, which aims at increasing a freshwater lens below a creek ridge. Field measurements and numerical model simulations were used to investigate the CARD system at a site on a creek ridge on the Walcheren peninsula (Figure 3.1). Using the field and model results, the potential of applying the CARD system elsewhere is qualitatively discussed. The case study that is described here is focused on the hydrological aspects of the CARD system; hydrochemical and economical aspects are only briefly mentioned.

## 3.2 Material and methods

### 3.2.1 Theory and definitions

In this chapter, the classification of the salinity of surface water and groundwater into 'fresh', 'brackish' or 'saline' is based on the electrical conductivity of the water referenced to a temperature of 20°C ( $EC_{w20}$ ). The water is fresh when  $EC_{w20} \leq 2.0 \text{ mS cm}^{-1}$ , the water is brackish when the  $EC_{w20}$  is between 2.0 and 5.0  $\text{mS cm}^{-1}$  and the water is saline in case  $EC_{w20} > 5.0 \text{ mS cm}^{-1}$ . This classification is based on guidelines that farmers in the area use for irrigation; fresh water can be used safely for irrigation, brackish water is only used occasionally in times of severe water scarcity, and saline water is unfit for irrigation.

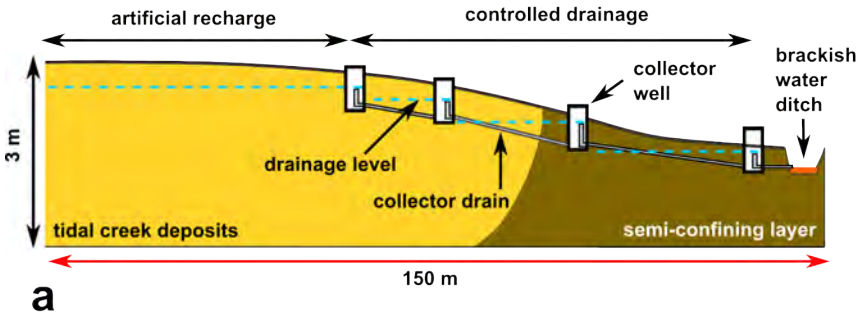
The thickness of the freshwater lens is defined as the depth at which the  $EC_{w20}$  or  $EC_{bulk}$  is equal to 50% of the difference between their maximum and minimum value below the creek ridge, and referred to as  $D_{mix}$  (modified from De Louw et al. (2011)).  $D_{mix}$  approximately corresponds to the center of the mixing zone of the freshwater lens (De Louw et al., 2011). The reason for choosing  $D_{mix}$  instead of the depth of the 'fresh - brackish' interface for the thickness of the freshwater lens, is that from the different geophysical measurement techniques that were used to infer the thickness of the freshwater lens, it was difficult to determine the 'fresh - brackish' interface, as information about the formation factor for the conversion of the  $EC_{bulk}$  (the electrical conductivity of the water and porous medium) to  $EC_{w20}$  using Archie's law (Archie, 1942) was missing.

The CARD system that is described in this chapter aims at increasing the freshwater lens by increasing the groundwater table below the creek ridge in winter, when there is a precipitation excess. The effect of the groundwater table on the thickness of the freshwater lens was explained in the introduction of this thesis using the classical Badon Ghijben - Herzberg principle. Furthermore, it was explained that the two most important assumptions of the Badon Ghijben - Herzberg principle are that 1) no mixing zone is present between the fresh and saline groundwater and 2) the vertical pressure distribution is hydrostatic. In reality, these conditions are never exactly met. Amongst others, groundwater table fluctuations will never result in immediate changes of the thickness of the freshwater lens because hydraulic heads in the subsurface react much faster than the groundwater salinity distribution (Oude Essink, 1996). Nevertheless, on the long term an increase of the freshwater lens can be expected when the time-averaged groundwater table is increased (Eeman et al., 2012), which is the basic idea behind the CARD system.

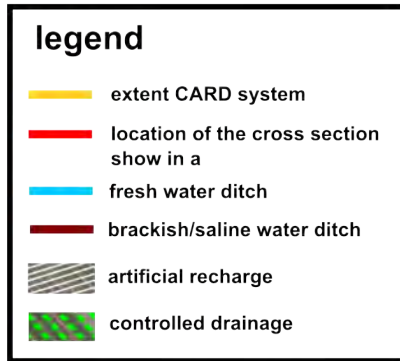
### 3.2.2 Design of the CARD system at the study area

The study area is located on the Walcheren peninsula (Figures 3.1 and 3.4). Within the study area, the focus is on the fields of two farmers (Figures 3.3 and 3.4). The farmers use the fields for crop rotation of cichorium, potatoes, cauliflower, and fennel. In the period 1971 - 2010, the average precipitation excess in autumn and

winter was 261 mm, whereas in spring and summer there was no precipitation excess but net evapotranspiration, which amounted on average 135 mm higher than the precipitation (weather station Vlissingen, ~11 km from the study area (KNMI, 2015)).



**a**



**b**

Figure 3.3: **a** Concept of the CARD system in vertical cross section. Note that the only a part of the semi-confining layer is shown and that the semi-confined aquifer (Figure 3.2) is not. In reality the transition zone between the sandy tidal creek deposits and the semi-confining layer is gradual. **b** Overview of the CARD system in plan view (part of the study area, see Figures 3.1 and 3.4 ). Close and parallel to the cross section in **a**, a ditch is present that separates the fields of two farmers. As this ditch was draining fresh groundwater, a dam was placed in conjunction with the installation of the CARD system to prevent undesirable drainage of fresh groundwater.

In the north and east, the study area is bordered by a 10 m wide ditch (Figure 3.4). The  $EC_{w20}$  of this ditch varies between 3 (winter) and 9 (summer) mS  $cm^{-1}$  due to seepage of saline groundwater. For this reason, the water is unfit for irrigation. In summer, the water level in the ditch is maintained at -1.0 m NAP (the Dutch ordnance datum, approximately equal to MSL) and in winter at -1.2 m

NAP. In between the fields of the two farmers a 1 m wide ditch is present.

In April 2013, the CARD system was installed on the two fields and a dam in the small ditch between the fields of the two farmers was placed to prevent drainage of the fresh groundwater. The drain tiles of the CARD system are composed of plastic perforated tubes of 60 mm with an outer envelope of polypropylene (PP450). The depth of the drain tiles varies between 1.1 m (higher parts of the creek ridge) and 0.8 m (lower parts of the creek ridge) below ground level (BGL). At the higher parts of the creek ridge the distance between the drain tiles is 7 m. Artificial recharge using fresh surface water takes place here. The fresh surface water is collected downstream of a weir just north of the CARD system (Figure 3.3). The weir controls the discharge of fresh surface water into a brackish/saline ditch. Discharge mainly occurs in late autumn, winter, and early spring, as a result of the precipitation excess, so in this period water is available for artificial recharge. The collected freshwater is passed through a 0.2 mm filter (Meeuwse Handelsoederne-ning), is transported over the brackish/saline ditch, and is then pumped into the CARD system at an intake point (Figure 3.3). When the groundwater table is higher than the highest desired drainage level (about 1 m BGL at the highest parts of the creek ridge), the pump automatically turns off. During the other period of the year artificial recharge is generally not possible, as the weir prevents the discharge of fresh water into the brackish/saline ditch.

At the lower parts of the creek ridge, artificial recharge does not take place, but the drainage level is kept as high as possible (between 0.6 to 0.8 m BGL) to reduce the groundwater flow from the higher parts of the creek ridge. A groundwater table higher than 0.6 m BGL at the lower parts of the creek ridge is undesired as it leads to crop damage. In Figure 3.3 it is shown how the drainage level is controlled. Individual drain tiles at 6 m spacing are oriented perpendicular to the plane of Figure 3.3 and are connected to a collector drain. The water in this collector drain discharges into a collector well, where the drainage level can be controlled at the desired level. Additional illustrative pictures of the CARD system are given in the Appendix of this chapter.

### 3.2.3 Field measurements

In Figure 3.4 and Table 3.1 an overview is shown of the measurement locations (ML) and the different field measurements that were used. Prior to the installation of the CARD system, field data of the lithology and  $EC_{bulk}$  was collected for the design of the system and for the calibration of the numerical model. Cone penetration tests (CPTs) were used to determine the vertical distribution of the lithology and  $EC_{bulk}$  at 5 MLs. For the lithology, a friction ratio ( $R_f$ )  $> 2$  was used to indicate sediment with a low permeability, such as clay or peat. The friction ratio is the ratio of the pressure on the tip of the cone and on the sleeve (i.e., the side) of the cone (Lunne et al., 1997). These pressures were recorded together with  $EC_{bulk}$  at a 2 cm interval as the cone was pushed downwards. As the  $EC_{bulk}$  is also influenced by lithology (e.g., clay), the influence of the lithology was qualitatively

considered using  $R_f$ .

Continuous vertical electrical sounding (CVES) measurements were carried out at three transects to estimate the distribution of  $EC_{bulk}$  in a vertical cross section. The ABEM Lund Imaging System, comprising the ABEM SAS 4000 terrameter and the ES10-64 electrode selector (ABEM), was used for this purpose. The Wenner method was used with an electrode distance of 2 m to measure the 'apparent'  $EC_{bulk}$  distribution (Telford et al., 1990). The RES2DINV inversion program (Loke et al., 2006) was used to obtain a model of  $EC_{bulk}$ .

### 3.2.4 Monitoring

After the installation of the CARD system, the groundwater table,  $EC_{bulk}$  and  $EC_{w20}$  were monitored at MLs 1, 2, 4, 5, and 6, for the period May 1, 2013 May 1, 2014. ML 6 served as a reference measurement, as the CARD system was not installed here.

Table 3.1: Overview of the different types of field measurements and their ML. The manufacturers of the devices are: pressure transducers: Schlumberger (The Netherlands), SLIMFLEX: Deltares (The Netherlands), CPT: Fugro (The Netherlands), CVES: ABEM (Sweden), SMD: Imageau (France).

| measurement type               | ML            | purpose                   |
|--------------------------------|---------------|---------------------------|
| pressure transducers           | 1, 2, 4, 6    | groundwater levels        |
| sampling using piezometer nest | 1,4           | $EC_{w20}$                |
| SLIMFLEX                       | 1, 5, 6       | $EC_{bulk}$               |
| CPT                            | 1, 2, 3, 4, 5 | lithology and $EC_{bulk}$ |
| CVES                           | A, B, C       | $EC_{bulk}$               |
| SMD                            | 2             | $EC_{bulk}$               |

At ML 2, a vertical electrical resistivity monitoring system (Subsurface Monitoring Device; SMD) was installed. The borehole for this system was made using pulse drilling with a diameter of about 15 cm. The SMD was used to measure the vertical distribution of  $EC_{bulk}$  at a daily interval, using multiple electrodes located at various depths. The Wenner configuration was used to measure  $EC_{bulk}$ . The electrode spacing was 0.1 m from -6.5 m NAP to -10.3 m NAP. Above and below this section the electrode distance gradually increased to 0.7 m.

At MLs 1 and 4, six 2.5 cm diameter piezometers with a 40 cm long screen were installed at depths where the mixing zone was present before the installation of the CARD system. The borehole was made using rotary flush drilling, with a diameter of about 20 cm. Bentonite plugs in between the screen were used to prevent short-circuiting of the groundwater. About two times the volume of the piezometer was pumped to determine the  $EC_{w20}$ , which was sufficient to obtain a stable value. During the period September 2013 May 2014, the  $EC_{w20}$  was sampled approximately bi-monthly.

In December 2013 and February 2014, electromagnetic (EM) borehole logging using a thin probe (SLIMFLEX) was conducted at MLs 1, 5 and 6. In the probe,

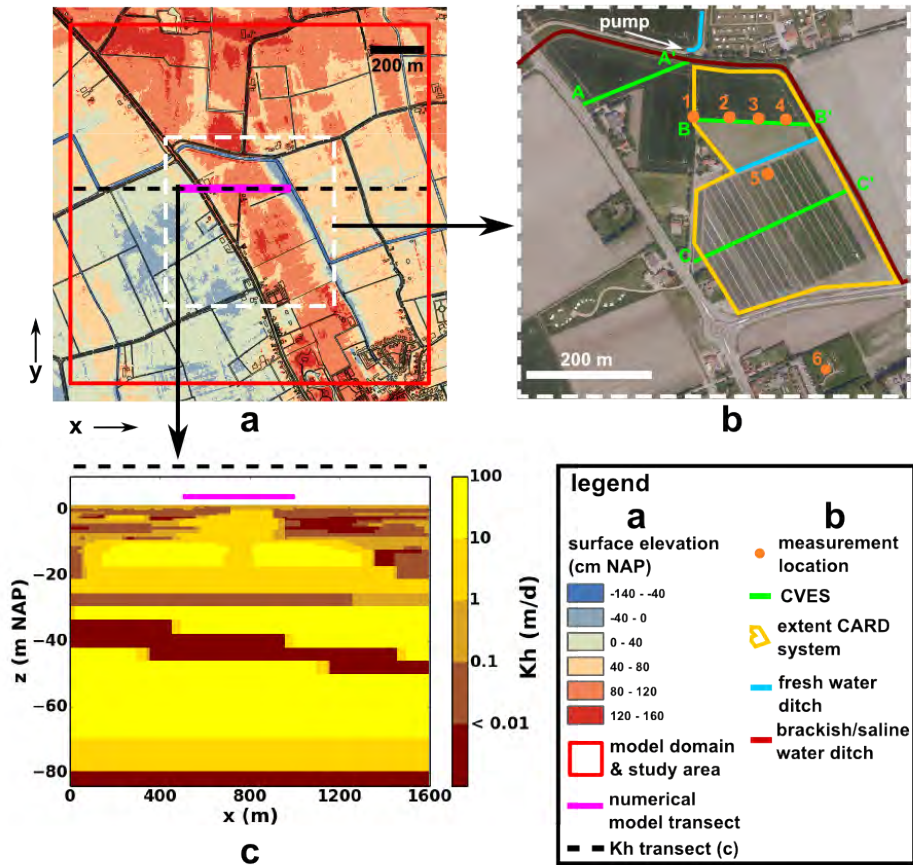


Figure 3.4: **a** The study area (also shown in Figure 3.1) and the horizontal extent of the numerical model in plan view, including the surface elevation. **b** Overview of the horizontal extent of the CARD system, the measurement locations (MLs) and CVES transects. **c** Cross-sectional transect of the horizontal hydraulic conductivity ( $K_h$ ) in the numerical model. This transect is indicated by the black dashed line in **a**. The purple solid line indicates the cross-sectional transect of the numerical model results shown in Figure 3.11. CVES transect B-B' is partly located along this transect, as well as partly along the cross-sectional transect of the horizontal hydraulic conductivity shown in **c**.

an alternating electrical current is generated in a 'transmitting' coil to produce a primary EM field. This primary EM field produces electrical currents in the subsurface which lead to a secondary EM field. Both fields are measured in another coil at 50 cm distance from the transmitting coil. From the difference in amplitude and phase lag of the EM fields,  $EC_{bulk}$  can be determined (McNeill, 1980).

At MLs 1, 2, 4, and 6, groundwater levels were recorded at a 10 min interval

using pressure transducers installed in piezometers. The piezometers had a 40 cm screen at the bottom, and the screens were located at 4 m from the surface. The borehole for the piezometer was made using hand pulse drilling equipment. The pressure transducers were read out, compared with manual measurements and re-installed approximately bi-monthly. The maximum difference between the manual measurement and the recorded pressure was 4 cm.

### 3.2.5 Numerical model

#### Set-up of the initialization model

SEAWAT (Langevin et al., 2007) was used to simulate variable density groundwater flow and salt transport at the study area (Figure 3.4b). The horizontal extent of the model is 1600 by 1600 m and discretized using cells of 10 by 10 m. The vertical extent of the model is from +1.5 m NAP to -87.0 m NAP. Up to a depth of -25 m NAP the model layers are 0.5 m thick. The hydraulic conductivity distribution in this section was based on the geological model GEOTOP (Stafleu et al., 2011). Below -25 m NAP, the thickness of the model layers increases to up to 5 m at the bottom of the model. The hydraulic conductivity distribution in this section was based on the regional hydrogeological model REGIS II (REGIS, 2004). The vertical anisotropy ratio (the horizontal hydraulic conductivity ( $K_h$ ) divided by the vertical hydraulic conductivity ( $K_v$ )) in the numerical model is 1.4. In Fig. 3.4c a cross section of  $K_h$  in the numerical groundwater model is shown, which indicates the incision of the semi-confining layer by the more permeable sediment below the creek ridge. The effective porosity (0.3), confined storage coefficient ( $1E-5 m^{-1}$ ), specific yield (0.15), longitudinal dispersivity (0.1 m), transverse dispersivity (0.01 m), and the molecular diffusion coefficient ( $8.64E-5 m^2d^{-1}$ ) were assumed to be constant in the model. These parameters were estimated from literature (Domenico and Schwartz, 1990) and from groundwater flow studies in the coastal plain of the Netherlands (Oude Essink et al., 2010; De Louw, 2013; Zuurbier et al., 2014a) and Belgium (Lebbe, 1999; Vandenbohede and Lebbe, 2006).

First, an initialization model was constructed in which the development of a freshwater lens below the creek ridge was simulated, starting from an initially saline domain. The salt concentration was represented by  $EC_{w20}$ . The maximum value of  $EC_{w20}$  corresponds to the maximum measured  $EC_{w20}$  ( $40.6 mS cm^{-1}$  at a depth of -18 m NAP). This is also the initial concentration of the initialization model. The density of the water with  $EC_{w20} = 40.6 mS cm^{-1}$  was calculated at  $1022.3 kg m^3$ , following the method of Post (2012). The minimum concentration of the groundwater is 0 and corresponds with a density of  $1000 kg m^3$ . The water density ( $\rho_w$ ) varies linearly with  $EC_{w20}$ :

$$\rho_w = 1000 \beta EC_{w20} \quad (3.1)$$

with  $\beta = (1025-1000) kg m^3 / 40.6 mS cm^{-1}$ .

The PCG package was used for solving the variable density groundwater flow equation. The hydraulic head closure criterion was  $10^{-5}$  m, the flux closure criterion was  $0.1 \text{ m}^3$ . The advection term of the solute transport equation was solved using the MOC solver, with a minimum number of 9 particles per cell. A Courant number of 1.0 was used. The sink and source and the hydrodynamic dispersion terms of the solute transport equation were solved using the GCG solver, with a relative concentration closure criterion of  $10^{-6}$ .

Stress periods of 6 months were used, representing winter and summer conditions. The recharge rate in winter ( $1.5 \text{ mm d}^{-1}$ ) and the evapotranspiration rate in summer ( $-0.02 \text{ mm d}^{-1}$ ) were based on average data (period 1971-2000) from a nearby weather station (station Vlissingen,  $\sim 11 \text{ km}$  from the study site, (KNMI, 2015)). For the evapotranspiration, crop factors based on the crops on the field of the farmers were taken from Hooghart and Lablans (1988), to correct for the reference Makkink evapotranspiration (Makkink, 1957). At the vertical sides of the model, a head-dependent flux boundary condition was applied with the GHB package, using hydraulic heads and concentrations taken from a larger-scale model (Van Baaren et al., 2011). The conductance value was set to  $1 \text{ m}^2 \text{ d}^{-1}$ . Testing showed that an order of magnitude larger or lower value for the GHB conductance did not significantly change the model results at the study site. This was in line with the expectations, as the boundaries were located relatively far from the area of interest (i.e., the two fields of the farmers where the CARD system was installed). The bottom of the model is a no-flow boundary condition as it corresponds with the hydrogeological base. Ditches were simulated in the model using the RIVER package of SEAWAT. Tile drainage was modeled using the DRAIN package. The conductance for the cells where the RIVER or DRAIN packages were used was based on the methods of De Lange (1999) and Pauw et al. (2014). In the Appendix of this chapter, more information on the input parameters of the DRAIN and RIVER conductance is given.

### Calibration of the initialization model and sensitivity analysis

The initialization model was ended at the moment the thickness of the freshwater lens below the creek ridge ( $D_{mix}$ ) reached a virtually stable value. The simulated end-thickness of the freshwater lens was compared with the thickness of the freshwater lens as measured by the CPTs. The thickness of the freshwater lens was overestimated in the model using the parameters that were described in the previous section. Therefore, the model was calibrated to obtain a better match with the field observations. For the calibration the groundwater recharge rate in winter was reduced, as this was considered the most probable parameter to change. The reason for this is related to ponding, which frequently occurs at the field site due to the low permeability near the surface of the creek ridge (due to the fining up sequence). Due to ponding, the groundwater recharge is lower than the calculated value as described in the previous section (Healy, 2010; Voortman, 2010).

Evidently, other model parameters such as the hydraulic conductivity can also influence the thickness of the freshwater lens. Due to the long runtime of the ini-

tialization model (approximately one week on a modern desktop PC), however, an extensive calibration based on various combinations of different model parameters was not conducted. Instead, the sensitivity of individual model parameters was investigated, using the optimized groundwater recharge in winter. To realize a thinner freshwater lens, the evapotranspiration rate in summer was increased to  $0.4 \text{ mm d}^{-1}$ . This value is comparable with the anticipated increase of the evapotranspiration rate in summer due to climate change (De Louw, 2013; KNMI, 2015). In addition, the hydraulic conductivity in the upper 15 m below the higher parts of the creek were multiplied by a factor of two to decrease the thickness of the freshwater lens. As the conductance of the RIVER and DRAIN cells was based on various assumptions (see the Appendix of this chapter), the effect of a two times higher and two times lower value was also investigated.

### **Scenario simulations to investigate the effect of the CARD system**

The simulated hydraulic heads and concentrations at the end of the calibrated initialization simulation were used as initial condition for three scenario simulations. The effect of the CARD system on the thickness of the freshwater lens was simulated in the three scenarios. In addition, a 'reference' simulation where the CARD system was not simulated was used for comparison with the three scenario simulations. In all four simulations, the yearly period May 1, 2013 – May 1, 2014 was simulated using weekly stress periods. The recharge and evapotranspiration rates were based on data from a nearby weather station (station Vlissingen, ~11 km from the study site (KNMI, 2015)). The yearly period was repeated to cover a period of 10 years to study a long-term effect of the CARD system.

In scenario 'A' the influence of the CARD system on the thickness of the freshwater lens was simulated. The RIVER package was used to represent infiltration and drainage by the drain tiles of the CARD system. The 'stage' of each cell where the RIVER package was applied was based on the weekly average hydraulic heads that were measured at MLs 1, 2 and 4. Due to the surface elevation, the hydraulic heads are higher at MLs 1 and 2 than at ML 4. Therefore, at MLs 1 and 2 the assigned stages mainly result in infiltration, whereas at ML 4 this mainly results in drainage. For verification of this approach, the simulated artificial recharge was compared with the measured artificial recharge at the pump at the intake point of the CARD system. Further details on the simulation of the CARD system are available in the Appendix of this chapter.

The effect of a lower availability of fresh surface water for infiltration was investigated in scenario 'B', by simulating a 0.1 m lower groundwater table during the winter period (i.e., November 1, 2013 – May 1, 2014) compared to scenario A. In scenario 'C', a 0.1 m higher groundwater table compared to scenario A was simulated to investigate the effect of a higher groundwater table.

## 3.3 Results

### 3.3.1 Field measurements

#### Geology

In Figure 3.5 and Table 3.2 the results of the CPTs at MLs 1-5 are shown. The  $R_f$  in the CPTs at MLs 1, 2, and 5, at the higher parts of the creek ridge, is larger than 2 in the upper 1-2 m, indicating the fining-up sequence that is typically found below the creek ridges. Below the fining up sequence the  $R_f$  decreases, which indicates sandy tidal deposits. In the CPTs at MLs 3 (in between the higher and lower parts) and 4 (at the lower parts of the creek ridge), the  $R_f$  is larger than 2 over a larger part of the upper section due to the presence of silt, clay, and peat deposits, which form the semi-confining layer. Note that the semi-confining layer is also indicated by the GEOTOP model (Figure 3.4).

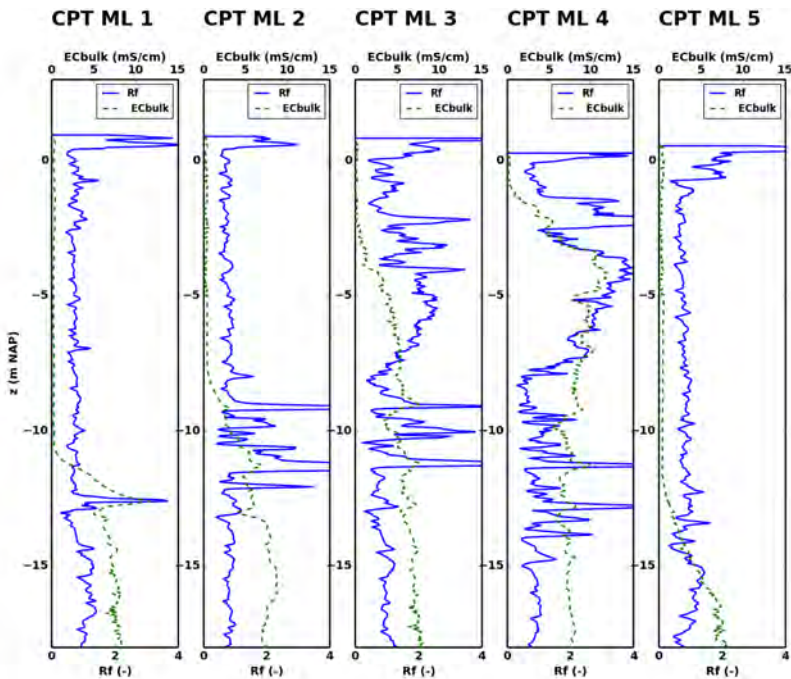


Figure 3.5:  $EC_{bulk}$  and  $R_f$  measured by the CPTs at MLs 1-5 (Figure 3.4).

At larger depth, the CPT at ML 1 indicates low permeable sediment between -12 and -12.5 m NAP. This is also observed in the CPTs at MLs 2, 3, and 4, but at different depths between -8.0 m and -15.0 m NAP. In the CPT at ML 5, low permeable sediment at depth seems to be absent. The sections of low permeable

sediment are interpreted as bank deposits of the former creek system. This type of heterogeneity is not present in the GEOTOP model. In the Appendix of this chapter the  $R_f$  is shown in combination with the vertical hydraulic conductivity at MLs 1-5.

### $EC_{bulk}$ prior to the installation of the CARD system

In Figure 3.6 the inversion results of the CVES transects A-A', B-B', and C-C', are shown. The  $EC_{bulk}$  values  $\leq 2 \text{ mS cm}^{-1}$  indicate the freshwater lens in the sandy deposits below the creek ridge. Further down, the  $EC_{bulk}$  increases relatively fast, which indicates the transition towards the ambient saline groundwater. CVES transect C-C' indicates a thicker freshwater lens compared to CVES transects A-A' and B-B'. This is in line with the difference in  $D_{mix}$  between the CPT at ML 5 and the CPTs at MLs 1 and 2 (Figure 3.5 and Table 3.2), and shows that the freshwater lens increases towards the south. CVES transect B-B' indicates a 0.5 - 1.0 m lower  $D_{mix}$  than the CPTs at MLs 1-4, which can be attributed to the lower vertical resolution in the CVES compared to the CPTs (Reynolds, 1997). As expected, at the higher parts of the creek ridge (MLs 1, 2, and 5)  $D_{mix}$  in the CPTs and the CVES was found at a larger depth than at the lower parts (ML 4).

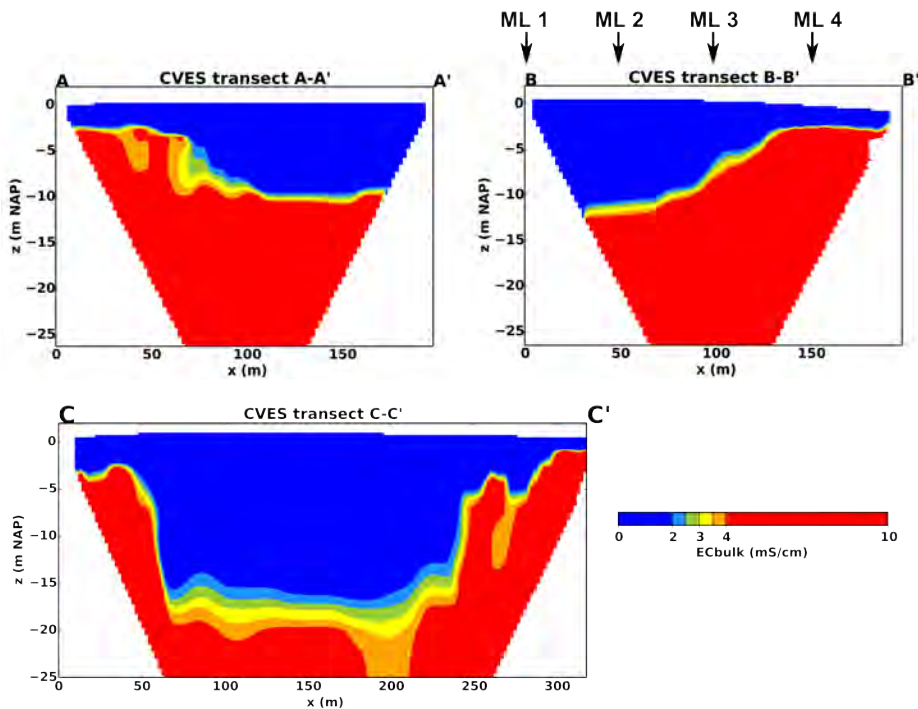


Figure 3.6: Inversion results ( $EC_{bulk}$ ) of the CVES transect A-A, B-B, and C-C.

Table 3.2: Estimated  $D_{mix}$  from the CPTs and simulated  $D_{mix}$  in the numerical model at MLs 1-5. The estimation of  $D_{mix}$  is influenced by clay in the subsurface, which influences the  $EC_{bulk}$  measured in the CPTs. The uncertainty in the estimated  $D_{mix}$  associated with this is 0.5 m.

| name | ML | surface elevation (m NAP) | $D_{mix}$ (m NAP) | modeled $D_{mix}$ (m NAP) |
|------|----|---------------------------|-------------------|---------------------------|
| CPT1 | 1  | 1.08                      | -12.0             | -13.0                     |
| CPT2 | 2  | 0.99                      | -11.0             | -12.5                     |
| CPT3 | 3  | 0.94                      | -5.0              | -11.5                     |
| CPT4 | 4  | 0.37                      | -2.0              | -1.0                      |
| CPT5 | 5  | 0.68                      | -14.5             | -14.0                     |

### Monitoring of $EC_{bulk}$ and $EC_{w20}$

In Figure 3.7 the daily precipitation and the hydraulic heads relative to NAP at ML 1 are shown. From approximately halfway October 2013 until halfway April 2014 the groundwater table could be maintained at a level between 0.2 and -0.2 m NAP. After halfway April 2014 the groundwater table gradually dropped as the artificial recharge stopped. This was because the discharge of fresh surface water over the weir at the water collection point ceased.

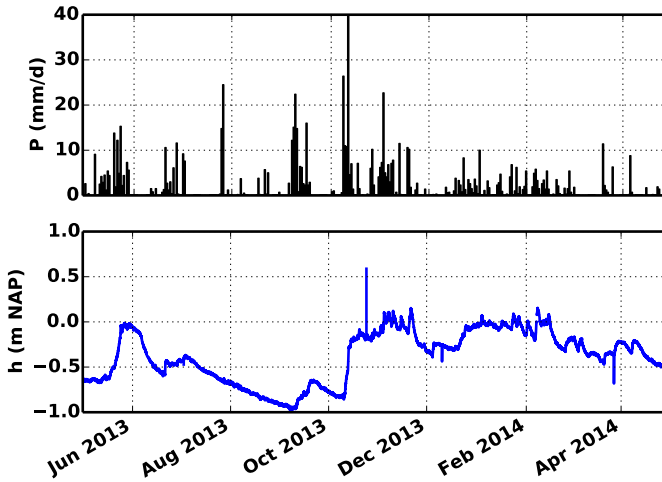


Figure 3.7: Daily precipitation rate ( $P$ , in  $\text{mm d}^{-1}$ ) and hydraulic heads relative to NAP ( $h$ , in m). The surface level is located 1.08 m NAP. The month indications on the horizontal axis indicate the first day of that month.

The results of the  $EC_{w20}$  sampling at ML 1 are shown in Figure 3.8.  $D_{mix}$  on September 20, 2013 (prior to the start of the artificial recharge), which was determined at the depth where  $EC_{w20}$  was equal to  $20.3 \text{ mS cm}^{-1}$ , was about equal to -12 m NAP. This agrees well with  $D_{mix}$  derived from CPT at ML 1 (Figure 3.5 and

Table 3.2). Between September 20, 2013 and March 28, 2014 the freshwater lens increased about 2 m. The sampling results of May 1, 2014 indicate a slight decrease (about 0.05 m) of the freshwater lens between March 28, 2014 and May 1, 2014. At ML 4, the  $EC_{w20}$  at all depths was higher than  $30 \text{ mS cm}^{-1}$  and did not change significantly during the monitoring period, indicating that no significant freshening occurred at this location.

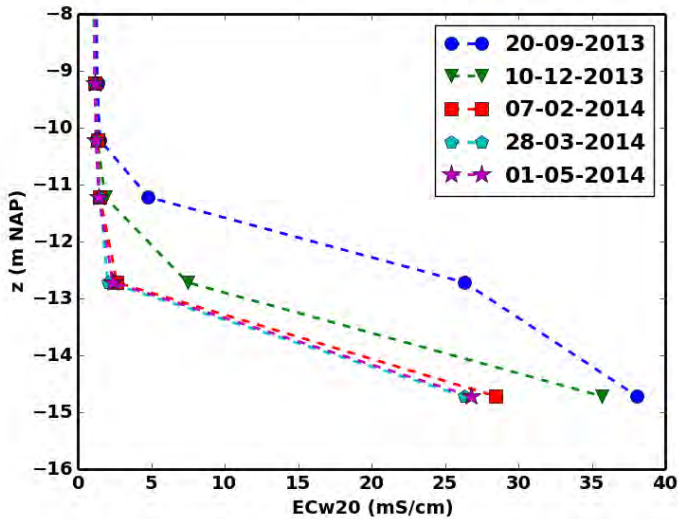


Figure 3.8:  $EC_{w20}$  ( $\text{mS cm}^{-1}$ ) at six depths during 5 monitoring rounds at ML 1.

In Figure 3.9 the development of  $EC_{bulk}$  measured by the SMD at ML 2 is shown during the monitoring period. The decrease of  $EC_{bulk}$  indicates that freshening took place in between -8.0 and -12.0 m NAP. A remarkable feature of Figure 3.9 is the relative constant  $EC_{bulk}$  around  $z = -9.0$  and around -10.5 m NAP. This is attributed to a high clay content in the sediment at these depths. Therefore, the permeability at this depth is expected to be low. The observed freshening can be explained by two processes. The first, which is considered the most likely process, is that the freshening below -9.0 m NAP does not take place from above (i.e., through the clay-rich sediment), but by preferential flow through sections where the hydraulic conductivity is higher. This hypothesis is strengthened by the CPTs which indicated that the low-permeable sections at the higher parts of the creek ridge do not constitute a continuous unit. The second explanation is that the clay-rich section is still permeable enough to transmit fresh groundwater from above.

The SLIMFLEX measurement at ML 1 (Figure 3.10) showed that  $D_{mix}$  decreased by about 0.8 m in the period between December 10, 2013 and February 7, 2014. This agrees well with the sampling results for this ML (Figure 3.8). The

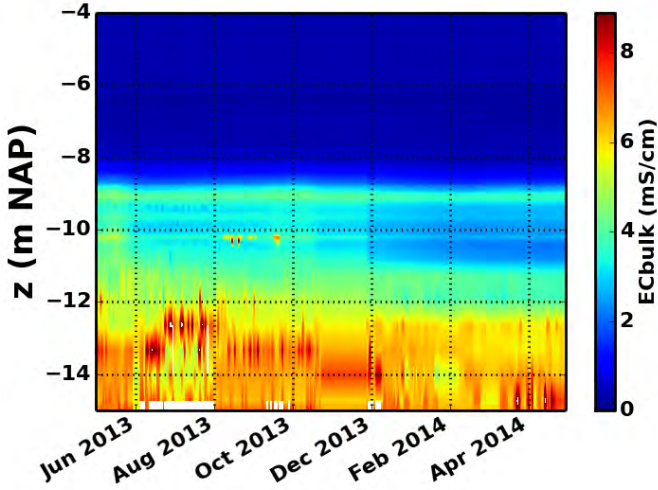


Figure 3.9: Development of the  $EC_{bulk}$  in the period May 1, 2013 – May 1, 2014 relative to NAP, obtained from the SMD at ML 2. The month indications on the horizontal axis indicate the first day of that month. The erratic pattern of  $EC_{bulk}$  between -12 and -15 m NAP is attributed to measurement errors and should therefore be ignored.

SLIMFLEX measurements at ML 5 showed a decrease of  $D_{mix}$  of about 0.5 m. At ML 6 (the reference ML) the SLIMFLEX measurements showed no significant changes in  $D_{mix}$ . This was expected, as the CARD system was not installed here.

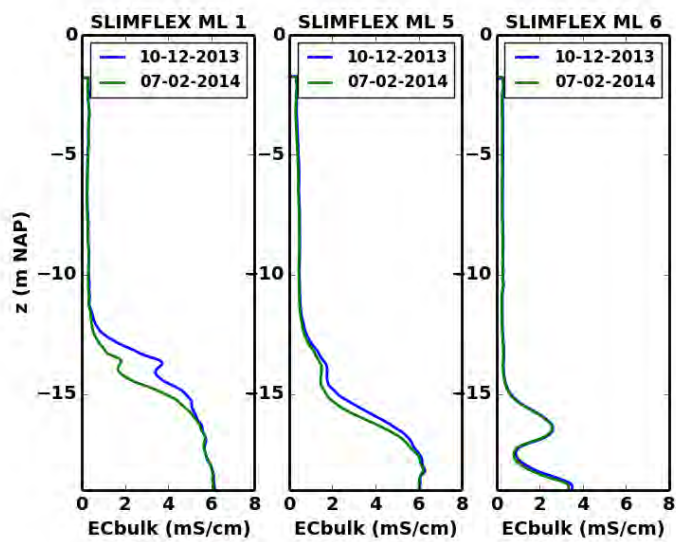


Figure 3.10:  $EC_{bulk}$  relative to NAP at MLs 1, 5, and 6, obtained using the SLIMFLEX measurements.

### 3.3.2 Numerical simulations

#### Initialization model

In Figure 3.11a  $D_{mix}$  is shown in plan view at the end of the initialization model with the calibrated winter recharge rate of  $1.2 \text{ mm d}^{-1}$ . 230 years of simulation time were needed to reach a steady state position of  $D_{mix}$ .  $D_{mix}$  shows a clear relation with the elevation map (Figure 3.4). At the creek ridge the drainage level and the groundwater table are higher than the surrounding lower lying areas. Therefore, the freshwater lens is also thicker here. This is also indicated in Figure 3.11b, where the simulated  $EC_{w20}$  at the end of the initialization model is shown in vertical cross section. In the areas with a low drainage level and low permeable sediment at the surface, the lenses are thinner, presumably due to upward flow of saline groundwater (De Louw et al., 2011). The low water level (-1.2 m NAP) of the 8 m wide ditch that dissects the creek ridge north of the CARD system has a negative impact on the thickness of the freshwater lens, as  $D_{mix}$  below the ditch is found shallower than further away from the ditch.

The simulated  $D_{mix}$  was compared with the  $D_{mix}$  estimated from the CPTs at MLs 1-5. These results are shown in Table 3.2. At ML 5, situated at the higher part of the creek ridge, the simulated  $D_{mix}$  is within the estimated uncertainty (0.5 m) of the measured  $D_{mix}$ . At this ML, the CPT indicated no low-permeable sediment (Figure 3.5). At ML 1, also situated at the higher part of the creek ridge, the difference between the simulated and measured  $D_{mix}$  is larger (1.0 m) than at ML 1. This difference is attributed to the presence of low-permeable sediment at ML 1, indicated by the increase of the friction ratio  $R_f$ , and the absence of this low-permeable sediment in the numerical model. At MLs 2 and 3, which are situated between the high and low parts of the creek ridge, the CPTs indicated more sections of low permeable sediment than at ML 1. These sections are also not present in the numerical model. Therefore, the difference between the measured and simulated  $D_{mix}$  is higher than at ML 1. At ML 4 the difference between the simulated and measured  $D_{mix}$  was comparable to the difference at ML 1. At this low-elevated ML the CPT indicated low-permeable sediment up to about -8.0 m NAP, which is interpreted as the semi-confining layer. In the numerical model the semi-confining layer is also present, which explains smaller difference between the simulated and measured  $D_{mix}$  compared to MLs 2 and 3. In the Appendix of this chapter further information on the comparison between the CPTs and the numerical simulations is given.

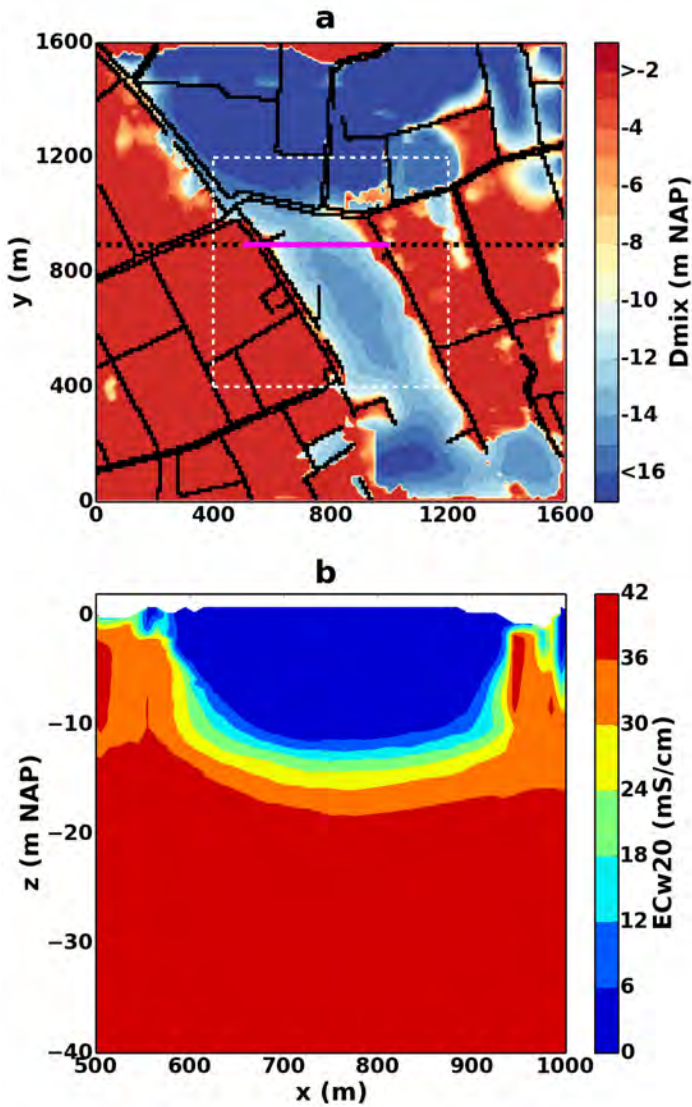


Figure 3.11: **a**  $D_{mix}$  in the initialization model in plan view, using the calibrated groundwater recharge. The white dashed square shows the focus area of the results of the scenario models (Figure 3.13). The black solid lines indicate ditches. The black dashed line indicates the location of the vertical cross section of the hydraulic conductivity distribution in the model (Figure 3.4). The purple solid line indicates the cross section of the simulated  $EC_{w20}$ , shown in **b**.

## Sensitivity analysis

The sensitivity of the different parameters was investigated using the simulated  $EC_{w20}$  and  $D_{mix}$  at MLs 1 and 5, as at these locations measurements of  $D_{mix}$  were also available. The most important observation from Figure 3.12 is that the variations in groundwater recharge and hydraulic conductivity have a larger influence on  $D_{mix}$  than variations in the DRAIN and RIVER conductances. The simulation with a higher groundwater recharge rate in winter showed a 10% thicker freshwater lens at ML 5 compared to the simulation with the calibrated groundwater recharge. In the simulation with a higher evapotranspiration rate in summer, the thickness of the lens at ML 5 was about 10% less than the thickness of the freshwater lens in the simulation with the calibrated groundwater recharge.

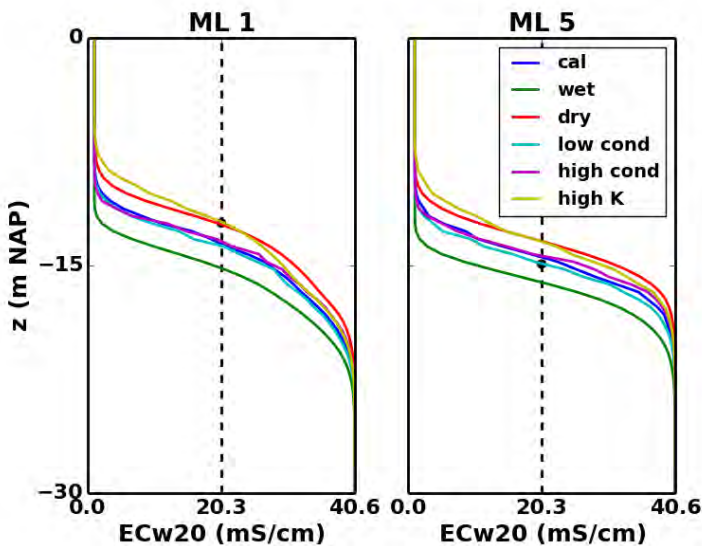


Figure 3.12: Results of the calibration and sensitivity analysis. The simulated  $EC_{w20}$  as a function of depth is shown for the simulation with the calibrated groundwater recharge ('cal') and the other simulations of the sensitivity analysis. 'wet' is the simulation where the groundwater recharge in winter was  $1.5 \text{ mm d}^{-1}$ , 'dry' is the simulation where the evapotranspiration was  $0.4 \text{ mm d}^{-1}$ , 'high K' is the simulation where the hydraulic conductivity (both  $K_h$  and  $K_v$ ) below the higher parts of the creek ridge where increased by a factor of 2, and 'low cond' and 'high cond' are the simulations where the conductance of cells where the RIVER or DRAIN were used was decreased and increased by a factor of 2, respectively. The black dots indicate the measured  $D_{mix}$  at MLs 1 and 5.

## Effect of the CARD system

In the reference simulation, where the CARD system was not simulated,  $D_{mix}$  varied about 0.1 m during a year at ML 1 (Figure 3.13). After 10 years of simulation,  $D_{mix}$  lowered about 0.6 m, which can be explained by the slightly higher recharge rate that was applied in Scenario A compared to the recharge rate of the initialization model.

In scenario A, where the CARD system using the measured groundwater levels was simulated, the groundwater table in winter was about 0.5 m higher than in the reference simulation during the winter period, which led to a lowering of  $D_{mix}$  (Figure 3.13). At the end of the first artificial recharge period,  $D_{mix}$  at ML 1 was about 1.4 m lower than in the reference simulation (Figure 3.13b). This lowering of  $D_{mix}$  is an underestimation of about 0.6 m compared to the CPT and SLIMFLEX measurements. The difference between the simulated and measured lowering of  $D_{mix}$  is attributed to the initialization model, where the simulated  $D_{mix}$  at ML 1 which was about 1 m lower than the measured  $D_{mix}$  (Table 3.2). A deeper  $D_{mix}$  has an attenuating effect on the lowering of  $D_{mix}$  as a result of the increase of the freshwater lens, which can also be deduced from Figure 3.13b. At ML 5, where the difference between the measured and simulated  $D_{mix}$  in the initialization model was smaller than at ML 1, the difference between the measured and simulated lowering of  $D_{mix}$  was also smaller than at ML 1; the SLIMFLEX results between December 10, 2013 and February 7, 2014 indicated a 0.5 m increase of the lens, which also agrees well with the simulated increase of the lens (0.3 m). The decrease of the freshwater lens due to buoyancy during the summer months is much less than the increase of the fresh water lens during the artificial infiltration, which indicates a net increase of the freshwater lens over a year.

After 10 years of simulation,  $D_{mix}$  increased about 6 m in depth at ML 1 and about 8 m at ML 5 in scenario A (Figure 3.13b). The lens has not reached its end-thickness after 10 years, but the freshening rate has considerably decreased. In scenario B, where the effect of a 0.1 m lower groundwater table in the CARD system was investigated, the increase of  $D_{mix}$  in depth is less than in scenario A. At ML 1 the increase was about 5 m and at ML 5 about 6 m. After 10 years, the freshwater lens has almost reached a new dynamic equilibrium. As expected, in scenario C, where the effect of a 0.1 m higher groundwater table in the CARD system was investigated, the increase of  $D_{mix}$  in depth is larger than in scenario A. At ML 1 the increase is about 8 m at ML 1 and 10 m at ML 5. For brevity, the results of scenarios B and C (analogous to Figure 3.13) are given in the Appendix of this chapter. The differences in the scenarios A, B, and C indicate the significant effect of increasing the groundwater table below the creek ridge on the thickness of the freshwater lens.

In Figure 3.14 the simulated volume of the increase of the freshwater lens below the CARD system ( $dV - lens$ ) and the simulated volume of artificial recharge ( $V - AR$ ) at the end of each artificial recharge period are shown cumulatively over the 10 year period, for the three scenarios. The total simulated volume of

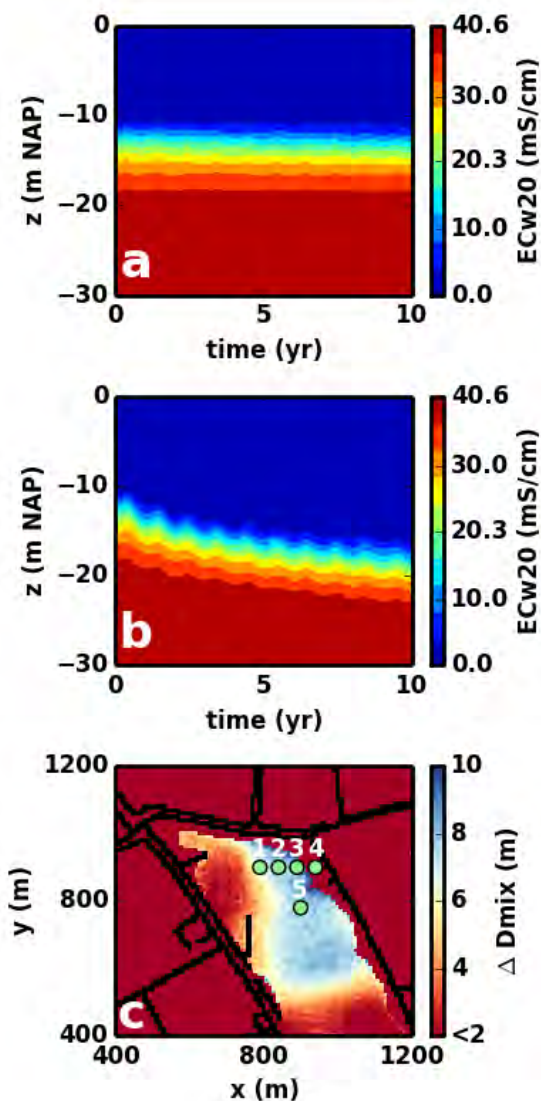


Figure 3.13: **a** Simulated  $EC_{w20}$  contours as a function of depth and time at ML 1 the reference simulation. **b** Simulated  $EC_{w20}$  contours as a function of depth and time at ML 1 in scenario A. **c** difference in  $D_{mix}$  ( $\Delta D_{mix}$ ) between the reference simulation and scenario A, after 10 years of simulation time. The black solid lines indicate ditches. The green dots and the white numbers indicate the MLs.

the freshwater lens below the CARD system at the end of the initialization model was  $373088 \text{ m}^3$ . The total simulated natural groundwater recharge volume below

the CARD system per artificial recharge period was  $27444 \text{ m}^3$ .  $V - AR$  during the first infiltration year in scenario A ( $25052 \text{ m}^3$ ) was about equal to the simulated natural groundwater recharge.  $V - AR$  was higher than the measured volume of the artificial infiltration ( $18905 \text{ m}^3$ ). This difference is partly attributed to the presence of low-permeable sediment indicated by the CPTs and the absence of this sediment in the numerical model. Other factors, such as a difference in simulated and actual groundwater recharge or hydraulic properties, can influence the simulated volume of artificial recharge, but the underlying causes of this discrepancy were not further investigated.  $V - AR$  decreases from  $25052 \text{ m}^3$  in the first year to  $16702 \text{ m}^3$  in year 10 of scenario A. In the first 4 years,  $dV - lens$  is larger than  $V - AR$  (not shown in Figure 3.14), which indicates the contribution of the natural groundwater recharge to the increase of the freshwater lens. In the last 6 years,  $dV - lens$  is smaller than  $V - AR$ . The yearly storage efficiency (i.e,  $dV - lens / V - AR * 100\%$ ) in the last 6 years decreases from 90% to 58%.

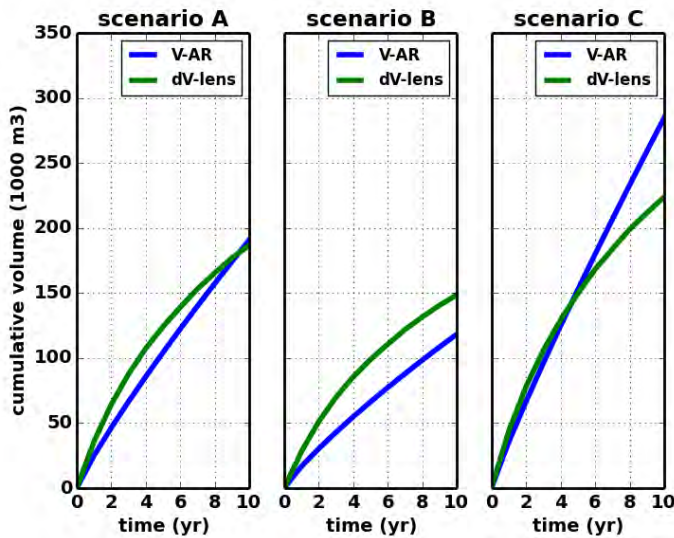


Figure 3.14: The volume of the increase of the freshwater lens below the CARD system ( $dV - lens$ ) and the volume of artificial recharge ( $V - AR$ ) at the end of each artificial recharge period, cumulatively over the 10 year period for the three scenarios.

In scenario B, where the effect of a lower availability of fresh surface water for artificial infiltration was simulated by considering a 0.1 m lower groundwater table below the creek ridge compared to scenario A, the total increase of the volume of the freshwater lens at the end of the 10-year simulation is  $38370 \text{ m}^3$  less than in scenario A. Furthermore,  $72764 \text{ m}^3$  less water was artificially recharged. The storage efficiency in scenario B is higher than in scenario A. In the first 7 years,  $dV - lens$  is larger than  $V - AR$ . In the last 3 years the storage efficiency is less

than 100% and decreases from 94% to 80%.

In scenario C the effect of a 0.1 m higher groundwater table below the creek ridge compared to scenario A was investigated. As expected, the total increase of the volume of the freshwater lens at the end of the 10-year simulation was higher than in scenarios A and B. The total volume of artificial recharge was also higher (Figure 3.14). The storage efficiency was less compared to scenarios A and B. Only in the first two years  $dV - lens$  is larger than  $V - AR$ . In the following years, the storage efficiency decreases from 94% to 48%. Therefore, the higher the groundwater table below the creek ridge, the larger the increase of the freshwater lens, the more water is needed for artificial infiltration, and the lower the storage efficiency.

### 3.4 Discussion

The results of this chapter indicated the hydrological potential of the CARD system for increasing a freshwater lens below a creek ridge. As much as the hydrological potential was thoroughly investigated, other aspects related to the implementation of the CARD system were not in the scope of this study. The effects of chemical, biological, and mechanical clogging of the CARD system were not investigated. Belcher and D'Itri (1995) described the ambiguous experiences regarding the influence of clogging on controlled drainage in their summary of a collection field experiments on controlled drainage and sub-irrigation systems. Clogging will depend on the local conditions, such as soil type, infiltration regime and the amount of suspended solids in the infiltration water. Further research is needed to determine the effect of clogging of the CARD system. Furthermore, although the CARD system is intended to be a relative cheap method for artificial infiltration, the economical aspects of the CARD system need to be investigated in detail.

The hydrological investigation that was presented also has limitations. An important reason for this is the long simulation time of the models that were used. For this reason, the amount of simulations for the calibration, the sensitivity analyses and the scenarios were limited. Future work should focus on a constructing a computationally efficient model which can be used to better estimate the uncertainty and sensitivity of the model parameters. Such a model can also be used to more extensively investigate the influence of the availability of surface water for artificial recharge on the thickness of the freshwater lens. Although the aspects that control the thickness of the freshwater lens below a creek ridge were not investigated quantitatively to a large extent, some hydrogeological aspects are qualitatively discussed here.

It is expected that low-permeable layers, in particular their spatial coherence and permeability, play an important role in the thickness of the freshwater lens and, hence, in the effect of the CARD system on the increase of the freshwater lens. The field observations at ML 2 showed that even thin layers can already significantly influence the increase of the freshwater lens. For applying the CARD system elsewhere, it is important to realize that in geological models these thin

layers might not always be present, as was the case in this study. CPTs offer a relatively cheap and effective technique with very high vertical resolution, for detecting (thin) low permeable layers.

In addition to the low permeable layers, the drainage resistance is expected to have a large influence on the effect of the CARD system on the thickness of the freshwater lens. The drainage resistance is the hydraulic resistance that the natural and artificial recharge experiences upon flowing towards drainage entities (i.e., ditches and drain tiles). The lower the drainage resistance, the less water (and energy) is needed to maintain an elevated groundwater table. A low drainage resistance is amongst others favored by a low permeability of the sandy tidal creek deposits below the creek ridge, a low permeability of the bed sediment of ditches and a low permeability of the semi-confining layer. A low permeability of the creek sediments has a positive effect on the amount of water that is needed to maintain an elevated groundwater table, but has a negative effect on the speed of the freshening. The speed and extent of the freshening furthermore depends on how long and how much the groundwater table can be increased during the year, as was indicated by the results of the scenario simulations. Furthermore, for applying the CARD system elsewhere it is important that the unsaturated zone is thick enough to accommodate the increase of the groundwater table.

Evidently, from thicker freshwater lenses more fresh groundwater can be extracted. How much extra water could be extracted (i.e., the recovery efficiency) or what the most optimal extraction approach is, was not investigated. This is left for further study. As the area of the artificial recharge is large and the artificial recharge is applied in a relatively shallow aquifers, it is advised to use horizontal wells for the extraction. Compared to vertical wells, horizontal wells induce less the drawdown per volume of abstracted groundwater (Yeh and Chang, 2013), which in turn reduces saltwater upconing (Dagan and Bear, 1968).

### 3.5 Conclusions

Freshwater lenses below creek ridges are important for irrigation in the southwestern part of the Netherlands. Their sustainable exploitation is jeopardized by future stresses such as increasing water demand, sea level rise and climate change. To sustain and increase freshwater supply in the area measures are needed.

This chapter considered a Controlled Artificial Recharge and Drainage (CARD) system for increasing a freshwater lens below a creek ridge, for increasing freshwater supply. The CARD system aims at increasing the groundwater table below the creek ridge to increase the freshwater lens, and is therefore based on the Badon Ghijben - Herzberg principle. The groundwater table is increased by artificial recharge of fresh surface water during winter in combination with high drainage levels.

The CARD system was tested on a creek ridge in the southwestern part of the Netherlands, using field measurements and numerical simulations. The numerical simulations reasonably reproduced the field measurements. Extensive model cali-

bration and sensitivity analyses were not conducted in view of the long simulation times of the numerical models. The scenario simulation results indicated that over a period of 10 years, the 10-15 m thick freshwater lens increased up to 10 m in case the groundwater table in winter at the higher parts of the creek ridge was increased by up to 0.5 m using the CARD system. A 0.1 m lower groundwater table led to a lower increase of the volume of the fresh water water lens, but a higher storage efficiency of the CARD system (the volume of water infiltrated relative to the increased volume of the freshwater lens). A 0.1 m higher groundwater table had the opposite effect. All scenarios indicated the potential of raising the groundwater table using the CARD system in increasing the freshwater lens.

It is expected that the most important factors that influence the effect of the CARD system on the increase of the freshwater lens are low permeable layers, the drainage resistance, the water availability for artificial recharge and the thickness of the unsaturated zone to accommodate the increase of the groundwater table.

## 3.6 Appendix

This Appendix provides additional information about 1) the Controlled Artificial Recharge and Drainage (CARD) system, 2) the numerical simulation of drainage and infiltration by drain tiles and ditches using the DRAIN and RIVER packages, 3) the simulation of the CARD system in the scenario simulations, 4) the results of the comparison between the CPTs and the initialization simulation with the optimized groundwater recharge, and 5) the scenario simulations B and C.

### 3.6.1 Additional information of the CARD system

In Figure 3.15 an overview and impression of the CARD system is shown. Freshwater is collected behind a weir (**a**). Excess freshwater discharges into the brackish/saline water ditch (shown in **b** and **d**). The collected freshwater is pumped via a transport pipe over the brackish/saline water ditch (**b**) into the CARD system at the inlet point. The freshwater infiltrates at the high parts of the creek ridge (**c**). At the low parts, the water level is controlled in a collector well (**c** and **e**). In the separating ditch (**c**) a dam was placed to prevent drainage of the fresh groundwater.

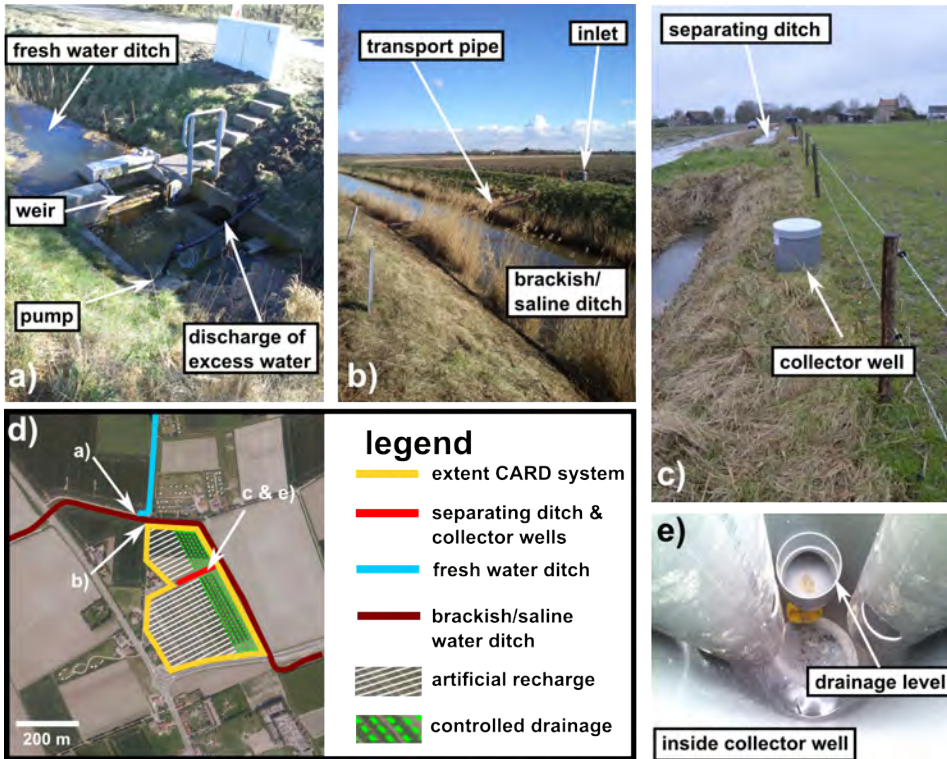


Figure 3.15: Impression and overview of the CARD system.

### 3.6.2 Numerical simulation of drainage and infiltration by drain tiles and ditches using the DRAIN and RIVER packages

Drainage by drain tiles was simulated using the DRAIN package, ditches were simulated using the RIVER package of SEAWAT (Langevin et al., 2007). The conductance values of the RIVER and DRAIN cells were determined using the method of De Lange (1999). This method for determining the conductance requires the determination of 7 parameters related to the properties of the ditch or drain tiles and the hydrogeological unit that supports the groundwater - surface water interaction. The 7 parameters are (using the term 'surface water' to indicate the drain tiles or ditches):

1. The entry resistance of the surface water  $c_0$  [T].
2. The resistance of the layer below the hydrogeological unit  $c_1$  [T].
3. The width of the surface water  $B$  [L].
4. The effective distance between the surface waters  $L$  [L].
5. The thickness of the hydrogeological unit  $H$  [L].
6. The representative horizontal hydraulic conductivity of the hydrogeological unit  $K_{h-eff}$  [L T<sup>-1</sup>].
7. The representative vertical hydraulic conductivity of the hydrogeological unit  $K_{v-eff}$  [L T<sup>-1</sup>].

The entry resistance of the drain tiles is equal to the thickness of the drain envelope divided by the hydraulic conductivity of the drain envelope. The entry resistance of the ditches is equal to the thickness of the ditch bed divided by the vertical hydraulic conductivity of the ditch bed. Unfortunately, detailed information about the entry resistance of the drain tiles and ditches was not available. As there was not an indication of important clogging layers around the drain tiles or at the ditch bed, the entry resistance was assigned a relatively low value of 1 d. From the geological model, a low-permeable layer below the hydrogeological unit could not be distinguished. Therefore,  $c_1$  was given a low value of 0.1 d.

Three types of ditches were simulated in the model (Figure 3.16). The primary, secondary and tertiary ditches have an average width  $B$  of 8.0, 1.2, and 1.0 m, respectively. The width of the drain tiles is on average 0.1 m. The effective distance between the ditches was based on the length of the surface water in the cell and the cell area (De Lange, 1999). For the drain tiles  $L$  was given a value of 7 m, based on local knowledge of the farmers.

$H$  was taken as the distance between surface elevation and the lowermost 'non-sand' cell in the upper 10 meters of the geological model GEOTOP (Stafleu

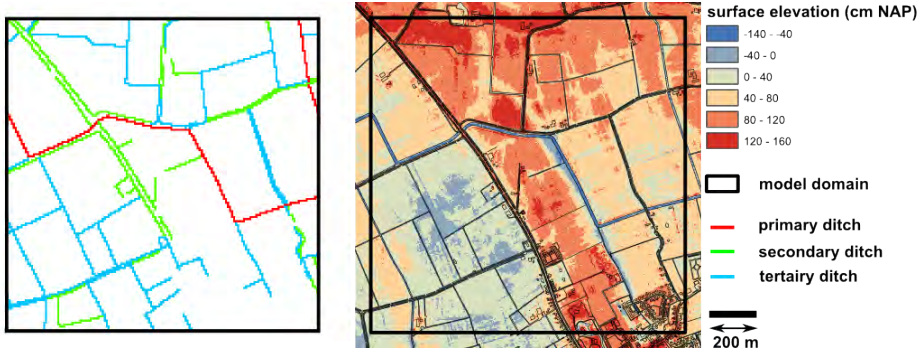


Figure 3.16: Overview of the locations of the ditches (left) and the model domain in plan view (right), including a surface elevation map.

et al., 2011). The effective horizontal and vertical hydraulic conductivities of the hydrogeological unit ( $K_{h-eff}$  and  $K_{v-eff}$ , respectively) were determined using:

$$K_{h-eff} = \frac{\sum(m_i K_{h-i})}{\sum m_i} \quad K_{v-eff} = \frac{\sum m_i}{\sum(\frac{m_i}{K_{v-i}})} \quad (3.2)$$

$K_{h-i}$  is the horizontal hydraulic conductivity of an individual cell with thickness  $m_i$ .  $K_{v-i}$  is the vertical hydraulic conductivity of an individual cell with thickness  $m_i$ .

The ditches have a controlled winter and summer level. In Figure 3.17 the water level of the ditches in winter relative to NAP is shown. In summer, the water level in the primary ditches is 0.2 m higher. The secondary ditches and tertiary ditches fall dry during summer.

### 3.6.3 Simulation of the CARD system in the scenario simulations

In the scenario simulations the influence of the CARD system on the thickness of the freshwater lens was investigated. The RIVER package was used to represent infiltration and drainage in the CARD system. The 'stage' of each cell where the RIVER package was applied was based on the weekly average hydraulic heads that were measured at measurement locations (ML) 1, 2, and 4. Due to the surface elevation and the necessary drainage, the hydraulic heads during the artificial recharge in winter are higher at MLs 1 and 2 than at ML 4. In Figure 3.18 a plan view of the assigned stages of the CARD system is shown. In area I, the highest stage was assigned, whereas the lowest stage was assigned in area IV. For Scenario A, the variation of the maintained water levels as a function of time is shown in Figure 3.19, for the 4 different areas in the CARD system.

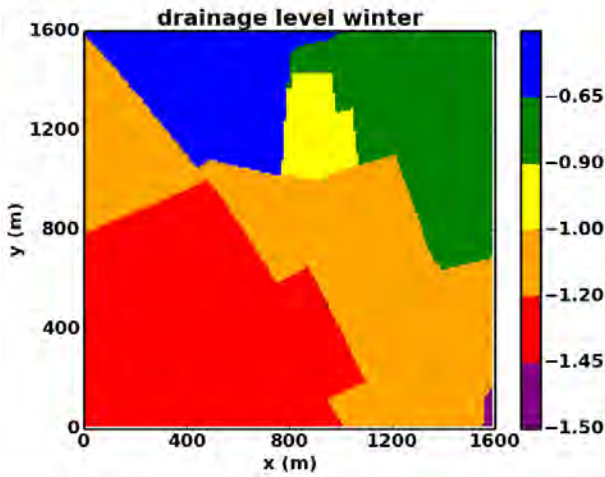


Figure 3.17: Overview of the controlled surface water levels in the study area during the winter half year. The elevation is shown relative to NAP.

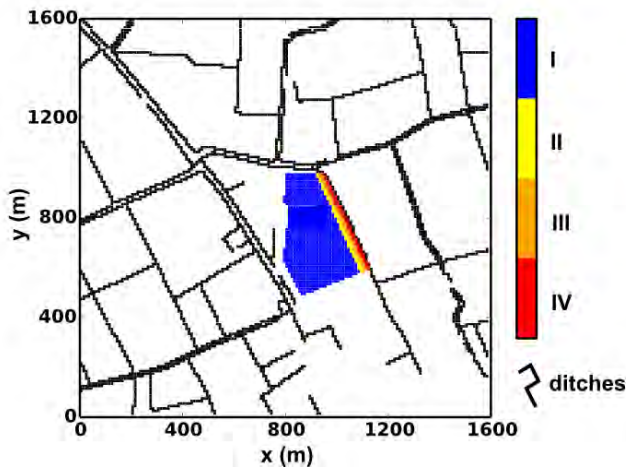


Figure 3.18: Plan view of the assigned stages of the CARD system. In area I, the highest stage is assigned, whereas the lowest stage is assigned in area IV. The assigned stages for each area per stress period are shown in Figure 3.19.

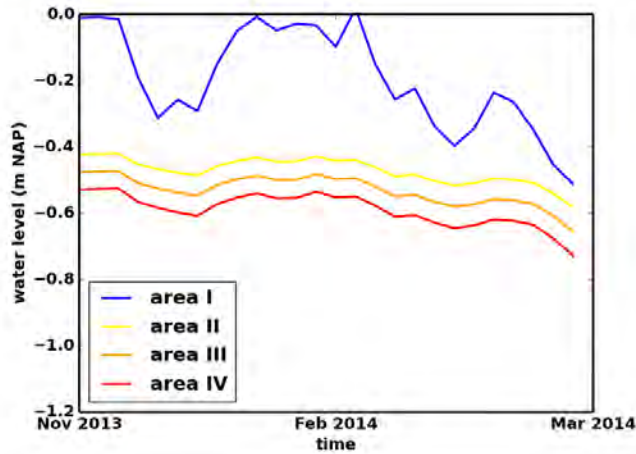


Figure 3.19: The variation of the assigned water levels in scenario A as a function of time for the 4 different areas in the CARD system.

### 3.6.4 Additional results of the comparison between the CPTs and the initialization simulation with the optimized ground-water recharge

The CPTs and the results of the initialization simulation with the optimized ground-water recharge were compared at MLs 1-5 with respect to  $D_{mix}$ . The reason for analyzing  $D_{mix}$  was because information about the formation factor that is needed to calculate  $EC_{w20}$  (the electrical conductivity of the water, referenced to a temperature of 20°C) from the measured  $EC_{bulk}$  (the electrical conductivity of the sediment and pore water) was not available.

The CPTs and the results of the initialization simulation can be further compared by investigating the relative change of simulated  $EC_{w20}$  and measured  $EC_{bulk}$  with depth. In Figure 3.20 the simulated  $EC_{w20}$  and measured  $EC_{bulk}$  as a function of depth (NAP) are shown. The horizontal scales have been chosen such that the maximum value of  $EC_{w20}$  ( $40.6 \text{ mS cm}^{-1}$ ) corresponds with the maximum value of  $EC_{bulk}$  in absence of clay ( $8 \text{ mS cm}^{-1}$ ).

The best match between the simulated  $EC_{w20}$  and  $EC_{bulk}$  was obtained at ML 5. This can be attributed to the absence of low permeable sediment at depth in both the model and the CPT, as can be seen in Figure 3.21, where the friction ratio ( $R_f$ ) deduced from the CPTs is plotted together with the vertical hydraulic conductivity ( $K_v$ ) in the numerical model.

At the other MLs,  $R_f$  values  $> 2$  indicate sections where the sediment has a relative low permeability (i.e., clay or peat). At MLs 1, 2, and 3 these layers are not present in the numerical model. Therefore, the  $EC_{w20}$  is simulated at a larger depth compared to  $EC_{bulk}$ . At ML 4, low permeable sediment is indicated by the

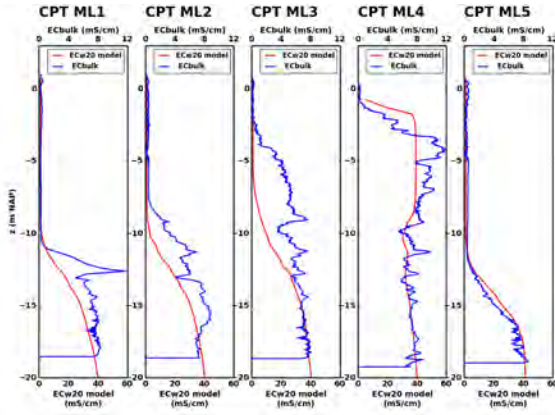


Figure 3.20: Measured  $EC_{bulk}$  (CPTs) and simulated  $EC_{w20}$  as a function of depth (m NAP) at the five MLs.

CPT and also present in the numerical model. Therefore, at this location the match between the CPT and the numerical models is better than at ML 1, 2, and 3.

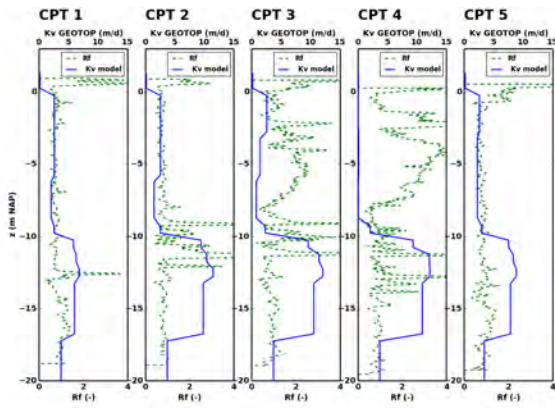


Figure 3.21: The friction ratio ( $R_f$ ), measured by the CPTs and the vertical hydraulic conductivity distribution in the numerical model ( $K_v$  GEOTOP), both as a function of depth (m NAP) for the five MLs.

### 3.6.5 Results of scenarios B and C

In Figures 3.22 and 3.23 the results of scenarios B and C are shown, respectively, analogous to Figure 3.13.

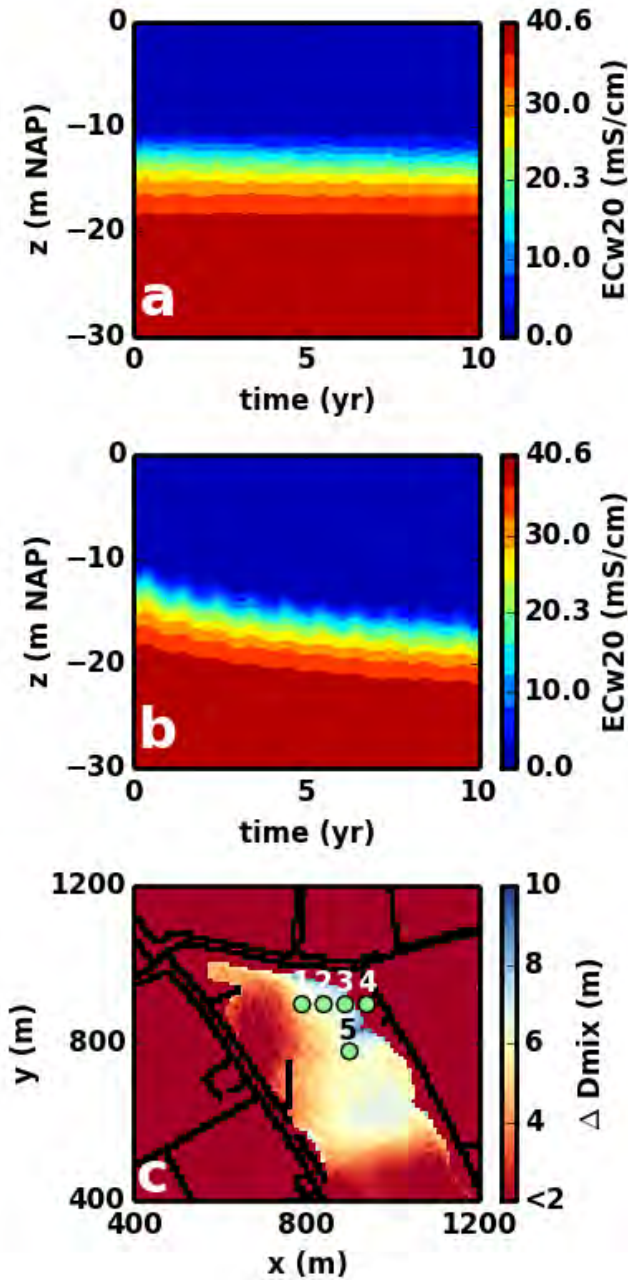


Figure 3.22: **a** Simulated  $EC_{w20}$  contours as a function of depth and time at ML 1 in the reference simulation. **b** Simulated  $EC_{w20}$  contours as a function of depth and time at ML 1 in scenario B. **c** difference in  $D_{mix}$  ( $\Delta D_{mix}$ ) between the reference simulation and scenario B, after 10 years of simulation time. The black solid lines indicate ditches. The green dots and the white numbers indicate the MLs.

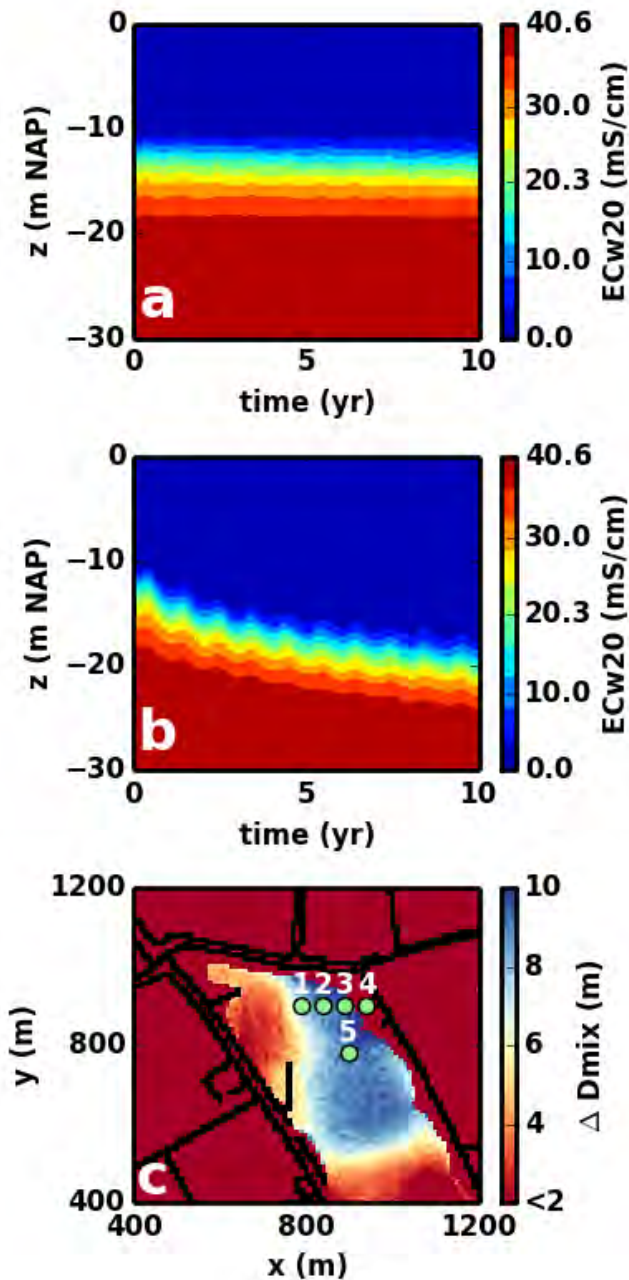


Figure 3.23: **a** Simulated  $EC_{w20}$  contours as a function of depth and time at ML 1 in the reference simulation. **b** Simulated  $EC_{w20}$  contours as a function of depth and time at ML 1 in scenario C. **c** difference in  $D_{mix}$  ( $\Delta D_{mix}$ ) between the reference simulation and scenario B, after 10 years of simulation time. The black solid lines indicate ditches. The green dots and the white numbers indicate the MLs.

## Chapter 4

# Saltwater upconing due to cyclic pumping by finite horizontal wells in freshwater lenses

This chapter is based on: *Pauw, P.S., Leijnse, A., Van der Zee, S.E.A.T.M. & Oude Essink, G.H.P. Saltwater upconing due to cyclic pumping by finite horizontal wells in freshwater lenses. Under review in Groundwater, 2015.*

### 4.1 Introduction

Freshwater lenses are important for freshwater supply in coastal areas (Custodio and Bruggeman, 1987; Bear et al., 1999; Werner et al., 2013). Pumping from freshwater lenses generally leads to saltwater upconing, i.e., a local rise of saline groundwater below the well (Dagan and Bear, 1968; Werner et al., 2009). As long as saltwater upconing remains limited, freshwater lenses can be sustainably exploited. In case of excessive saltwater upconing, however, there is a high risk of an undesired salinity in the well. Excessive saltwater upconing has led to closure of wells in many coastal areas (Stuyfzand, 1996; Custodio, 2009). Evidently, quantitative investigations of saltwater upconing are important for preventing this type of overexploitation.

In quantitative investigations on saltwater upconing, 'interface' and 'miscible' approaches can be distinguished (Reilly and Goodman, 1985; Werner et al., 2009). In the interface approach, fresh and saline groundwater are considered as immiscible fluids, separated by an interface. The fluids have a different density and, in some cases, dynamic viscosity. In the miscible approach, fresh and saline ground-

water mix by hydrodynamic dispersion. In view of its mathematical complexity, a miscible approach usually requires a numerical model (Reilly and Goodman, 1985; Zheng and Bennett, 2002). Although numerical models based on the miscible approach have been used in many previous saltwater upconing studies (Zhou et al., 2005; Jakovovic et al., 2011), their major disadvantage is the high computational demand in case of a large number of grid cells. The computational demand can be reduced by using a lower grid resolution, but this can lead to an underestimation of saltwater upconing, as the cone is smeared out over a large cell area (De Marsily, 1995).

Analytical solutions based on the interface approach offer an attractive alternative to numerical models based on the miscible approach with respect to computation time and insight. Motz (1992) and Bower et al. (1999) presented analytical solutions to determine the critical, steady state pumping rate in case of a partially penetrating well in an aquifer overlain by a leaky confining layer. Below the critical pumping rate the well pumps only fresh groundwater, whereas above the critical pumping rate the interface below the well is not stable and will rise abruptly to the well screen. A steady-state analytical solution to determine the critical pumping rate was also presented by Garabedian (2013), for the case of a partially penetrating well in an aquifer with no-flow conditions at the top and bottom and a constant head boundary condition at a defined radial distance from the well.

In addition to these steady-state analytical solutions, Dagan and Bear (1968) presented transient analytical solutions for the rise of the interface due to pumping, for a point well (i.e., axi-symmetric flow) and for an infinite horizontal well. Zhang et al. (1997) also presented an analytical solution for the case of a point well. Schmorak and Mercado (1969) used the analytical solutions of Dagan and Bear (1968) to determine the critical pumping rate of a point well in case of infinitely thick and confined freshwater and saltwater zones, and to calculate the downward movement of the interface after the pumping stops.

Numerical models based on the interface approach have also been used in previous studies on saltwater upconing (Wirojanagud and Charbeneau, 1983; Reilly et al., 1987b). In case the Dupuit assumption is adopted, such models are computationally efficient (Bakker, 2003). However, in the study that is presented in this chapter, the Dupuit assumption could not be adopted. Instead, as a computationally efficient alternative for numerical models based on the miscible approach, analytical solutions based on the interface approach are considered. The analytical solutions are used to calculate saltwater upconing below horizontal wells in freshwater lenses. The considered pumping regime is representative for the extraction of fresh groundwater for irrigation. In coastal areas, horizontal wells are often preferred over vertical wells, as they induce less saltwater upconing per volume extracted groundwater (Yeh and Chang, 2013).

The objective of this chapter is to present new insights into the accuracy of analytical solutions for the calculation of saltwater upconing below finite horizontal wells. Three aspects are considered, i.e., 1) cyclic pumping, 2) dispersion, and 3) horizontal wells with a finite length in a finite domain. The first aspect was

investigated, as few previous studies have considered saltwater upconing due to cyclic pumping, despite that cyclic pumping is common when water is extracted for irrigation purposes. The second aspect is important because dispersion adversely affects the safe yield (i.e., maintaining a low salinity in the well) but is disregarded in the analytical interface solutions. The third aspect was investigated because the analytical interface solutions of Dagan and Bear (1968) that were used in this chapter were derived for an infinite domain, whereas in reality freshwater lenses are finite. The three accuracy aspects of the analytical solutions were investigated by comparing the analytical solutions with numerical simulations based on the miscible approach, for a wide range of hydrogeological parameters and pumping regimes.

## 4.2 Material and methods

### 4.2.1 Two-dimensional (2D) and three-dimensional (3D) conceptual models

Numerical simulations and analytical calculations were applied to a 2D conceptual model to investigate the accuracy of the analytical calculations with respect to cyclic pumping and dispersion, in view of the computational effort of the numerical simulations. In the 2D conceptual model the horizontal well has an infinite length. In reality, however, horizontal wells as well as freshwater lenses have a finite length. Therefore, a 3D conceptual model was used for investigating the accuracy the analytical calculations with respect to a finite horizontal well in a finite domain. SEAWAT (Langevin et al., 2007) was used for all the numerical simulations.

### 4.2.2 Cyclic pumping (2D conceptual model)

The 2D conceptual model that was used to investigate cyclic pumping is shown in Figure 4.1. The extent of the model domain is infinite in the horizontal  $x$  [L] direction, with the origin of the  $x$  axis ( $x = 0$ ) located at the well. In view of vertical symmetry at  $x = 0$ , only half of the model domain was considered. In the horizontal direction perpendicular to the  $x$ -axis, the 2D conceptual model represents a horizontal well with an infinite length. The thickness of the domain in the vertical  $z$  [L] direction  $D$  [L] is finite. The  $z$  coordinate is 0 at the top and is positive upwards. Groundwater with a density  $\rho_f$  [ $\text{M L}^{-3}$ ] of  $1000 \text{ kg m}^{-3}$ , which is referred to in this chapter as fresh groundwater, is situated on top of saline groundwater with a higher density  $\rho_s$  [ $\text{M L}^{-3}$ ]. The freshwater density corresponds with a salt concentration  $C$  [ $\text{M L}^{-3}$ ] of  $0 \text{ kg m}^{-3}$ . In the saline groundwater with density  $\rho_s$ , the concentration is equal to  $C_s$  [ $\text{M L}^{-3}$ ]. Common assumptions on the properties of fresh and saline groundwater were adopted (Langevin et al., 2007); the density of the groundwater varies linearly with concentration and the fresh and the saline groundwater have the same dynamic viscosity  $\mu$  [ $\text{M L}^{-1} \text{ T}^{-2}$ ]. The aquifer has a

homogeneous porosity ( $n$ ) [-] and horizontal ( $\kappa_h$ ) and vertical permeability ( $\kappa_v$ ) (both [ $L^2$ ]). The horizontal ( $K_x$ ) and vertical ( $K_z$ ) hydraulic conductivities [ $L T^{-1}$ ] based on fresh groundwater are defined as:

$$K_x = \frac{\kappa_x \rho_f g}{\mu} \quad (4.1)$$

$$K_z = \frac{\kappa_z \rho_f g}{\mu} \quad (4.2)$$

in which  $g$  is the gravitational acceleration [ $L T^{-2}$ ]. The concept of elastic storage (storage coefficient  $S_s$  [ $L^{-1}$ ]) was used to account for the compressibility of the groundwater and porous medium, and the concept of phreatic storage (specific yield  $S_y$  [-]) was used to account for drainage at the water table (Domenico and Schwartz, 1990).

Initially, at time  $t$  [T] = 0, the fresh and the saline groundwater are at rest, and the hydraulic head  $h$  [L] at the top of the aquifer is 0 m. The depth of the interface between fresh and saline groundwater  $\zeta$  [L] is where  $C = 0.5C_s$ . The initial thickness of the freshwater zone  $a$  [L] is defined as the distance between the initial interface depth and the top of the aquifer. The initial thickness of the saline groundwater zone  $b$  [L] is defined as the distance between the initial interface depth and the bottom of the aquifer. The well, which has a negligible screen length, is located at a vertical distance  $d$  [L] from the initial interface depth.

A mixing zone is present around the interface in which, in the initial situation, the concentration in the vertical is normally distributed (Gaussian). The thickness of the mixing zone  $M$  [L] is defined as twice the distance between the interface and the depth at which the concentration equals  $0.024C_s$ , i.e., two standard deviations from  $0.5C_s$ . Interface upconing is defined as the distance between the initial interface depth and the interface depth after a certain amount of time due to pumping. Saltwater upconing is more generally defined than interface upconing, i.e., saltwater upconing is the rise of the saline groundwater relative to its initial depth, regardless of its salinity (i.e., any concentration higher than freshwater).

A cyclic pumping regime was considered, which takes place during a period  $T_p$  [T] of 180 days.  $T_p$  represents a dry half year when irrigation is needed, and consists of a number of cycles ( $n_{cyc}$ ), in which fresh groundwater is pumped during a period  $T_{on}$  [T], followed by a period of no pumping  $T_{off}$  [T]:

$$n_{cyc} = \frac{T_p}{T_{on} + T_{off}} \quad (4.3)$$

During  $T_{on}$  fresh groundwater is pumped with a rate  $Q_d$  [ $L^2 T^{-1}$ ] (the pumping rate of the well per unit length of the well).

The following section explains the numerical and analytical approaches for the 2D conceptual model shown in Figure 4.1.

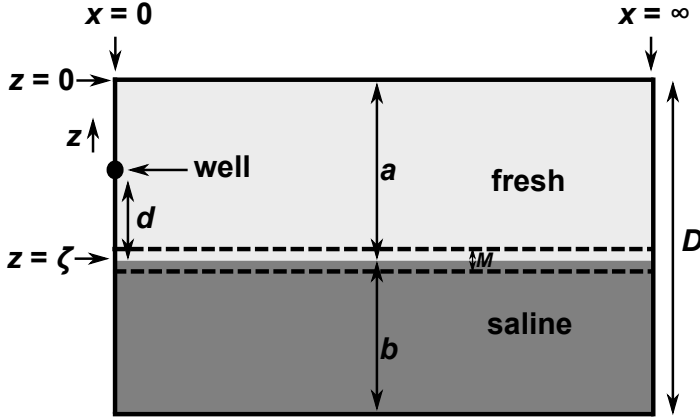


Figure 4.1: 2D cross-sectional conceptual model that was used in the analytical calculations and numerical simulations. The initial conditions (i.e., prior to pumping) are shown.

### Numerical simulations and analytical calculations

A 2D numerical model was constructed based on the conceptual model shown in Figure 4.1. A constant hydraulic head and constant concentration boundary condition was used at 200 meters from the well ( $x = 200$  m). Testing showed that, for the parameter variations that were considered, this was far enough to approximate an infinite domain. The hydraulic head at this boundary is 0 m at the top and hydrostatic downwards. The concentration at this boundary as well as the initial concentration was specified according to the initial thickness of the freshwater and saltwater zones ( $a$  and  $b$ ) and the thickness of the mixing zone  $M$ .

The groundwater flow equation was solved using the PCG package. The advection part of solute transport equation was solved using the MOC solver, with a minimum number of 27 particles and a relatively low Courant number of 0.1. The dispersion part of the solute transport equation was solved using the GCG package. A regular grid with a column width of 0.1 m and a layer thickness of 0.05 m was used. Testing showed that a finer grid did not significantly change the simulation results.

An analytical interface solution was applied to the conceptual model shown in Figure 4.1, based on equation 43 presented by Dagan and Bear (1968) and on the transformation procedures for anisotropy presented by Bear and Dagan (1965):

$$\zeta_{an} = \frac{Q_d}{\delta\pi\sqrt{K_x K_z}} \int_0^\infty \frac{1}{\lambda} \frac{\cosh[\lambda(a-d)]}{\sinh(\lambda a)} \left[ 1 - \exp\left(\frac{-\lambda t}{\frac{n}{\delta K_z} \cotgh(a\lambda) + \frac{n}{\delta K_z} \cotgh(b\lambda)}\right) \right] \cos(\lambda x \sqrt{\frac{K_z}{K_x}}) d\lambda - a, \quad (4.4)$$

where  $\zeta_{an}$  [L] is the interface depth,  $\delta$  is defined as:

$$\delta = \frac{\rho_s - \rho_f}{\rho_f} \quad (4.5)$$

and  $\lambda$  is the variable of integration. In Equation 4.4 it is assumed that the aquifer and the groundwater are both incompressible, in contrast to the conceptual model shown in Figure 4.1. Therefore, the influence of elastic and phreatic storage was investigated using numerical simulations. Another important limitation of Equation 4.4 is that it is only valid up to a certain degree of interface upconing. This is related to the method of small perturbations that Dagan and Bear (1968) used for the derivation. Dagan and Bear (1968) recommended using Equation 4.4 for cases where the interface upconing is less than  $1/3 d$ , based on comparison with laboratory (Hele-Shaw) experiments. The dimensionless interface upconing  $d\zeta$  is defined as the analytically calculated interface upconing divided by  $d$ .

Cyclic pumping using Equation 4.4 was simulated using the superposition principle. This procedure is illustrated using Figure 4.2, with  $T_{on} = 5$  days,  $T_{off} = 10$  days and  $n_{cyc} = 3$ . The three blue lines in Figure 4.2 each indicate interface upconing due to pumping with extraction rate  $Q_d$ . They start at  $t = i(T_{on} + T_{off})$ , with  $i = (0,1,2)$ . The red lines indicate the downward movement of the interface due to well injection with rate  $-Q_d$ . These lines start at  $t = i(T_{on} + T_{off}) + T_{on}$ , with  $i = (0,1,2)$ .  $\zeta_{an}$  is obtained by summing the contribution of all lines throughout the total pumping period  $T_p$  (black line in Figure 4.2).

### Parameter variations and accuracy definitions

The analytical calculations were compared with numerical simulations for various parameter combinations. The parameters  $T_p$  (180 d),  $n$  (0.3),  $a$  (12 m),  $b$  (18 m),  $d$  (7 m), and  $\rho_f$  (1000 kg m<sup>-3</sup>) were kept constant, as they were considered irrelevant or superfluous for investigating the accuracy of the analytical calculations. The molecular diffusion coefficient ( $D_m$ ) in the numerical simulations was  $8.64 \cdot 10^{-5}$  m<sup>2</sup>d<sup>-1</sup>. The influence of the parameters  $Q_{tot}$  (the total amount of extracted fresh groundwater during  $T_p$  [L<sup>3</sup>]),  $n_{cyc}$ ,  $Q_d$ ,  $K_x$ ,  $K_z$ ,  $C_s$  and  $\alpha_L$  (the longitudinal dispersivity, [L]) was investigated relative to a set of reference parameters (Table 4.1 and the Appendix of this chapter). Note that  $T_p$ ,  $n_{cyc}$ ,  $T_{on}$ ,  $T_{off}$ ,  $Q_d$ , and  $Q_{tot}$  are related by Equation 4.3 and by:

$$Q_{tot} = Q_d n_{cyc} T_{on} \quad (4.6)$$

In addition to these parameters, the influence of the specific storage ( $S_s$ ) and specific yield ( $S_y$ ) parameters was also investigated using numerical simulations, as in Equation 4.4 it is assumed that the aquifer and groundwater are both incompressible.

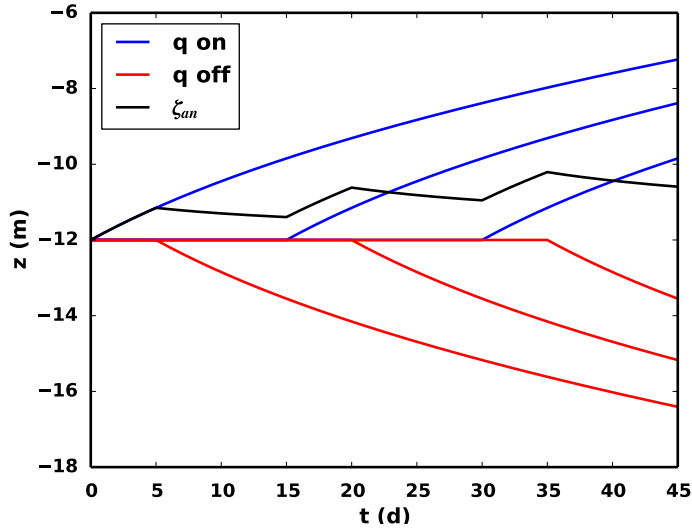


Figure 4.2: Illustration of calculating the upward and downward movement of the interface  $\zeta_{an}$  due to well extraction (q on) and well shutdown (q off), using the superposition principle and Equation 4.4.

As a measure of the accuracy of the analytical calculations with respect to cyclic pumping, the error in the interface depth ( $\epsilon_\zeta$  [L]) was calculated using:

$$\epsilon_\zeta = \zeta_{an}(x = 0) - \zeta_{num}(x = 0), \quad (4.7)$$

where  $\zeta_{num}$  [L] is the interface depth in the numerical simulation.

### 4.2.3 Dispersion (2D conceptual model)

#### Numerical simulations and analytical calculations

The numerical model and Equation 4.4 that were used to investigate the accuracy of the analytical calculations with respect to cyclic pumping were also used to investigate the analytical calculation of mixing by dispersion. As Equation 4.4 is based on the interface approach, the following equation was used to account for dispersion:

$$C = C_s 0.5 \operatorname{erfc} \left( \frac{s_\zeta}{2\sqrt{\alpha_L(\eta + |s|)}} \right), \quad (4.8)$$

Table 4.1: Variation of parameters for investigating the accuracy of the analytical calculations with respect to cyclic pumping and dispersion. As certain parameters are related, a complete overview of all parameter combinations is given in the Appendix of this chapter. Values between parentheses denote the reference values. The reference values for  $T_{on}$  and  $T_{off}$  are both 1 d. The storage parameters were only varied in the numerical simulations.

| parameter      | variations                            | units               |
|----------------|---------------------------------------|---------------------|
| $Q_{tot}$ (18) | 36, 54, 72, 80, 98                    | $m^3 m^{-1}$        |
| $n_{cyc}$ (90) | 180, 45, 30, 10, 1                    | -                   |
| $Q_d$ (0.2)    | 20.0, 4.0, 2.0, 0.4, 0.16, 0.13, 0.11 | $m^3 m^{-1} d^{-1}$ |
| $K_x$ (10)     | 1, 5, 50, 100                         | $m d^{-1}$          |
| $K_x/K_z$ (1)  | 2.0, 5.0                              | -                   |
| $C_s$ (35)     | 17.5, 8.25                            | $kg m^{-3}$         |
| $\alpha_L$     | 0.01, 1.0                             | m                   |
| $Ss$ (1E-5)    | 0                                     | $m^{-1}$            |
| $Sy$ (0.15)    | 0                                     | -                   |
| $M$ (0)        | 1.4, 2.8                              | m                   |

where  $C$  [ $M L^{-3}$ ] is the concentration of the groundwater at a vertical distance  $s_\zeta$  from  $\zeta_{an}$ , and  $|s|$  [L] is the total absolute traveled distance of  $\zeta_{an}$  throughout  $T_p$ , which can be derived from the analytical calculations.  $\eta$  [L] is equal to:

$$\eta = \frac{\left( \frac{0.5M}{2\text{erfc}^{-1}(0.048)} \right)^2}{\alpha_L} \quad (4.9)$$

$\eta$  was derived by solving  $|s|$  in Equation 4.8 using  $C/C_s = 0.024$  (see the definition of the width of the mixing zone  $M$ ) and using the corresponding value of  $s_\zeta$ . Equations 4.8 and 4.9 are based on Schmorak and Mercado (1969). In applying these equations it is assumed that below the well the saltwater upconing is governed by vertical flow (advection) and longitudinal dispersion, so mixing due to diffusion and transversal dispersion is neglected. In addition, it is assumed that the pore water velocity in the vertical does not vary (i.e., is equal to the velocity of the interface), and that the vertical concentration distribution around  $\zeta$  is normally distributed. The appropriateness of these assumptions for the parameter combinations that are considered here will be addressed later in this chapter.

### Parameter variations and accuracy definitions

Using the parameter combinations of the 2D conceptual model (Table 4.1 and Figure 4.1) the accuracy of the analytical calculations with respect to dispersion was analysed. Similar as in the investigations on cyclic pumping, accuracy measures were defined. Two concentration values were investigated:

$$C_{1\sigma} = 0.16C_s \quad C_{2\sigma} = 0.024C_s \quad (4.10)$$

$C_{1\sigma}$  and  $C_{2\sigma}$  represent the concentrations at one standard deviation and two standard deviations from the mean concentration (assuming that the concentration is normally distributed, as in the initial situation), respectively. The reference value of  $C_s$  is equal to  $35 \text{ kg m}^{-3}$  and represents the total dissolved solids in ocean water.  $C_{2\sigma}$  is then equal to  $0.84 \text{ kg m}^{-3}$ , which is representative for the drinking water standard (WHO, 2011).

$C_{1\sigma-an}$  and  $C_{1\sigma-num}$  are defined as the concentration  $C_{1\sigma}$  in analytical calculations and numerical simulations, respectively. In a similar way,  $C_{2\sigma-an}$  and  $C_{2\sigma-num}$  are defined. The accuracy definitions  $\epsilon_{1\sigma}$  [L] and  $\epsilon_{2\sigma}$  [L] are defined as:

$$\epsilon_{1\sigma} = z(C = C_{1\sigma-an}, x = 0) - z(C = C_{1\sigma-num}, x = 0) \quad (4.11)$$

$$\epsilon_{2\sigma} = z(C = C_{2\sigma-an}, x = 0) - z(C = C_{2\sigma-num}, x = 0) \quad (4.12)$$

$z(C = C_{1\sigma-an}, x = 0)$  and  $z(C = C_{1\sigma-num}, x = 0)$ [L] are the depths at which the concentration below the well is equal to  $C_{1\sigma}$ , in the numerical simulations and analytical calculations, respectively. In a similar way,  $z(C = C_{2\sigma-an}, x = 0)$  and  $z(C = C_{2\sigma-num}, x = 0)$ [L] are equal to the depths at which the concentration below the well is equal to  $C_{2\sigma}$ . Note that  $z(C = C_{1\sigma-an})$  and  $z(C = C_{2\sigma-an}, x = 0)$  were computed using Equations 4.8 and 4.9.

#### 4.2.4 Horizontal wells with a finite length in a finite domain (3D conceptual model)

In the 2D conceptual model that was used to analyse cyclic pumping and dispersion, the horizontal well was assumed to have an infinite length. In reality, however, both horizontal wells and freshwater lenses have a finite length. Therefore, a 3D conceptual model was used to investigate the accuracy of analytical calculations with respect to the finite length of the horizontal well and the domain. In Figure 4.3, a quarter of this model is shown, as the model is symmetrical along the  $x$  and  $y$  axes.

Prior to pumping, a freshwater lens is present in a finite domain with horizontal length  $L_x$  [L] and  $L_y$  [L] and thickness  $D$  during a period  $T_{init}$  [T]. A freshwater lens is present, which terminates at the boundaries  $x = 0.5L_x$  and  $y = 0.5L_y$ . The outflow level at the boundaries is equal to 0 m. Inflow can take place along the total vertical depth at the boundaries with a density (and corresponding salinity)  $\rho_s$ . The vertical pressure distribution at the boundaries is hydrostatic. Similar as in the 2D conceptual model,  $z$  is positive upwards.

The thickness of the freshwater lens varies due to groundwater recharge at the top of the total model area during a period  $T_{rch}$  [T], followed by a period  $T_{dry}$  [T], in which there is no groundwater recharge.  $T_{rch}$  has a length of 180 days, in which the recharge rate ( $N$  [L T<sup>-1</sup>]) is constant ( $0.002 \text{ m d}^{-1}$ ). The length of  $T_{dry}$

is also 180 days. The freshwater lens is in dynamic equilibrium, i.e., the thickness of the freshwater lens is constant at the end of successive periods  $T_{rch}$ .

The end of a  $T_{rch}$  period is the initial condition for a period where pumping takes place. Similar as in the 2D conceptual model, cyclic pumping takes place during a period  $T_p$  of 180 days. The well has a finite horizontal length  $L_{well}$  [L]. During  $T_{on}$ , the pumping rate of the well is  $Q$  [L<sup>3</sup> T<sup>-1</sup>]. The well is located in the center of the freshwater lens and oriented in the direction of the  $y$ -axis; the longest axis.

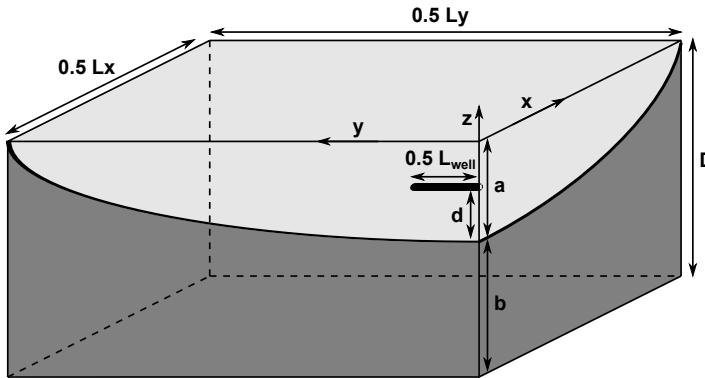


Figure 4.3: Overview of the 3D conceptual model prior to pumping (only a quarter is shown).  $z$  is positive upwards. The light grey area shows the freshwater lens at the end of  $T_{init}$ . Note that the mixing zone between fresh and saline groundwater is not shown.

### Numerical simulations and analytical calculations

A 3D numerical model was constructed based on the conceptual model shown in Figure 4.3. Only the most important aspects of this numerical model are described here, as many aspects are similar to the 2D numerical model. In the 3D numerical model an irregular grid was used in view of computational effort. Near the well, the horizontal cell size is 0.1 m. Away from the well the cell size gradually increases towards the boundaries. Between the well and the initial mixing zone, 0.1 m thick model layers were used. Above and below, the layer thickness gradually increases. Only a quarter of the domain of the full problem was simulated, in view of symmetry along the  $x$  and  $y$  axes. The bottom and the vertical planes at  $x = 0$  and  $y = 0$  are no-flow boundaries. Along the vertical planes at  $x = 0.5L_x$  and  $y = 0.5L_y$  a constant hydraulic (saltwater) head (0 m) and concentration boundary condition with concentration  $C_s$  was applied. The hydraulic head along these vertical sides therefore follows a hydrostatic pressure distribution. These flow and concentration boundary conditions remain constant throughout the simulation.

The initial condition was simulated in the numerical model starting from an

initial saline model domain, and simulating the development of a freshwater lens using subsequent periods  $T_{rch}$  and  $T_{dry}$ . During  $T_{rch}$ , groundwater recharge with a rate  $N = 0.002 \text{ m d}^{-1}$  and with concentration  $C = 0$  was simulated. During  $T_{dry}$  no recharge was simulated. The initial condition period  $T_{init}$  was ended when the total salt mass in the domain over successive  $T_{dry}$  and  $T_{rch}$  periods reached a virtually stable value.

Pumping using the finite horizontal well during  $T_p$  was simulated by superposition of point sinks. The extraction rate for every cell that represented the horizontal well was determined by dividing the total extraction rate of the well by the amount of columns that were used to simulate the well. In this approach, it is assumed that the extraction rate per unit length along the well is constant. In reality, this is not always the case due to pressure losses in the well. Moreover, even when a constant pressure is present along the total length of the well, the flow pattern at the edges of well is different than in the center of the well, which also induces a variable inflow along the well. These two effects will be discussed in somewhat more detail at the end of this chapter.

In the analytical calculations, the initial condition (i.e., the freshwater lens) was not simulated. The input parameters for  $T_p$ , such as the initial thickness of the mixing zone  $M$  and its salinity distribution, were taken from the numerical model. The initial thickness of the freshwater and saltwater zones ( $a$  and  $b$ ) was taken from the numerically simulated salinity distribution at the center of the horizontal well.

The approach for cyclic pumping was similar as in the 2D analytical calculations. The finite horizontal well was simulated by superposition of point sinks along the length of the well. For further details on this analytical procedure, the reader is referred to Reilly et al. (1987a) and Langseth et al. (2004). The following equation was used for each point sink:

$$\zeta_{an} = \frac{Q}{\delta 2\pi \sqrt{K_x K_z}} \int_0^\infty \frac{1}{\lambda} \frac{\cosh[\lambda(a-d)]}{\sinh(\lambda a)} \left[ 1 - \exp \frac{-\lambda t}{\frac{n}{\delta K_z} \cotgh(a\lambda) + \frac{n}{\delta K_z} \cotgh(b\lambda)} \right] J_0 \left( \lambda r \sqrt{\frac{K_z}{K_x}} \right) d\lambda - a, \quad (4.13)$$

$J_0$  is a Bessel function of the first kind and order zero and  $r$  is the horizontal radial distance from the well. This equation is based on equation 69 of Dagan and Bear (1968). They derived this equation in a similar way as Equation 4.4, but then for a cylindrical, axisymmetric infinite domain with a vertical rotation axis at the location of the well. As this analytical solution was also derived using a perturbation approximation, it is subjected to the same accuracy condition as Equation 4.4.

### Parameter variations and accuracy definitions

For the comparison of the 3D numerical simulations with the analytical calculations, saltwater upconing during the period  $T_p$  was analysed. Similar as in the 2D comparisons, reference parameters were chosen (Table 4.2) and some parameters

were varied. However, less parameters were varied due to the computational effort of the numerical simulations. Most of parameters are equal to the reference values in the 2D conceptual model; the exceptions are shown in Table 4.2. The horizontal length of the numerical model is 500 m ( $x$ ) by 1000 m ( $y$ ).

The dimensionless analytically calculated interface upconing ( $d_\zeta$ ) is below 1/3 in case of the reference parameter values. The parameter  $Q_{tot}$  was increased to investigate the salinity of the water in the well in case  $d_\zeta$  is close to 1/3. In addition, the length of the well was increased to investigate the influence of the finite domain in case  $d_\zeta$  is close to 1/3 (Table 4.2).

Table 4.2: Reference parameters and variations in the 3D conceptual model. Note that  $a$  and  $b$  were taken as the numerically simulated maximum thickness of the lens at the end of  $T_{init}$ . Regarding the variation of  $L_{well}$ : With an increase of the length of the well, the total extraction also increases, such that the extraction per unit length of the well remains  $150 \text{ m}^3 \text{ m}^{-1}$ . This value corresponds with  $Q_{tot} = 12000 \text{ m}^3$  and the reference length of the well  $L_{well} = 80 \text{ m}$  (i.e.,  $12000 \text{ m}^3 / 80 \text{ m} = 150 \text{ m}^3 \text{ m}^{-1}$ ).

| parameter        | variations | units                       |
|------------------|------------|-----------------------------|
| <b>reference</b> |            |                             |
| $Q_{tot}$        | 4500       | $\text{m}^3$                |
| $Q$              | 0.5        | $\text{m}^3 \text{ d}^{-1}$ |
| $L_{well}$       | 80         | m                           |
| $a$              | 15.5       | m                           |
| $b$              | 14.5       | m                           |
| $d$              | 10.0       | m                           |
| <b>reference</b> |            |                             |
| $Q_{tot}$        | 12000      | $\text{m}^3$                |
| $L_{well}$       | 320, 640   | m                           |

## 4.3 Results

The results of the 2D numerical simulations with the reference parameters are first described, for understanding of the groundwater flow patterns and mixing processes. Subsequently, the results of the parameter variations are used to assess the differences between the analytical calculations and numerical simulations with respect to cyclic pumping and dispersion. Finally, the results of the 3D conceptual model are discussed in view of the horizontal well with a finite length in a finite domain.

### 4.3.1 Groundwater flow patterns and mixing in the 2D numerical simulation with the reference values

In Figure 4.4, streamlines and the groundwater salinity distribution of the numerical simulation with the reference parameter values at the end of the last  $T_{on}$  and  $T_{off}$  periods are shown. The streamlines do not indicate fluid path lines because of transient flow (i.e., the streamlines change over time). At the end of  $T_{on}$ , the streamlines are approximately horizontal at a far distance (150 m) from the well, and a radial flow pattern is present close to the well. This radial flow pattern has a remarkable feature: some streamlines that originate from above the well travel below the well before reaching it. In Figure 4.5 the results of a simulation with the same parameters but without storage ( $S_s$  and  $S_y$  are both 0) are shown. By comparing the streamlines of the two figures, it is clear that the remarkable flow pattern is caused by storage, as in Figure 4.5 some streamlines that originate from below the well travel above the well before reaching it. In the reference simulation (Figure 4.4), a relatively large amount of water is released from storage at the water table (i.e., due to the specific yield of the aquifer). As a result, more water above the well is extracted compared to below the well, which results in an asymmetric distribution of the streamlines. In the simulation without storage, no water is released from storage at the water table. Therefore, more water below the well relative to above the well needs to be extracted, as the well is located in the upper part of the aquifer.

During  $T_{off}$  a rotational flow pattern is observed near the well (Figure 4.4), where the saline groundwater below the well flows down and induces the saline groundwater further away from the well to flow upwards. Rotational flow is common in variable density groundwater flow and has been described in previous studies (Bakker et al., 2004; Zhou et al., 2005; Eeman et al., 2011). A remarkable feature of the rotational flow is the influence of the storage parameters. In case of phreatic and elastic storage (the reference parameters, Figure 4.4), the rotation cell is only present at a distance of 20 - 30 m from the well. In case of no storage (Figure 4.5), the rotation cell extends much further, as the pressures quickly adjust to the new conditions.

Mixing was investigated by computing the relative contributions of the longitudinal ( $f_{\alpha_L}$ ), transversal ( $f_{\alpha_T}$ ) and molecular diffusion ( $f_{D_m}$ ) on total hydro-

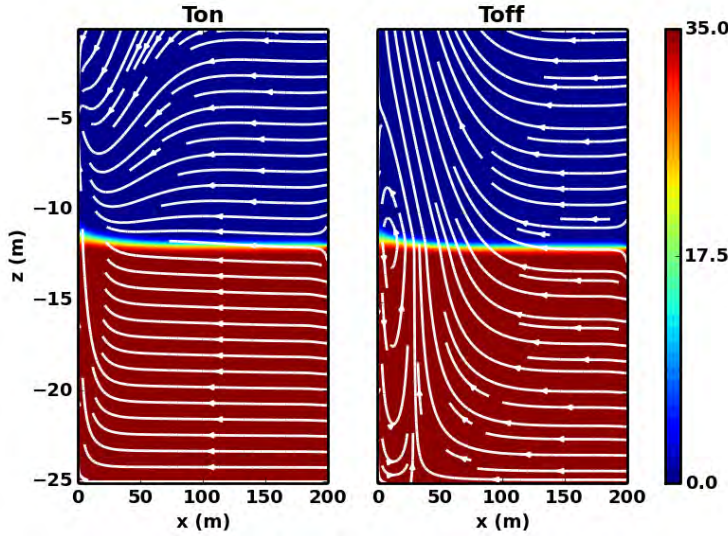


Figure 4.4: Groundwater salinity distribution ( $\text{kg m}^{-3}$ , shown in colour) and streamlines (in white) of the numerical simulation with the reference values at the end of the last periods  $T_{on}$  and  $T_{off}$ . The well is located at  $z = -7.0$  m.

dynamic dispersion during  $T_{on}$  and  $T_{off}$ , using:

$$f\alpha_L = \frac{\alpha_L v_{\perp}^2}{D_m |v| + \alpha_L v_{\perp}^2 + \alpha_T v_{\parallel}^2} \quad (4.14)$$

$$f\alpha_T = \frac{\alpha_T v_{\parallel}^2}{D_m |v| + \alpha_L v_{\perp}^2 + \alpha_T v_{\parallel}^2} \quad (4.15)$$

$$fD_m = \frac{D_m |v|}{D_m |v| + \alpha_L v_{\perp}^2 + \alpha_T v_{\parallel}^2} \quad (4.16)$$

where  $|v|$  is the magnitude of the velocity vector,  $v_{\perp}$  is the magnitude of the velocity vector component in the direction of the concentration gradient (i.e., perpendicular to the orientation of the mixing zone) and  $v_{\parallel}$  is the magnitude of the velocity vector component perpendicular to the concentration gradient (i.e., parallel to the orientation of the mixing zone). For further details on Equations 4.14 - 4.16, the reader is referred to Eeman et al. (2011). Note that the dispersive flux in the direction parallel to the mixing zone is 0. In case there is no concentration gradient (i.e., no spatial change in concentration), as is the case outside the mixing zone, the hydrodynamic dispersion flux is 0.

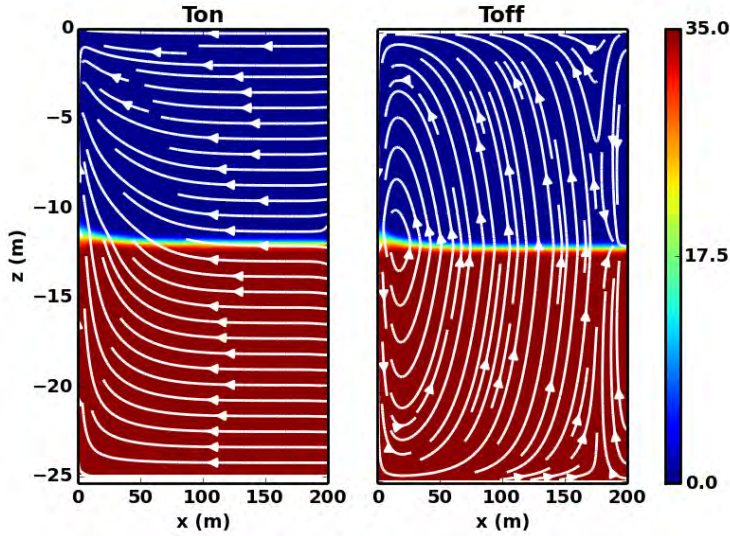


Figure 4.5: Groundwater salinity distribution ( $\text{kg m}^{-3}$ , shown in colour) and streamlines (in white) of the numerical simulation with the reference values at the end of the last periods  $T_{on}$  and  $T_{off}$ , except that no storage is simulated. The well is located at  $z = -7.0$  m.

$f\alpha_L$ ,  $f\alpha_T$ , and  $fD_m$  for the end of the last  $T_{on}$  period are shown in Figure 4.6. Close to the well, the mixing is dominated by longitudinal dispersion as the concentration gradient and the velocity vector are (nearly) parallel here. Further away from the well, the velocity vector is aligned more perpendicular to the concentration gradient, which explains the increasing values of  $f\alpha_T$ . Even further from the well, the flow velocities decrease such that  $f\alpha_T$  decreases and  $fD_m$  increases.

In Figure 4.7,  $f\alpha_L$ ,  $f\alpha_T$ , and  $fD_m$  at the end of the last period  $T_{off}$  are shown. Again, mixing near the well is dominated by longitudinal dispersion. The model simulation results at the other output timesteps showed that longitudinal dispersion was the most important mixing process below the well not only at the end of  $T_{on}$  and  $T_{off}$ , but also throughout these periods. The rotation cell is also clearly present in Figure 4.7. In the middle of the rotation cell the flow velocities are very low, so  $fD_m$  is large here. Further away from the well, in the lower part of the transition zone,  $f\alpha_L$  is relatively large. This is caused by the upward flowing groundwater (parallel to the concentration gradient), which is part of the rotation cell.  $f\alpha_T$  is small here. The dominance of the longitudinal dispersion below the well suggests that Equation 4.8 is appropriate to account for dispersion below the well, as a result of cyclic pumping. In the following two sections, this shall be discussed in more detail.

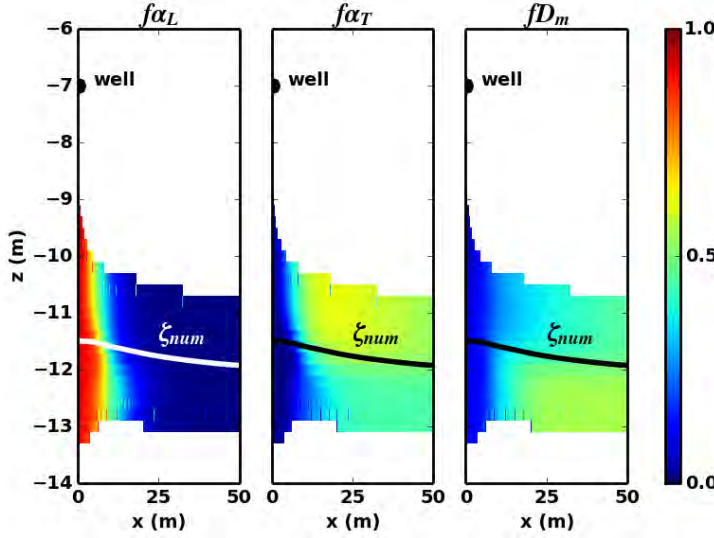


Figure 4.6: Relative contributions (scaled, from 0-1) of  $f_{\alpha_L}$ ,  $f_{\alpha_T}$ , and  $f_{D_m}$  on the total hydrodynamic dispersion at the end of the last  $T_{on}$  period. In the white region,  $f_{\alpha_L}$ ,  $f_{\alpha_T}$  and  $f_{D_m}$  are undefined as there is no concentration gradient (no spatial change in concentration). The location of the well is indicated with a black dot. The depth of the numerically calculated interface  $\zeta_{num}$  (i.e.,  $C = 0.5C_s$ ) is also indicated.

### 4.3.2 Cyclic pumping (2D conceptual model)

The accuracy of the analytical calculations with respect to cyclic pumping was investigated using  $\epsilon_\zeta$ ; the depth of the numerically simulated interface ( $\zeta_{num}$ ) minus the depth of the analytically calculated interface  $\zeta_{an}$ , at  $x = 0$  (right below the well). In Figure 4.8,  $\zeta_{num}$  and  $\zeta_{an}$  are shown throughout the pumping period  $T_p$ , in case of the reference parameters. It is clear that  $\epsilon_\zeta$  is very small throughout  $T_p$ . The interface upconing is about 0.5 m at the end of the simulated period. This is within the accuracy condition (the dimensionless interface upconing  $d_\zeta$  is lower than  $1/3$ ) that was proposed by Dagan and Bear (1968).

In Figure 4.9,  $\epsilon_\zeta$  is plotted against  $d_\zeta$  for all parameter combinations at the end of  $T_p$ . Most parameter combinations led to interface upconing within the accuracy condition  $d_\zeta < 1/3$ . For these combinations,  $\epsilon_\zeta$  is small. Therefore, the superposition principle for cyclic pumping is accurate as long as  $d_\zeta < 1/3$ .

For larger values of  $d_\zeta$ , the difference between the analytical calculations and numerical simulations (i.e., the error  $\epsilon_\zeta$ ) is significant.  $\epsilon_\zeta$  is positive for large values of  $d_\zeta$ , which indicates that in the analytical calculations the interface upconing is underestimated. Note that  $\epsilon_\zeta$  is influenced by the vertical grid discretization (0.05 m). The total volume of groundwater that is extracted ( $Q_{tot}$ ) clearly has the largest influence on interface upconing and, hence,  $\epsilon_\zeta$ .

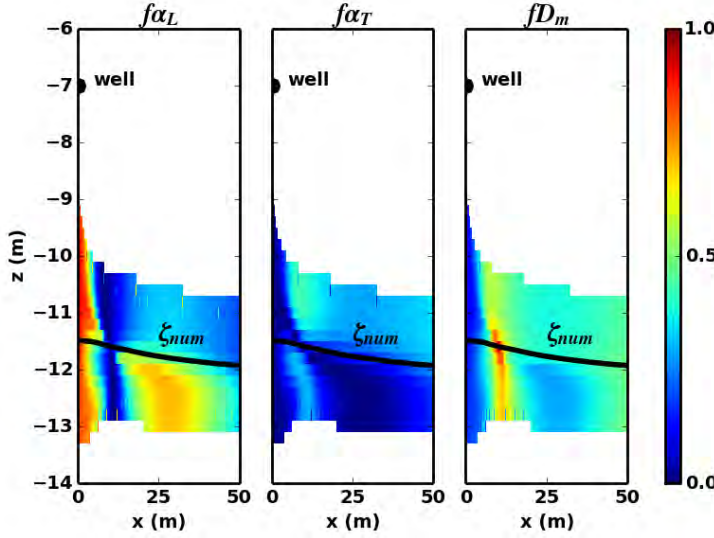


Figure 4.7: Relative contributions (scaled, from 0-1) of  $f_{\alpha_L}$ ,  $f_{\alpha_T}$ , and  $f_{D_m}$  on the total hydrodynamic dispersion at the end of the last  $T_{off}$  period.

### 4.3.3 Dispersion (2D conceptual model)

The accuracy of the analytical calculations with respect to dispersion was investigated using  $\epsilon_{1\sigma}$  and  $\epsilon_{2\sigma}$ : the difference between the numerically simulated and analytically calculated concentration contours  $C_{1\sigma}$  and  $C_{2\sigma}$ , respectively, at  $x = 0$  (right below the well). In case of the reference parameters (Figure 4.8),  $\epsilon_{1\sigma}$  and  $\epsilon_{2\sigma}$  are very small throughout  $T_p$ . Therefore, for these parameter combinations it is appropriate to use Equation 4.8 to account for dispersion.

In Figure 4.10,  $\epsilon_{1\sigma}$  and  $\epsilon_{2\sigma}$  at the end of the period  $T_p$  are plotted against  $d_\zeta$  (the dimensionless interface upconing calculated with the analytical model) for all parameter combinations. Similar as for  $\epsilon_\zeta$ , the errors  $\epsilon_{1\sigma}$  and  $\epsilon_{2\sigma}$  are positive in case of significant interface upconing, which indicates that the concentration contours are underestimated in the analytical calculations, but  $\epsilon_{1\sigma}$  and  $\epsilon_{2\sigma}$  are both higher than  $\epsilon_\zeta$ . The larger errors  $\epsilon_{1\sigma}$  and  $\epsilon_{2\sigma}$  arise because in Equation 4.8 it is assumed that the vertical flow distribution around the interface is constant, whereas in the numerical simulations the vertical flow velocity varies due to the radial flow resistance induced by the small well screen. Towards the well, the flow velocities increase inverse-proportionally, which also explains why  $\epsilon_{2\sigma}$  is higher than  $\epsilon_{1\sigma}$  at high values of  $d_\zeta$ . Moreover, in case of a wide initial mixing zone  $M$ , the errors  $\epsilon_{1\sigma}$  and  $\epsilon_{2\sigma}$  are also high.

Similar as for  $\epsilon_\zeta$ , parameter variations of  $Q_{tot}$  have the largest influence on  $\epsilon_{1\sigma}$  and  $\epsilon_{2\sigma}$ . For  $Q_{tot}$ ,  $\epsilon_{2\sigma}$  increases with increasing  $d_\zeta$  (Figure 4.10), except for  $d_\zeta = 0.35$  and  $d_\zeta = 0.43$ . In these cases,  $C_{2\sigma-num}$  has almost reached the well screen,

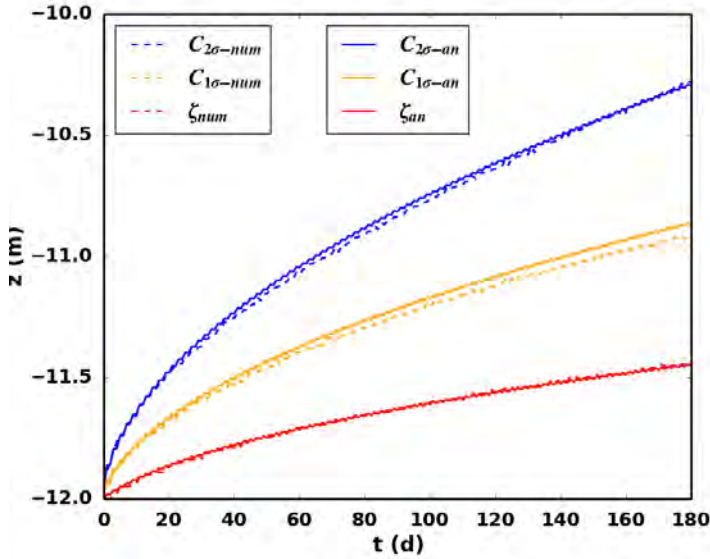


Figure 4.8: Analytically calculated depths of  $\zeta_{an}$ ,  $C_{1\sigma-an}$ , and  $C_{2\sigma-an}$  (m) (solid lines) and the numerically simulated depths of  $\zeta_{num}$ ,  $C_{1\sigma-num}$  and  $C_{2\sigma-num}$  (m) (dashed lines) below the well, using the reference parameters of the 2D numerical model. The pumping periods  $T_{on}$  and  $T_{off}$  are both 1d.

and therefore the difference with  $C_{2\sigma-an}$  decreases, which leads to a lower value of  $\epsilon_{2\sigma}$ .

For some of the  $Q_d$  and  $n_{cyc}$  parameter variations,  $\epsilon_{1\sigma}$  and  $\epsilon_{2\sigma}$  are negative. The negative values indicate that dispersion is overestimated in the analytical calculations. The overestimation can be attributed to storage. In the analytical calculations, elastic and phreatic storage are neglected, whereas in the reference parameters in the numerical simulations both elastic and phreatic storage are taken into account. The effect of the difference in storage is that saltwater upconing in the analytical calculations is higher than in the numerical simulation in case the pumping rate is high (as is the case in some of the  $Q_d$  and  $n_{cyc}$  parameter variations). In case the pumping rate is high and no storage is simulated ( $S$ )  $\epsilon_{1\sigma}$  and  $\epsilon_{2\sigma}$  are both positive. For the parameter combinations that are considered in this chapter, the effect of the storage on saltwater upconing is relatively small.

For all parameter combinations except for the variations in  $C_s$ ,  $C_{2\sigma}$  represented the drinking water standard. From Figure 4.10 it is clear that using Equations 4.4 and 4.8 to estimate the depth of the contour of the drinking water concentration below the well leads to substantial errors when  $d_\zeta$  increases, which indicates a practical limitation of the analytical solutions to estimate the safe yield in case of substantial saltwater upconing. Unfortunately, analytical solutions for radial flow

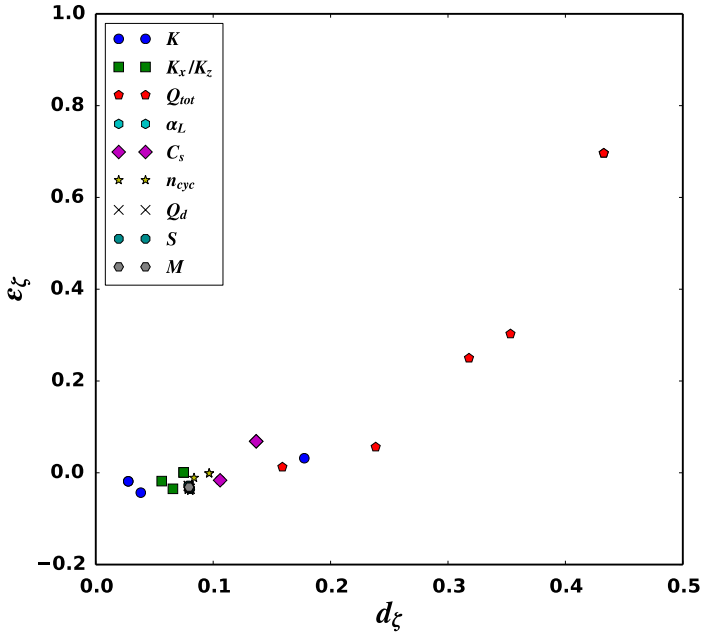


Figure 4.9:  $\epsilon_\zeta$  (m) versus  $d_\zeta$  for all parameter combinations.

problems that account for both variable density groundwater flow and dispersion are not available.

As was mentioned in the introduction of this chapter, in many previous analytical studies a critical rise of the interface in terms of  $d_\zeta$  was used to determine the safe yield of the well (i.e., when salt concentrations in the well remain sufficiently low). For the parameter combinations as listed in Table 4.1, the numerically simulated concentration in the well ( $C_{well_{num}}$ ) was compared with the analytically calculated interface upconing (expressed as  $d_\zeta$ ).  $Q_{tot}$  was not varied, but kept constant at a high value ( $108 \text{ m}^3$ ) to assure that the salinity in the well at the end of the numerical simulations was higher than  $C_{2\sigma}$  (approximately equal to the WHO drinking water limit). For  $C_s$ , an additional concentration value of  $3.5 \text{ kg m}^{-3}$  was investigated. For  $\alpha_L$ , the highest value of  $1.0 \text{ m}$  was not considered, as this value is not very realistic for the type of aquifers (geological formations) that are considered here.

In Figure 4.11,  $C_{well_{num}}$  is plotted against  $d_\zeta$  at the end of every  $T_{on}$  and  $T_{off}$  periods throughout  $T_p$ , for the three values of the maximum concentration of the ambient saline groundwater ( $C_s$ ). Remarkably,  $C_s$  has a minor influence on the degree of interface upconing (as calculated with the analytical solution) at which the WHO drinking water limit ( $0.84 \text{ kg m}^{-3}$ ) is exceeded. The drinking water

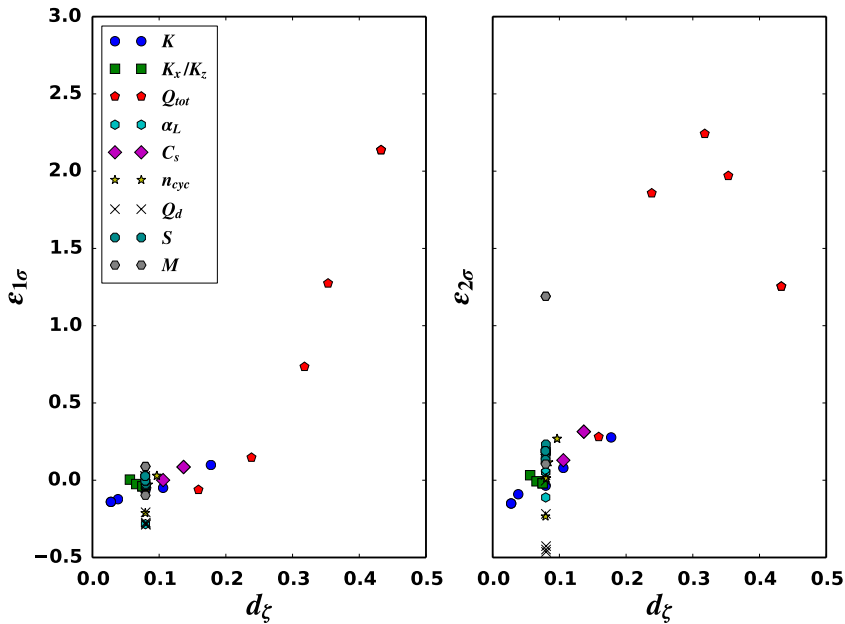


Figure 4.10:  $\epsilon_{1\sigma}$  (left) and  $\epsilon_{2\sigma}$  (right) and corresponding  $d_\zeta$  for all parameter combinations at the end of  $T_p$ .

limit in the well is exceeded at  $d_\zeta = 0.3, 0.31,$  and  $0.35$  for  $C_s = 35, 17.5,$  and  $3.5$   $\text{kg m}^{-3}$ , respectively. This can be explained by two effects that counteract each other. One effect is related to the absolute value of the concentration. The lower the maximum concentration of the saline groundwater, the lower the salinity in the well. The other effect is related to the groundwater density. The lower the groundwater density, the faster saline groundwater flows towards the well. In case the largest value of  $M$  is neglected, all parameter combinations yield a salinity lower than the drinking water in the well as long as  $d_\zeta < 1/3$ .

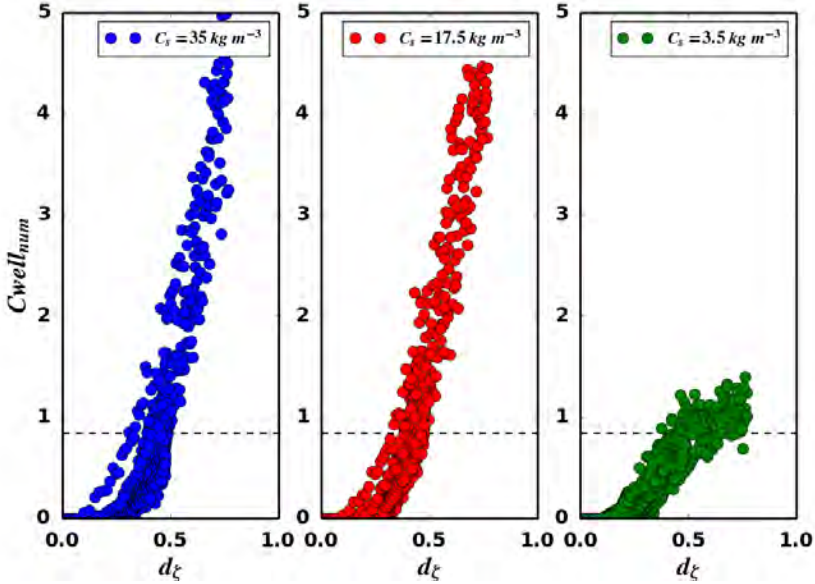


Figure 4.11:  $C_{well\_num}$  ( $\text{kg m}^{-3}$ ), the numerically simulated concentration in the well, vs.  $d_\zeta$ , at the end of every periods  $T_{on}$  and  $T_{off}$  during  $T_p$ , for the three values of  $C_s$ . The horizontal dashed line indicates the WHO drinking water limit ( $0.84 \text{ kg m}^{-3}$ )

#### 4.3.4 Horizontal wells with a finite length in a finite domain (3D conceptual model)

In the previous two sections, saltwater upconing below an infinitely long horizontal well in a domain with an infinitely long horizontal length was considered in a 2D model concept, for investigating the influence of cyclic pumping and dispersion on the analytical calculations. In this section, the accuracy of the analytical calculations with respect to the finite length of both the well and the domain (freshwater lens) is investigated, using the 3D conceptual model (Figure 4.3).

In Figure 4.12 the analytically calculated depths  $\zeta_{an}$ ,  $C_{1\sigma-an}$ , and  $C_{2\sigma-an}$  and numerically calculated depths  $\zeta_{num}$ ,  $C_{1\sigma-num}$ , and  $C_{2\sigma-num}$  below the well are shown throughout  $T_p$ , using the reference parameters of the 3D model concept. In the numerical simulation,  $\zeta_{num}$  increases from  $z = -15.5 \text{ m}$  in the beginning of the simulation, to  $z = 14.1 \text{ m}$  at the end of the simulation. In the analytical calculation,  $\zeta_{an}$  is underestimated by about  $0.35 \text{ m}$ , which is more than what was observed in the 2D model concept with the reference parameters. In both the 2D and 3D model concepts using the reference parameters, the dimensionless interface upconing  $d_\zeta$  was well below the critical value of  $1/3$ . The difference between the 2D and 3D results can be explained by the (seasonal) variation in thickness of the freshwater lens. In the 2D model concept, the freshwater lens does not vary

in thickness, due to the nature of the boundary conditions. In the 3D model concept, the thickness of the freshwater lens varies due to variation in groundwater recharge. In winter the groundwater table increases. This leads to an increase of the freshwater lens. During summer (i.e., during the pumping period  $T_p$ ) the water table decreases because there is no groundwater recharge, and fresh groundwater flows towards the ditches as a result of the hydraulic gradient. Consequently, due to buoyancy the saline groundwater moves upward by about 0.3 m, which is approximately equal to the difference between  $\zeta_{num}$  and  $\zeta_{an}$ . The errors with respect to  $C_{1\sigma}$  and  $C_{2\sigma}$  are also influenced by this effect, as well as by the initial thickness of the mixing zone  $M$ , as was explained in the previous section.

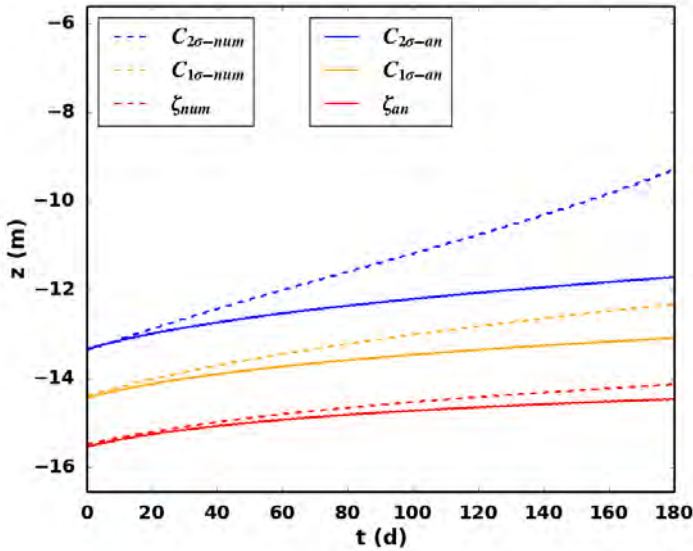


Figure 4.12: Analytically calculated depths of  $\zeta_{an}$ ,  $C_{1\sigma-an}$ , and  $C_{2\sigma-an}$  (m) (solid lines) and the numerically simulated depths of  $\zeta_{num}$ ,  $C_{1\sigma-num}$  and  $C_{2\sigma-num}$  (m) (dashed lines) below the centre of the well, using the reference parameters of the 3D conceptual model.

In Figure 4.13 the analytical and numerical results using the same parameters as the reference values, but with  $Q_{tot} = 12000 \text{ m}^3$ , are shown. As a result of the higher  $Q_{tot}$ , the saltwater upconing is larger than for the reference parameters. As expected, the differences between analytical calculations and numerical simulations with respect to  $\zeta$ ,  $C_{1\sigma}$ , and  $C_{1\sigma}$  are also larger.

For this value of  $Q_{tot}$ , the dimensionless analytically calculated interface upconing  $d_\zeta$  at the end of  $T_p$  is 0.28. The numerically simulated concentration in the well is  $0.88 \text{ kg m}^{-3}$ , which is slightly higher than the drinking water limit of  $0.84 \text{ kg m}^{-3}$ . The drinking water limit is exceeded at  $d_\zeta = 0.27$ . In the 2D numerical simulations, the concentration in the well did not exceed the drinking water

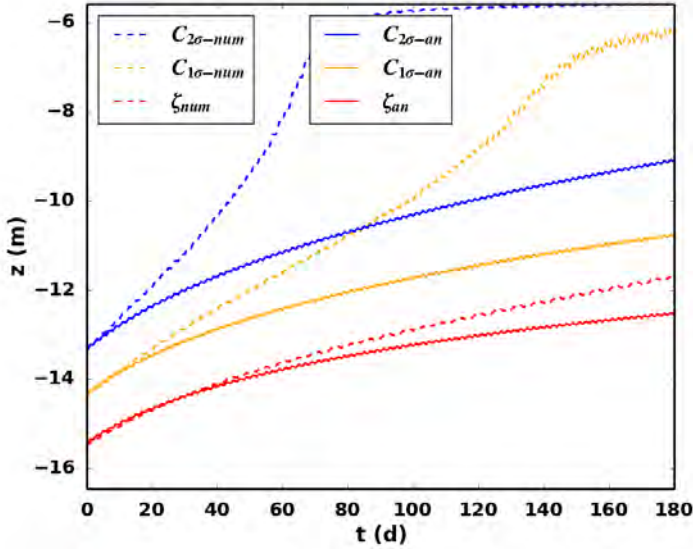


Figure 4.13: Analytically calculated depths of  $\zeta_{an}$ ,  $C_{1\sigma-an}$ , and  $C_{2\sigma-an}$  (m) (solid lines) and the numerically simulated depths of  $\zeta_{num}$ ,  $C_{1\sigma-num}$  and  $C_{2\sigma-num}$  (m) (dashed lines) below the centre of the well, using the reference parameters of the 3D conceptual model, but with a  $Q_{tot}$  of  $12000 \text{ m}^3$ .

limit as long as the corresponding dimensionless analytically calculated interface upconing was less than 0.3. The difference between the 2D and 3D results is attributed to the effect of the buoyancy of the freshwater lens, which increases the saltwater upconing below the well as described previously.

In Figure 4.14, the three variations of  $L_{well}$  are shown at the end of  $T_p$ . In all three subfigures the extraction per unit length of the well is equal to  $150 \text{ m}^3 \text{ m}^{-1}$ . Therefore, as the length of the well increases also the total extraction of the well increases. In case  $L_{well} = 80 \text{ m}$  (upper subfigure), both the analytical calculation and numerical simulation show the largest interface upconing below the centre of the well and that the interface upconing decreases towards the outer end of the well. This is attributed to the difference in flow pattern between the centre and the outer end of the well, which induces less drawdown of the water table and less saltwater upconing at the outer end of the well, compared to the centre of the well. From the outer end of the well towards the end of the freshwater lens, the difference in  $\zeta$  between the analytical and numerical results increases, which is related to the finite numerical model (i.e., the freshwater lens) and the analytical solution based on an infinite domain.

In case  $L_{well} = 320 \text{ m}$ , the analytical and numerical results show the same similarities and differences compared to  $L_{well} = 80 \text{ m}$ , except that the interface

upconing is larger as well as constant over a significant length of the well. The reason for this is that in case  $L_{well} = 320$  m, the flow pattern at the outer ends don't influence (i.e. reduce) the drawdown and the saltwater upconing at the centre, in contrast to the case where  $L_{well} = 80$  m. For  $L_{well} = 640$  m, an additional difference between the numerical and analytical results is present. The numerical simulation shows that the largest saltwater upconing occurs at the outer end of the horizontal well, not at the centre. The reason for this is that in the numerical simulation the freshwater lens decreases in the direction of the edges, and therefore also the distance between the depth of the well and the initial depth of the interface (i.e., the distance  $d$ ) decreases. Based on these results, it can be expected that the analytical solution gives appropriate indications of saltwater upconing in case the distance  $d$  does not vary significantly below the well. In case  $L_{well} = 320$  m, the numerically simulated concentration in the well did not exceed the drinking water limit in case  $d_{\zeta} = 0.27$  (the threshold that was found in case  $L_{well} = 80$  m).

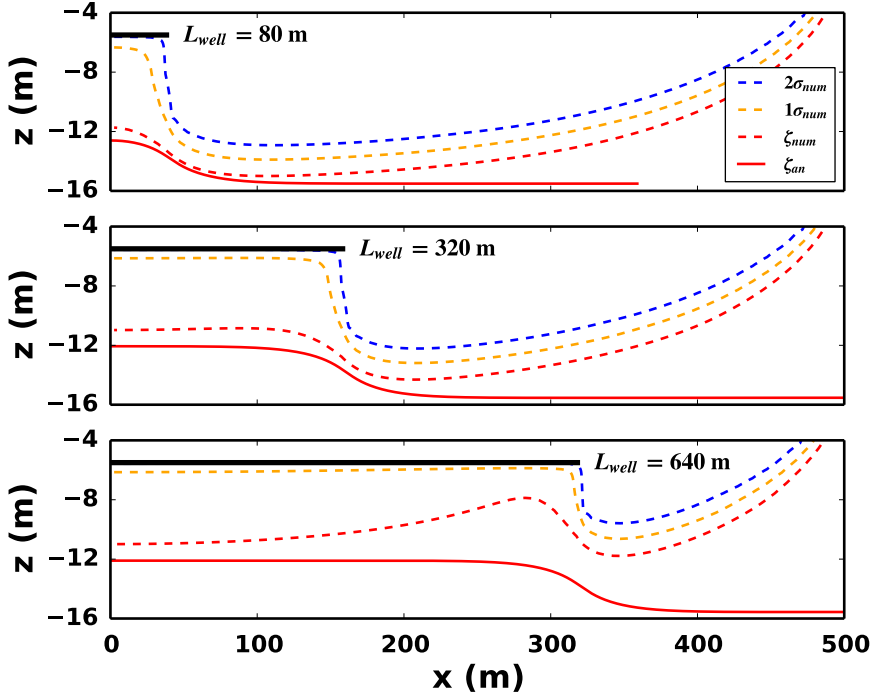


Figure 4.14: Analytically calculated depths of  $\zeta_{an}$ ,  $C_{1\sigma-an}$ , and  $C_{2\sigma-an}$  (m) (solid lines) and the numerically simulated depths of  $\zeta_{num}$ ,  $C_{1\sigma-num}$ , and  $C_{2\sigma-num}$  (m) (dashed lines) below the centre of the well, using three different lengths of the well ( $L_{well}$ ) where the extraction per unit length of the well is equal to  $150 \text{ m}^3 \text{ m}^{-1}$ . Note the values of  $L_{well}$  hold for the total length of the well, but that (given the symmetry) only half of the well is indicated. The centre of the well is located at  $x = 0$ .

## 4.4 Discussion and conclusions

### 4.4.1 Accuracy aspects

The analytical calculations of interface upconing due to cyclic pumping using the analytical solutions of Dagan and Bear (1968) were found to be accurate for a large range of parameter combinations, as long as the analytically calculated dimensionless interface upconing  $d_\zeta$  was less than about  $1/3$ . This accuracy condition agrees with the accuracy condition that Dagan and Bear (1968) proposed in view of the perturbation approximation which they used for deriving their analytical solutions. Dagan and Bear (1968) proposed the accuracy condition based on comparisons of the analytical solutions with laboratory experiments, using a steady pumping regime. This study shows that the accuracy condition that Da-

gan and Bear (1968) proposed is also appropriate for cyclic pumping, for a wide range of parameter combinations. Schmorak and Mercado (1969) also quantified the development of the salinity distribution below the well after the pumping has stopped, based on the same superposition principle as used in this chapter. Relative to the work of Schmorak and Mercado (1969), the contribution of this study is that the accuracy was investigated for a much larger range of parameter combinations, and for multiple pumping cycles. In addition, the effect of phreatic and elastic storage on saltwater upconing was investigated in this study. The effect of the storage was large for the groundwater flow patterns, but relatively minor for the saltwater upconing.

During cyclic pumping, mixing below the well was dominated by longitudinal dispersion, as the longitudinal dispersivity was an order of magnitude larger than the transverse dispersivity (conform previous studies, e.g., (Gelhar et al., 1992; Janković et al., 2009) and as the velocity vector and the concentration gradient below the well were parallel, as a result of cyclic pumping. In contrast, Reilly and Goodman (1987), Zhou et al. (2005) and De Louw et al. (2013b) found that transverse dispersion was the most important parameter for the thickness of the transition zone below the well. However, in these studies it was assumed that the flow regime is steady (i.e., no temporal changes in the pumping rate). In this study, the flow regime was unsteady (i.e., cyclic), which influenced the mixing processes.

An analytical solution for mixing by longitudinal dispersion was superimposed on the analytical interface solutions. This was appropriate in case the vertical flow velocity was about constant in the transition zone around the interface below the well. In case the mixing zone was relatively wide or in case the distance between the transition zone and the well became small, the velocity distribution in the mixing zone varied significantly, which led to errors in the dispersion approximation. This limited applicability of the analytical solution for dispersion has been described briefly in previous studies (Schmorak and Mercado, 1969; Wirojanagud and Charbeneau, 1983), but the underlying causes were not analysed as in this study.

Furthermore, this study assessed the relationship between the analytically calculated interface upconing and the numerically simulated salinity in the well. Using a 2D model, it was found that as long as the mixing zone is thin and  $d_\zeta$  remains below  $1/3$ , the simulated salinity in the well will not exceed the drinking water limit for a wide range of parameter combinations. In case of a wide mixing zone, this condition only slightly decreased; the drinking water limit in the well was exceeded in case  $d_\zeta$  is larger than  $0.3$ .

This chapter has indicated some considerations for the analytical calculation of saltwater upconing below horizontal wells with a finite length in freshwater lenses. Buoyancy can influence the accuracy of the analytical calculations as well as the salinity in the well. In case of buoyancy, the 3D numerical simulations showed that the drinking water limit was exceeded at  $d_\zeta = 0.27$ ; a lower value than what was obtained in the 2D results. As the effect of buoyancy was not investigated in great

detail, it is advised here that when estimating the safe yield of the horizontal well using the analytical solutions,  $d_\zeta$  should be kept relatively low (e.g., 0.25).

The analytical calculation of interface upconing below a horizontal well with a finite length was accurate in case the distance  $d$  below the horizontal well was constant. The accuracy of the analytical calculations was influenced by the buoyancy force on the freshwater lens. It is expected that as long as this buoyancy effect is low compared to the saltwater upconing, the error in the analytical calculations is acceptable. In view of all the comparisons between the numerical simulations and analytical calculations presented in this chapter, it is advised for practical purposes to keep the dimensionless analytically calculated saltwater upconing using the expression of Dagan and Bear (1968) below 0.25 for the estimation of the safe yield of the horizontal well.

#### 4.4.2 Considerations for applying the analytical solutions in practice

The superposition principle that was used for the analytical calculation of interface upconing due to cyclic pumping works well for the parameter combinations that were considered, provided that the dimensionless interface upconing  $d_\zeta$  remains below 1/3. It is expected that for this condition, the analytical calculations will yield the same accuracy in case of a more irregular cyclic pumping regime, as will occur in practice. The total amount of extracted water during the irrigation season strongly affects interface upconing, and therefore also for the salinity in the well.

In this study it was not investigated how long it takes before the saltwater returns to its pre-pumping depth after a period of irrigation. Zhou et al. (2005) showed that this is a lengthy process compared to saltwater upconing. The reason for this is that saltwater upconing is a local process (driven by a point sink) with a relatively large vertical hydraulic head gradient, whereas the downward movement of the interface is determined by groundwater flow on a larger scale and is driven by a smaller vertical hydraulic head gradient. Zhou et al. (2005) also showed that the transition zone that increases during the pumping period will never return to its original width. Future work should focus on the long-term effects of saltwater upconing for sustainable freshwater supply.

It was assumed in this study that the frictional head losses within the horizontal well are negligible. The frictional head loss can be estimated using (Rushton and Brassington, 2013):

$$H_f = \frac{fL_{well}v_w^2}{4gr_w} \quad (4.17)$$

$H_f$  is the frictional head loss [L] at the end of the well (i.e., the pump is assumed to be located at the other outer end of the well),  $f$  the friction factor [-] which can vary between 0.06 and 0.08. Furthermore,  $v_w$  is the average flow velocity in the well and  $r_w$  is the radius of the well. In case the head losses are

significant, the inflow along the horizontal well varies significantly. Moreover, even if the frictional head loss in the horizontal well is negligible, the inflow along the horizontal well varies as the flow pattern at the edges of well is different than in the centre of the well. If these issues are addressed and the variation of inflow along the well is calculated or measured, the superposition principle can be used by giving each point sink along the horizontal well an extraction rate according to the calculated inflow along the well.

The final note in this section is on numerical groundwater flow codes based on the interface approach and the Dupuit assumption (e.g., (Bakker, 2003)). In case the Dupuit assumption is adopted, the resistance to vertical flow is neglected, although vertical flow itself (and hence, interface upconing) is not. Numerical codes based on the interface approach and the Dupuit assumption are computationally more attractive than numerical models based on the miscible approach, where the Dupuit assumption is not adopted. However, for the cases that were considered in this study, the Dupuit assumption is not likely to hold, due to the rather high pumping rates that induce large vertical hydraulic head gradients. Also, from the analytical solutions it can be deduced that the distance between the well and the initial depth of the interface is an important parameter that influences the salt-water upconing. In case the Dupuit assumption is adopted and the aquifer is not discretized in the vertical, this distance cannot be specified.

## 4.5 Appendix : Parameter variations in the 2D model concept

As certain parameters of the 2D model are related, a complete overview of all parameter combination was, for brevity, not given in Table 4.1. In Table A in this Appendix, a complete overview of the parameter combinations is given. Per parameter, the reference value is indicated between parentheses and the variation of that parameter is shown on the same line. Below that line, the actual combination of parameters is given. For example, for the parameter variation  $Q_d = 20.0 \text{ m}^3 \text{ m}^{-1} \text{ d}^{-1}$ ,  $T_{on}$  (period of pumping) was set to 0.01 d, and  $T_{off}$  (period of no pumping) to 1.99 d. This yields, together with the reference value for the number of pumping cycles ( $n_{cyc} = 90$  d), the reference value for  $T_p$  (180 d), and the total amount of water extracted ( $Q_{tot}$ ), i.e.,  $90 (n_{cyc}) * 0.01 \text{ d} (T_{on}) * 20 \text{ m}^3 \text{ m}^{-1} \text{ d}^{-1} (Q_d) = 18 \text{ m}^3 \text{ m}^{-1}$ . In total, 32 different parameter combinations were considered.

Table 4.3: Table A: Complete overview of the parameter combinations used for the comparison between the numerical simulations and analytical calculations using the 2D conceptual model.

| parameter              | variations and parameter combinations | units               |
|------------------------|---------------------------------------|---------------------|
| $Q_{tot}$ (18)         | 36, 54, 72, 80, 98                    | $m^3 m^{-1}$        |
| $Q_d$                  | 0.4, 0.6, 0.8, 1.0, 1.2               | $m^3 m^{-1} d^{-1}$ |
| $n_{cyc}$              | 180, 45, 30, 10, 1                    | -                   |
| $T_{on}$ and $T_{off}$ | 0.5, 2, 3, 9, 45                      | d                   |
| $Q_d$ (0.2)            | 20.0, 4.0, 2.0, 0.4, 0.16, 0.13, 0.11 | $m^3 m^{-1} d^{-1}$ |
| $T_{on}$               | 0.01, 0.05, 0.1, 0.5, 1.2, 1.5, 1.8   | d                   |
| $T_{off}$              | 1.99, 1.95, 1.9, 1.5, 0.8, 0.5, 0.2   | d                   |
| $K_x$ (10)             | 1, 5, 50, 100                         | $m d^{-1}$          |
| $K_x/K_z$ (1)          | 2.0, 5.0                              | -                   |
| $K_z$                  | 5.0, 2.0                              | $m d^{-1}$          |
| $C_s$ (35)             | 17.5, 8.25                            | $kg m^{-3}$         |
| $\alpha_L$ (0.1)       | 0.01, 1.0                             | m                   |
| $S$ (0.15 & 1E-5)      | 0 ( $S_y$ ), 0 ( $S_s$ )              | - and $m^{-1}$      |
| $Q_d$                  | 20.0, 4.0, 2.0, 0.4, 0.16, 0.13, 0.11 | $m^3 m^{-1} d^{-1}$ |
| $T_{on}$               | 0.01, 0.05, 0.1, 0.5, 1.2, 1.5, 1.8   | d                   |
| $T_{off}$              | 1.99, 1.95, 1.9, 1.5, 0.8, 0.5, 0.2   | d                   |
| $M$ (0)                | 1.4, 2.8                              | m                   |



## Chapter 5

# Regional scale impact of tidal forcing on groundwater flow in unconfined coastal aquifers

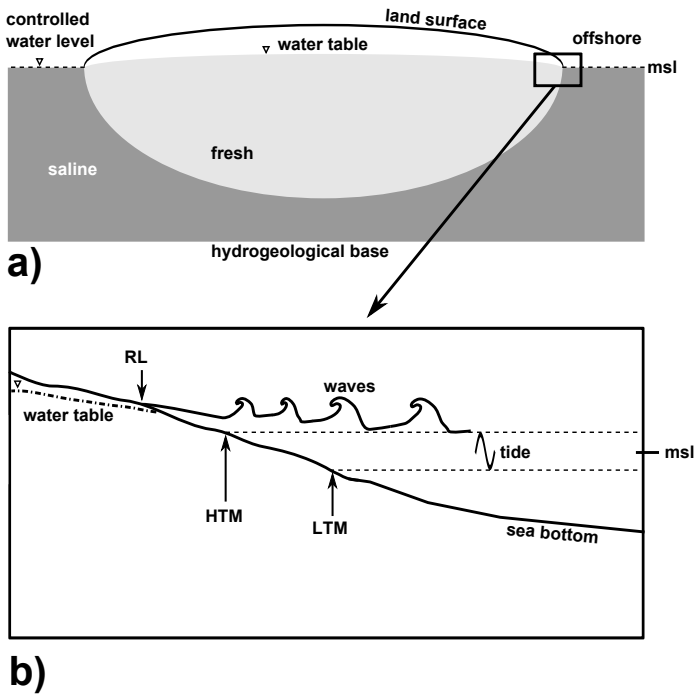
This chapter is based on: Pauw, P.S., Oude Essink, G.H.P., Leijnse, A., Vandenbohede, A., Groen, J., & Van der Zee, S.E.A.T.M. (2014). *Regional scale impact of tidal forcing on groundwater flow in unconfined coastal aquifers*. *Journal of Hydrology* 517, 269283. <http://dx.doi.org/10.1016/j.jhydrol.2014.05.042>

### 5.1 Introduction

Numerical models are widely used to quantify groundwater flow and salt transport in real-world coastal aquifers (Vandenbohede et al., 2008; Oude Essink et al., 2010; Sulzbacher et al., 2012). Assumptions and simplifications are often needed in these models to cope with computational limitations. A common assumption in regional scale models is to neglect forcing from the sea, such as tides, waves, and storm events. Several studies have shown that this assumption leads to underestimated hydraulic heads near the shore (Nielsen, 1990; Kang, 1995; Turner et al., 1995; Cartwright, 2004). However, the question that remains is: how significant is this effect on a regional scale?

Forcing from the sea results in (periodic) inundation of the intertidal area (Figure 5.1b). The zone where groundwater discharges during low tide is generally smaller than the inundation zone during high tide. Consequently, time-averaged groundwater levels are elevated compared to a situation where there is no forcing from the sea (Figure 5.2) (Lebbe, 1983; Nielsen, 1990; Vandenbohede and Lebbe, 2005). This effect increases as the slope of the intertidal area and the hydraulic conductivity of the intertidal sediments decreases (Nielsen, 1990; Turner et al., 1995; Horn, 2006) and also influences the groundwater salinity distribution be-

low the intertidal area (Lebbe, 1983; Ataie-Ashtiani et al., 1999; Cartwright, 2004; Robinson et al., 2006; Thorn and Urish, 2012).



both figures not at scale

Figure 5.1: a) Conceptual cross section of the groundwater salinity distribution of a fresh-water lens on a regional scale in case of a constant mean sea level. Note that in reality a transition zone between fresh and saline groundwater exists. b) Forcing on the groundwater below the beach by waves and tides. Infiltration of seawater occurs up to the upper limit of the wave run-up at high tide (RL). In case waves are dominant, RL is situated higher and further inland than the high tide mark (HTM). A comparable effect occurs during low tide regarding the low tide mark (LTM). This wave run-up effect can have a large influence on the time-averaged groundwater levels (Nielsen, 1999). Note that the groundwater salinity distribution is not shown. Figure 5.1b was largely adopted from a more detailed figure in Nielsen (1999) (by permission).

Previous related studies have mainly considered the near-shore region, where the forcing on the groundwater levels is most pronounced (Nielsen, 1990; Turner

et al., 1995; Robinson et al., 2007). Few studies have indicated the regional scale effects (Urish and Melih, 1989; Nielsen, 1999), despite the potential influence on the location of the groundwater divide and, hence, the amount of water that discharges to the hinterland and to the sea. An important reason to neglect the highly-dynamic processes in numerical models is the high computational effort required. Some regional scale model studies have accounted for the forcing from the sea, by using time-averaged hydraulic heads in the intertidal area that were either based on field observations or manual calibration (Vandenbohede and Lebbe, 2005; Werner and Gallagher, 2006).

The objective of this chapter is to provide an estimate of the regional scale effect of tides on hydraulic heads in an unconfined coastal aquifer with an intertidal area. It is important to note here that, depending on the local conditions, waves and storm events can also have a significant, or even larger contribution on the hydraulic heads than tides (Nielsen, 1999) (Figure 5.1b) but that this is not considered here. In case waves have a significant influence, the results in this chapter should be used with caution.

The term overheight (Nielsen, 1990) is used to indicate the underestimated hydraulic heads in a model where tides are neglected. More specifically, overheight is defined here as the difference in the computed water table between a model where tides are neglected, and a model where tides are taken into account. The influence of tides on both the location and hydraulic head at the groundwater divide is jointly referred to as regional scale overheight. Using numerical models, regional scale overheight is determined for the following hydrogeological cases:

- *Freshwater lens in a deep aquifer.* In this case, the unconfined aquifer is isotropic, homogeneous and the hydrogeological base is deep enough to accommodate the entire fresh water body (Figure 5.1a).
- *Freshwater lens in a shallow aquifer.* This case is analogous to the case of a freshwater lens in a deep aquifer, except that the hydrogeological base corresponds with the maximum depth of the fresh - saline transition zone.
- *Freshwater lens in a heterogeneous subsurface.* This case consists of an example of a layered coastal aquifer system in the Netherlands and serves as an illustration of how to use the findings from the cases of the deep and shallow aquifer in a more complex subsurface.

For these cases, the freshwater lens is subjected to tidal forcing on only one side (i.e., the seaward side), which may for example be the case in coastal barriers. A shallow aquifer is considered, as Nielsen (1990) showed that the depth of the aquifer also influences the overheight. Within all the cases, a wide range of hydrogeological parameters is considered that influence the groundwater flow in the intertidal area and the adjacent aquifer. Analytical solutions are derived for the same conditions and are compared with the numerical model results to investigate their suitability for a simple approximation of the regional scale overheight.

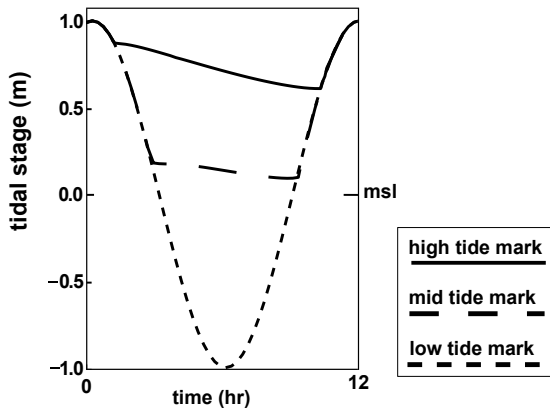


Figure 5.2: Conceptual behaviour of groundwater levels in an intertidal area around the low tide mark (LTM), the high tide mark (HTM) and in between them (mid tide mark; MTM), over one tidal cycle in case of tidal forcing. The hydraulic resistance to drainage of the intertidal area is higher than the hydraulic resistance to infiltration. To obtain a balance between inflow and outflow over a tidal cycle, the time-averaged groundwater levels inland of LTM are higher than mean sea level.

## 5.2 Material and methods

### 5.2.1 SEAWAT

SEAWAT (Langevin et al., 2007) was used to solve the following partial differential equation for variable density groundwater flow in all numerical simulations:

$$\nabla \cdot \left[ \rho \mathbf{K}_0 \left( \nabla h_f + \frac{\rho - \rho_f}{\rho_f} \nabla z \right) \right] = \rho S_s \frac{\partial h_f}{\partial t} + \theta \frac{d\rho}{dC} \frac{dC}{dt} - \rho_{ss} q_{ss} \quad (5.1)$$

where  $\rho$  is the density of the groundwater [ $\text{M L}^{-3}$ ],  $\mathbf{K}_0$  is the hydraulic conductivity tensor [ $\text{L T}^{-1}$ ],  $h_f$  is the freshwater head [L],  $z$  is the vertical coordinate [L],  $\rho_f$  is the density of fresh groundwater [ $\text{M L}^{-3}$ ],  $S_s$  is the specific storage coefficient [ $\text{L}^{-1}$ ],  $t$  is the time [T],  $\theta$  is the effective porosity [],  $C$  is the concentration [ $\text{M L}^{-3}$ ],  $\rho_{ss}$  is the density of the sink or source [ $\text{M L}^{-3}$ ] and  $q_{ss}$  is the sink and source term [ $\text{T}^{-1}$ ]. It was assumed that  $\mathbf{K}_0$  is isotropic, that the density of fresh groundwater is  $\rho_f$  is  $1000 \text{ kg m}^{-3}$  and that the maximum density of the water  $\rho_s$  is  $1025 \text{ kg m}^{-3}$ . A linear equation of state was used to calculate the density of the groundwater from concentration, whereby it was assumed that only salt concentration influences the density:

$$\rho = \rho_f + \frac{d\rho}{dC} C \quad (5.2)$$

Relative salt concentrations were used, ranging from 0 (concentration of fresh groundwater) to 1 (concentration of sea water). Hence,  $\frac{d\rho}{dC}$  equals 25.

The governing equation for salt transport in the simulations was:

$$\frac{d(\theta C)}{dt} = \nabla \cdot (\theta \mathbf{D} \cdot \nabla C) - \nabla \cdot (\mathbf{q} C) - q_{ss} C_{ss} \quad (5.3)$$

where  $\mathbf{D}$  is the hydrodynamic dispersion tensor [ $\text{L}^2 \text{T}^{-1}$ ],  $\mathbf{q}$  is the specific discharge vector [ $\text{L T}^{-1}$ ] and  $C_{ss}$  is the source and sink concentration [ $\text{M L}^{-3}$ ].

In all investigations, the groundwater flow equation and the dispersion term of the salt transport equation were formulated using a cell-centered finite difference scheme. The groundwater flow equation was solved using the PCG package. The non-advective part of the salt transport equation was solved using the GCG package. The advection term  $-\nabla \cdot (\mathbf{q} C)$  was formulated by a Lagrangian scheme and solved using the MOC solver with a relatively small Courant number (0.1) and a minimum number of 9 and a maximum number of 54 particles per cell.

### 5.2.2 Boundary conditions

The modeling of periodic groundwater flow in a regional scale model domain requires a high computational effort. To reduce the computational effort, a step-wise procedure was used to compute the overheight:

- **Constant mean sea level (CMSL) model.** First, the development of a fresh-water lens in an initially saline domain (with concentration  $C = 1$ ) was simulated using constant boundary conditions (Figure 5.3a). The hydraulic head in the offshore region  $S$  is equal to mean sea level, whereby the water flowing into the model domain has a concentration  $C$  of 1. In the hinterland region  $P$ , the water level is controlled with level  $h_P$ , again having an inflow concentration  $C = 1$ . In the region  $L$ , a recharge flux was applied with concentration  $C = 0$ . The simulations were ended when the total salt mass in the model reached a constant value.
- **Periodic sea level (PSL) model.** The concentrations and hydraulic heads of the CMSL model were used as initial conditions for the periodic sea level model. The differences compared to the CMSL model are the boundary conditions in the intertidal area ( $B$ ) and the offshore region ( $S$ ), where a tidal boundary condition was applied (Figure 5.3b and c). The simulations were ended when the time-averaged hydraulic heads (measured over one tidal cycle) and salt concentration in the intertidal area reached a constant value.
- **Time-averaged sea level model (TASL) model.** The results of the periodic sea level model were used as the initial condition for the time-averaged sea level model. In this model, constant boundary conditions were applied, similar as in the constant mean sea level model. In the intertidal area and offshore regions a constant head boundary condition was applied based on the time-averaged hydraulic heads (measured over one tidal cycle) of the periodic sea level model with concentration  $C = 1$ . The simulations were ended when the time-averaged hydraulic head at the groundwater divide and the total mass in the model reached a constant value.

The regional scale overheight was computed from the difference in hydraulic head between the CMSL and TASL models, whereby the hydraulic head was analyzed at  $x = 0.5L$ . In order to validate this step-wise approach, the TASL model was compared with a model wherein only periodic sea level was simulated. This model is referred to as 'step-wise validation model'. The boundary conditions of the step-wise validation model are equal to the ones used in the PSL model, but the initial condition for this model is a saline domain with  $C = 1$ . The step-wise validation model was ended when the time-averaged hydraulic heads in the model reached a constant value.

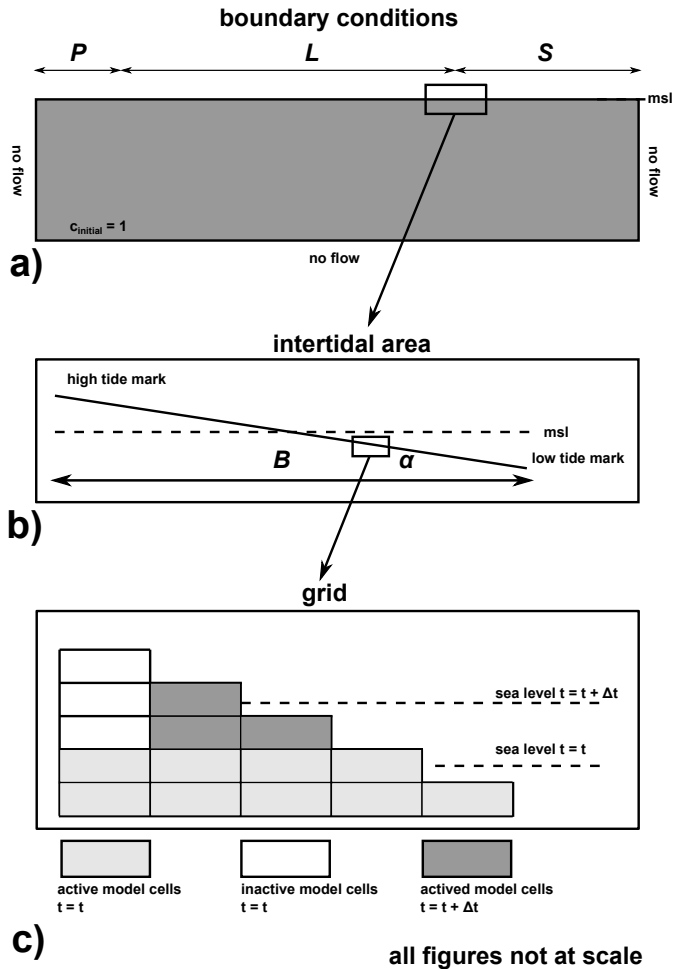


Figure 5.3: a) Boundary conditions of the constant mean sea level (CMSL) model. b) Boundary conditions of the periodic sea level (PSL) model.  $\alpha$  is the slope of the intertidal area,  $B$  is the width of the intertidal area. c) The GHB-DRN tidal boundary condition (Mulligan et al., 2011), with the method for a correct timing of the tidal signal in the intertidal area.

The tidal boundary condition in the intertidal area in the periodic sea level models consists of head-dependent flux boundary cells, which were implemented using the GHB-DRN (General Head Boundary - Drain) approach described by Mulligan et al. (2011). When, for the cells representing the surface of the intertidal area, the hydraulic head in the intertidal area is lower than the sea level during rising tide, inflow from a GHB cell occurs with an inflow concentration of 1. When the hydraulic head during falling tide is higher than the sea level and higher than the surface elevation of the intertidal area, there is outflow to a DRN cell. For further details, the reader is referred to Mulligan et al. (2011).

In the intertidal area, the maximum horizontal length of the cells was 5 m and the maximum thickness of the layers was 0.2 m. This is comparable with the number of cells Mulligan et al. (2011) used for discretizing the intertidal area. The cell size gradually increases away from the intertidal area to maximum values of 50 m for the horizontal and 5 m for the vertical dimension. Using stress periods of 15 minutes and 1-minute long flow and solute transport time steps, the following general form of the tidal oscillation was discretized:

$$h(t) = h_0 + A \sin(\omega t - \phi) \quad (5.4)$$

where  $h(t)$  is the sea level at time =  $t$ ,  $h_0$  is the reference hydraulic head (mean sea level),  $A$  is the tidal amplitude [L],  $\omega$  is the frequency [ $T^{-1}$ ] ( $2\pi T^{-1}$ , where  $T$  is the period [T]) and  $\phi$  is the phase shift []. The effect of waves, spring and neap tides and wind effects on the water level were not considered. The terms 'tidal forcing' and 'tides' (a result of tidal forcing) therefore refer to diurnal variations.

The original GHB-DRN tidal boundary approach of Mulligan et al. (2011), only prescribes the boundary condition for the uppermost cells that represent the surface of the intertidal area. If the slope of the intertidal area is small and the hydraulic conductivity of the intertidal sediment is large (Table 5.1), a relatively large number of cells fall dry during falling tide (i.e., they become inactive in the simulation). Subsequently, upon inundation of the intertidal area during rising tide, a delay of the tidal signal occurs. This can be attributed to the method of activating the inactive cells again; cells are allowed to be wetted only from below, as wetting from the horizontally adjacent cells leads to non-convergence of the flow solution (Mulligan et al., 2011). Therefore, the GHB boundary condition was prescribed for one stress period at the semi-saturated cell and across all cells that fall dry during ebb, as soon as inundation of that cell occurred due to the rising water level (Figure 5.3c). This approach effectively assumes that the saturation of the unsaturated zone is instantaneous, and that the vertical downward flow of infiltrating seawater is not associated with a large hydraulic head gradient. For implementation, this approach means that one has to know the number of de-saturated cells beforehand. Since this is not possible to determine a priori, this was done by trial and error for each model simulation. The forced activation of cells allows for the use of a relatively high (-0.1, or 10 % of the cell thickness and only wetting from below) WETDRY parameter of the BCF package. As a result, no problems with the convergence of the flow solution were encountered.

To justify this approach, a comparison was made with a simulation using the recently developed MODFLOW-NWT code (Niswonger et al., 2011). MODFLOW-NWT allows for a robust simulation of intertidal groundwater flow. Density variations were ignored and salt transport was not simulated. The results indicate a correct timing of the tidal signal, and negligible differences in hydraulic heads and fluxes between the models. For brevity, these results are omitted in this chapter.

### 5.2.3 Constant model parameters

In all the investigations, the slope of the intertidal area is constant and the groundwater recharge is constant in time and does not vary spatially. In addition, the following parameters are constant: ratio of the horizontal and vertical hydraulic conductivity (1), the specific storage coefficient ( $10^{-4} \text{ m}^{-1}$ ), specific yield (0.25), effective porosity (0.35), longitudinal dispersivity (0.25 m) and transversal dispersivity (0.025 m). The dispersivity values in this study compare well with previous related modeling work on submarine groundwater discharge (Vandenbohede and Lebbe, 2005; Robinson et al., 2007; Mulligan et al., 2011) and macro dispersivities found by e.g., Gelhar et al. (1992) and Kaleris (2006). Lebbe (1999) and Van Meir (2001) found dispersivity values from regression modeling of field data that were about three times lower than the values in this study, in a coastal aquifer of well-sorted medium to fine-medium sands. As will be shown further, the dispersivity values result in a relatively small mixing zone and in minor differences with the corresponding analytical solution that ignores dispersion. For a more detailed elaboration of dispersivity values in comparable coastal settings as in this study, the reader is referred to Eeman et al. (2012).

### 5.2.4 Freshwater lens in the deep aquifer

A dimensional analysis of the governing equations and boundary conditions for the case of the freshwater lens in the deep aquifer served as a basis for the variation of parameters, to enhance insight and efficiency. The parameter values are characteristic for regional scale freshwater lenses found in many, low lying coastal aquifers world-wide (Custodio and Bruggeman, 1987; Barlow and Reichard, 2009; Custodio, 2009). The dimensional analysis in this study is comparable to the problem that was described by Eeman et al. (2011). Therefore, many identical dimensionless groups arise. A difference compared to the dimensional analysis of Eeman et al. (2011) is the boundary condition in the intertidal area. An intertidal area with a constant slope introduces three additional dimensionless parameters:  $\alpha$ ,  $A_L$ , and  $f_{ps}$ . The derivation of these parameters is given in the Appendix of this chapter. Three dimensionless groups were varied:

- The Rayleigh number  $R$ , defined as:

$$R = \frac{\kappa g \Delta \rho_{max}}{\mu N} \quad (5.5)$$

(Eeman et al., 2011), where  $\kappa$  is the intrinsic permeability [ $L^2$ ],  $g$  is the gravitational acceleration [ $L T^{-2}$ ],  $\Delta\rho_{max}$  is the maximum density difference of between the fresh and saline groundwater [ $M L^{-3}$ ],  $\mu$  is the dynamic viscosity [ $M L^{-1} T^{-1}$ ] and  $N$  is the precipitation rate [ $L T^{-1}$ ]. As  $\rho_{max}$  was held constant, it was replaced by  $\rho_f$  in this chapter for convenience.

- The scaled amplitude  $A_L$ , defined as:

$$A_L = \frac{L}{A} \quad (5.6)$$

where  $A$  is the tidal amplitude [L] and  $L$  is the width of the freshwater lens in vertical cross section [L].

- The slope of the intertidal area  $\alpha$ :

$$\alpha = \frac{2A}{B} \quad (5.7)$$

where  $B$  is the width of the intertidal area [L].

$R$  was analyzed because this group has a significant effect on both the lens thickness and the hydraulic heads (Eeman et al., 2011). To vary this group, only the recharge rate  $N$  and the freshwater hydraulic conductivity  $K$ , which is here defined as  $\frac{\kappa g \rho_f}{\mu}$ , were varied and the value of  $R$  is expressed as the ratio  $\frac{K}{N}$ , such that it can be interpreted physically as the ratio of the freshwater hydraulic conductivity and the recharge rate. For the remaining part of this chapter, the freshwater hydraulic conductivity is simply denoted as 'hydraulic conductivity'. Variations in  $A_L$  and  $\alpha$  were chosen because they characterize the intertidal area.  $f_{ps}$  contains the frequency of the tidal oscillation, the effective porosity, the width of the freshwater lens and the precipitation rate. This group was not considered explicitly, but varies upon variation of  $A_L$  and  $R$ . For the parameters  $N$ ,  $K$ ,  $L$ ,  $A$ , and  $\alpha$ , a reference value and variations were chosen (Table 5.1). For  $\alpha$ , only the width of the intertidal area  $B$  was varied, as  $A$  also appears in  $A_L$ . The range of  $\alpha$  represents intermediate to dissipative intertidal area profiles (Wright and Short, 1984; Reis and Gama, 2010).

For the analytical solution, the time-averaged hydraulic head at the high tide mark from the corresponding numerical model functions as a boundary condition. The analytical solution is based on the solution of Van Dam (1983), who assumed mean sea level at the offshore boundary. The derivation of his analytical solution is based upon three governing equations to describe steady state flow in an unconfined coastal aquifer (Figure 5.4):

Table 5.1: Parameters used in the case of the freshwater lens in a deep aquifer. '(ref)' refers to the reference value.

| Dimensionless group | Parameter values  | Group value |
|---------------------|---|-------------|
| $R$                 | $K = 5 \text{ m d}^{-1}$ , $N = 0.002 \text{ m d}^{-1}$   | 2500        |
| $R$ (ref)           | $K = 10 \text{ m d}^{-1}$ , $N = 0.001 \text{ m d}^{-1}$  | 10000       |
| $R$                 | $K = 20 \text{ m d}^{-1}$ , $N = 0.0005 \text{ m d}^{-1}$ | 40000       |
| $\alpha$            | $A = 1 \text{ m}$ , $B = 200 \text{ m}$                   | 0.01        |
| $\alpha$            | $A = 1 \text{ m}$ , $B = 100 \text{ m}$                   | 0.02        |
| $\alpha$ (ref)      | $A = 1 \text{ m}$ , $B = 50 \text{ m}$                    | 0.04        |
| $\alpha$            | $A = 1 \text{ m}$ , $B = 25 \text{ m}$                    | 0.08        |
| $\alpha$            | $A = 1 \text{ m}$ , $B = 20 \text{ m}$                    | 0.10        |
| $A_L$               | $L = 1000 \text{ m}$ , $A = 2.0 \text{ m}$                | 500         |
| $A_L$               | $L = 1600 \text{ m}$ , $A = 1.6 \text{ m}$                | 1000        |
| $A_L$ (ref)         | $L = 2000 \text{ m}$ , $A = 1.0 \text{ m}$                | 2000        |
| $A_L$               | $L = 3200 \text{ m}$ , $A = 0.8 \text{ m}$                | 4000        |
| $A_L$               | $L = 4000 \text{ m}$ , $A = 0.5 \text{ m}$                | 8000        |

Darcy's law and the Dupuit assumption:

$$q = -K(H + h)\frac{dh}{dx} \quad (5.8)$$

the continuity equation:

$$dq = Ndx \quad (5.9)$$

and the Badon Ghijben - Herzberg relationship:

$$h = \delta H \quad (5.10)$$

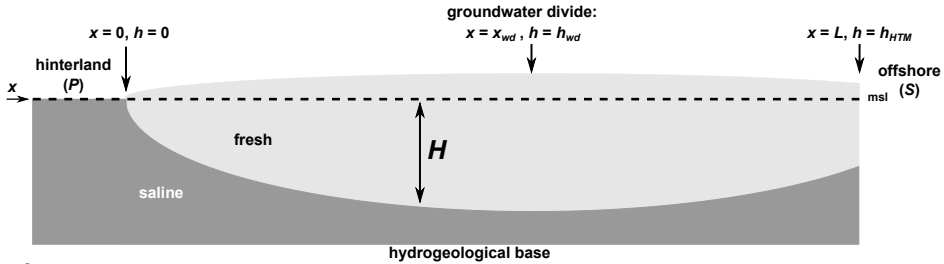
where  $q$  is the volumetric discharge per unit width of the aquifer [ $L^2 T^{-1}$ ],  $H$  is the depth of the sharp saline-fresh groundwater interface (absolute, and referenced from msl / x-axis) [L],  $x$  is the horizontal coordinate (origin at the boundary between regions  $P$  and  $L$  (Figure 5.3a)) [L],  $h$  is the hydraulic head (0 in case of msl) [L] and  $\delta$  is the relative density difference ( $\frac{\rho_s - \rho_f}{\rho_f}$ ). Combining equations 5.8 - 5.10 and integration yields, after rewriting, the following equation to compute the hydraulic head at location  $x$ :

$$h(x) = \delta \sqrt{\frac{-Nx^2 - 2C_1x}{K\delta(1 + \delta)}} \quad (5.11)$$

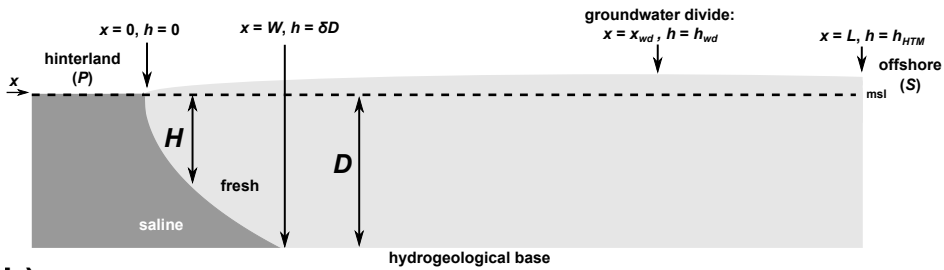
with  $C_1$ :

$$C_1 = \frac{\left(\frac{h_{HTM}}{\delta}\right)^2(\delta K + \delta^2 K) + NL^2}{-2L} \quad (5.12)$$

The location of the groundwater divide can be found by taking the derivative of equation 5.11 with respect to  $x$ . Note that  $L$  in the time-averaged sea level model is related to  $L$  in the corresponding analytical model by  $L(\text{numerical}) = L(\text{analytical}) + 0.5B$ , as the mean sea level elevation is located in the middle of the intertidal area.



a)



b)

both figures not at scale

Figure 5.4: a) Freshwater lens in a deep aquifer.  $x_{wd}$  is the horizontal location of the groundwater divide,  $h_{wd}$  is the hydraulic head of the groundwater divide. b) Freshwater lens in the shallow aquifer.  $D$  is the thickness of the aquifer, relative to mean sea level.

### 5.2.5 Freshwater lens in the shallow aquifer

The aquifer is underlain by an impermeable layer at -20 m msl (Figure 5.4). The variation of the parameters is shown in Table 5.2, including the different controlled water levels in the region  $P$ .

For the analytical model of the shallow aquifer, the equation for solving the hydraulic head in the region  $0 \leq x \leq W$  is given as:

$$h(x) = \delta \sqrt{\frac{-Nx^2 + 2Nx_{wd}x}{K(1+\delta)\delta}} \quad (5.13)$$

Table 5.2: Parameters used in the case of the freshwater lens in the shallow aquifer.

| Dimensionless group | Parameter values   | Group value |
|---------------------|--|-------------|
| $R$ (ref)           | $K = 10 \text{ m d}^{-1}$ , $N = 0.001 \text{ m d}^{-1}$ | 10000       |
| $\alpha$            | $A = 1 \text{ m}$ , $B = 25 \text{ m}$                   | 0.08        |
| $\alpha$ (ref)      | $A = 1 \text{ m}$ , $B = 50 \text{ m}$                   | 0.04        |
| $\alpha$            | $A = 1 \text{ m}$ , $B = 100 \text{ m}$                  | 0.02        |
| $A_L$               | $L = 1000 \text{ m}$ , $A = 0.5 \text{ m}$               | 2000        |
| $A_L$ (ref)         | $L = 1000 \text{ m}$ , $A = 1.0 \text{ m}$               | 1000        |
| $A_L$               | $L = 1000 \text{ m}$ , $A = 2.0 \text{ m}$               | 500         |

At  $x = W$  (the location of the saltwater wedge),  $H$  is equal to the depth of the aquifer  $D$  (absolute, and referenced from msl / x-axis), so:

$$D^2(x = W) = \frac{-NW^2 + 2Nx_{wd}W}{K(1 + \delta)\delta} \quad (5.14)$$

$W$  can be found by finding the roots of this equation.

For the region  $W \leq x \leq L$ , a general equation to describe flow in a shallow unconfined aquifer using the Dupuit assumption was used (Bear, 1972):

$$h(x) = \sqrt{(D + \delta D)^2 - \frac{(D + \delta D)^2 - (h_{HTM} + D)^2}{L - W}(x - W) + \frac{N}{K}((L - x)(x - W)) - D} \quad (5.15)$$

Equations 5.13, 5.14 and 5.15 were solved iteratively by adjusting  $x_{wd}$ , until  $h_{wd}$  is equal in equations 5.13 and 5.15.

This analytical solution applies for the cases where  $\frac{h_{HTM}}{\delta} \geq D$ . An analytical solution for a saltwater wedge (cf. equations 5.13 and 5.14) in case  $\frac{h_{HTM}}{\delta} < D$  resulted in a large difference with the numerical model regarding the location and hydraulic head of the groundwater divide. This can be attributed to the presence of the upper saline plume, which significantly reduces the length of the saltwater wedge, as was shown by Kuan et al. (2012).

For the three cases with a different hydraulic head in the region  $P$  ( $h_P$ ), the following equation for the hydraulic head in the region  $0 \leq x \leq L$  (cf. Bear (1972)) was used:

$$h(x) = \sqrt{(D + h_P)^2 - \frac{(D + h_P)^2 - (h_{HTM} + D)^2}{L}x + \frac{N}{K}(L - x)x - D} \quad (5.16)$$

Note that it is assumed here that  $\delta D \leq h_P$ .

## 5.2.6 Freshwater lens in the heterogeneous subsurface

For the investigation of a freshwater lens in the heterogeneous subsurface, a cross sectional model was constructed of a field situation in the Netherlands. The model was calibrated using borehole logs, hydraulic head data, ground time-domain electromagnetic soundings, a smooth inversion model of an airborne electromagnetic (AEM) survey (for comparable examples see Viezzoli et al. (2010); Faneca Sánchez et al. (2012)), and pressure transducer data in the intertidal area. For further details, we refer to Pauw et al. (2009). Figure 5.5 shows the boundary conditions and the distribution of the hydrogeological units that were used to model the heterogeneous distribution of the hydraulic conductivity. In the intertidal area  $B$ , the time-averaged hydraulic heads are based on pressure transducer data. At the high tide mark, the time-averaged hydraulic head amounts 0.4 above msl. The length of the intertidal area is approximately 50 m.

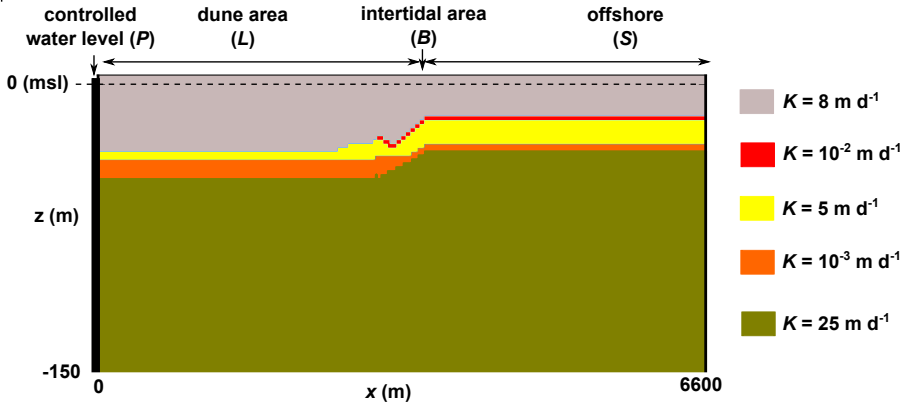


Figure 5.5: Overview of the boundary conditions and distribution of hydrogeological units of the model of the freshwater lens in the heterogeneous subsurface. The right and bottom boundaries are no-flow boundaries. The left boundary (the hinterland  $P$ ) is a constant hydraulic head and constant concentration boundary. The isotropic hydraulic conductivity values are displayed at the right. Note that  $B$  is a region (intertidal area), but that for scaling reasons it is indicated here with a single arrow.

## 5.3 Results

### 5.3.1 Validation of the step-wise approach

For the validation of the step-wise approach a relatively small model domain was used. The hydrogeological base of the aquifer is located at 10 m below mean sea level, the freshwater lens is 1000 m wide, the tidal amplitude is 1.0 m, the recharge rate is  $0.001 \text{ m d}^{-1}$ , the isotropic hydraulic conductivity is  $10 \text{ m d}^{-1}$  and the slope of the intertidal area is 0.02. The change of the hydraulic head at  $x = 0.5L$  as a function of time is shown in Figure 5.6. The hydraulic head at  $x = 0.5L$  increases rapidly in the first three years. Hereafter, the increase attenuates and stabilizes after approximately 20 years. A small depression is present between 3 and 5 year of simulation time, which can be attributed to the development of the upper saline plume in the intertidal area. In the constant mean sea level model, this depression is absent because there is no tidal forcing. The hydraulic head at  $x = 0.5L$  at the end of constant mean sea level model is lower than the hydraulic head at  $x = 0.5L$  at the end of the step-wise validation model, viz. the overheight at location  $x = 0.5L$  is 0.28 m.

In the periodic sea level model, the hydraulic head at  $x = 0.5L$  increases in the course of one year. It must be noted here, that the time-averaged hydraulic head at the high tide mark reached a stable value already after approximately 0.3 yr. However, as the time to reach a constant time-averaged hydraulic head at the high tide mark cannot be determined a priori, the simulation time of the periodic sea level model is longer. The time-averaged sea level model shows that the hydraulic head at  $x = 0.5L$  increases slightly during two years, after which it reaches a stable value. The overheight at  $x = 0.5L$ , calculated from the difference between the constant mean sea level model and the time-averaged mean sea level model, equals 0.28 m. This corresponds to the overheight calculated from the step-wise validation model. It should be noted here that this correspondence in overheight not only holds for  $x = 0.5L$ , but along the total width  $L$  of the freshwater lens. This example shows that the step-wise approach is appropriate to investigate the regional scale overheight.

Figure 5.7 suggests that there is also a reasonable correspondence in the ground-water salinity distribution between the step-wise validation model and the time-averaged sea level model. For this set of parameters though, the upper saline plume does not have a stable shape. Due to the observed fingering patterns and the unstable density distribution, the unstable shape of the upper saline plume is explained here by free convection processes. Free convection in the upper saline plume was also present in some of the other simulations. However, it is beyond the scope of this study to investigate the parameters that govern free convection in the intertidal area.

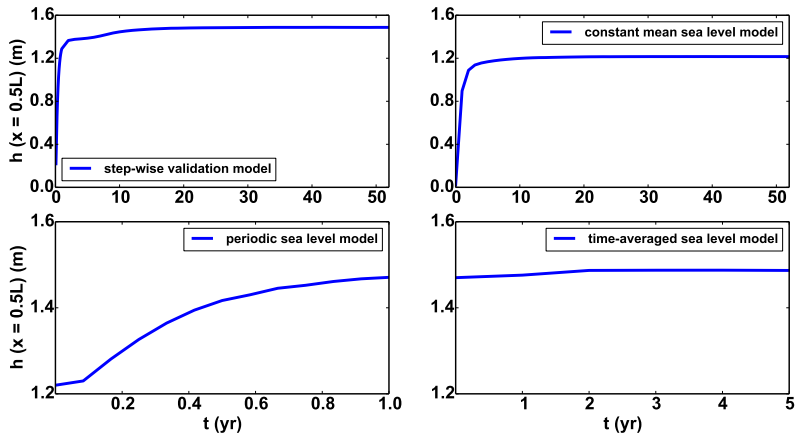


Figure 5.6: The change of the hydraulic head at  $x = 0.5L$  for the step-wise validation model, mean sea level model, periodic sea level model and time-averaged sea level model. Note that the upper and lower subfigures have different horizontal and vertical scales.

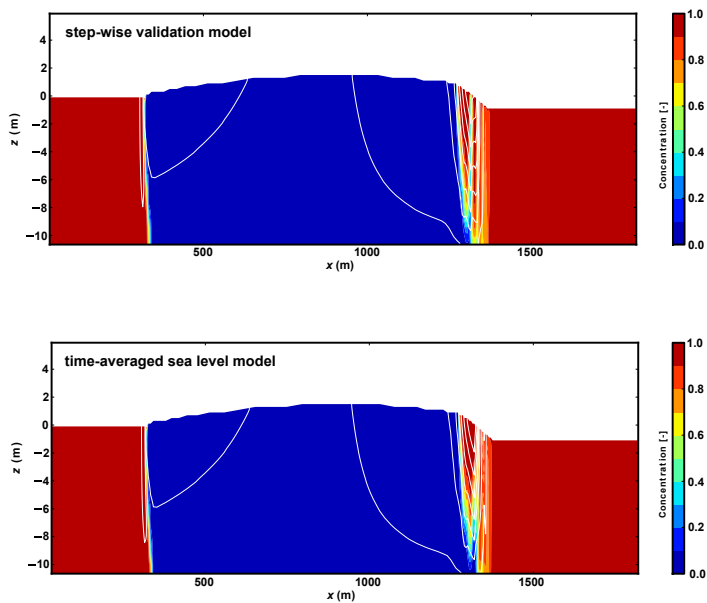


Figure 5.7: The groundwater salinity distribution and streamlines (in white) of the step-wise validation model and the time-averaged sea level model.

### 5.3.2 Freshwater lens in the deep aquifer

Figure 5.8 depicts the time-averaged hydraulic head at the high tide mark ( $h_{HTM}$ ) for the combinations of dimensionless groups. The relation of  $h_{HTM}$  with the different values of the dimensionless groups is in line with what can be expected qualitatively from previous investigations (Lebbe, 1983; Nielsen, 1990; Turner et al., 1995). An increase of the Rayleigh number  $R$  results in a lower  $h_{HTM}$  because a more permeable intertidal area is easier to drain than a less permeable one. An increase of the slope of the intertidal area  $\alpha$  results in faster drainage of the intertidal area, so  $h_{HTM}$  therefore decreases. As the Scaled Amplitude  $A_L$  increases, more water infiltrates in the intertidal area due to an increase of the tidal amplitude, so  $h_{HTM}$  increases. The sensitivity of  $\alpha$  and  $A_L$ , indicated by the slope of the lines in Figure 5.8, increases with a decrease of  $R$ . Hence, for a less permeable intertidal area, changes in the slope of the intertidal area and in the tidal amplitude are more outspoken compared to a more permeable intertidal area.

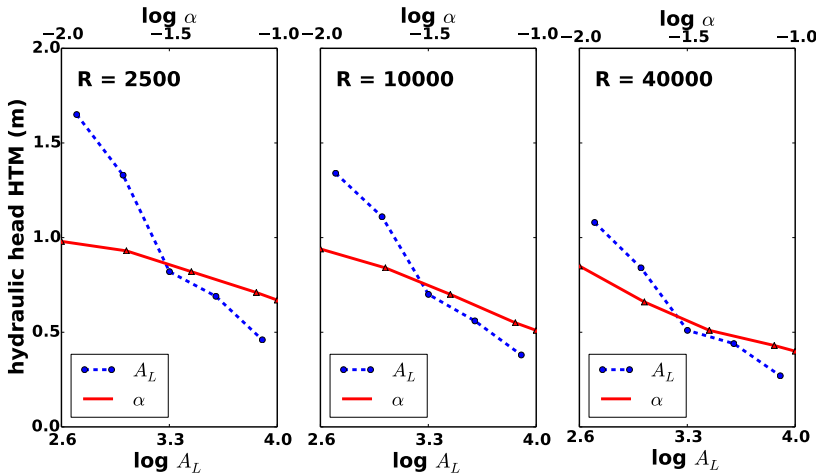


Figure 5.8: Time-averaged head at the high tide mark (HTM) for all the combinations of dimensionless groups for the freshwater lens in a thick aquifer.

Figure 5.8 suggests an approximately linear relationship between  $h_{HTM}$  and the log-transformed values of the three dimensionless groups. For the dominant parameters of the groundwater flow in the intertidal area ( $K$  (m/d),  $A$  (m), and  $\alpha$ ), the following linear equation was fitted:

$$h_{HTM} = c_1 + c_2 \log A + c_3 \log \alpha + c_4 \log A \log \alpha \quad (5.17)$$

with  $c_1 = -0.332 \log K + 0.652$ ,  $c_2 = -1.744 \log K + 3.519$ ,  $c_3 = 0.083 \log K - 0.368$  and  $c_4 = 0.033 \log K - 0.103$ .

Note that this equation implicitly assumes that the influence of  $L$  and  $N$  on  $h_{HTM}$  is negligible for the parameter range that is considered here. In other

words, the flow of fresh groundwater from the hinterland to the sea does not have a significant influence on the decrease of the hydraulic heads in the intertidal area during falling tide (again, for the considered parameter range). The root mean square (RMS) error of this relationship is 0.09 m, which indicates that the assumption is reasonable. The error especially increases when the width of the freshwater lens is large compared to the width of the intertidal area (i.e., for high values of  $A_L$ ). In these cases,  $h_{HTM}$  is underestimated, so the influence of the offshore directed flow of fresh groundwater has some influence. Fortunately, as will be explained further, the influence on the regional scale overheight is in these cases low. If the three largest values of  $A_L$  are taken out of the RMS calculation, the RMS decreases to 0.08 m and all values for  $h_{HTM}$  can be estimated within 0.1 m.

Figure 5.9 shows the relative hydraulic head change at  $x = 0.5L$ , for the dimensionless groups  $A_L$  and  $\alpha$ . The relative hydraulic head change  $\Delta h'$  is used as a measure for the (relative) overheight:

$$\Delta h' = \left( \frac{h_{TASL}}{h_{CMSL}} - 1 \right) 100 \quad (5.18)$$

where  $h_{TASL}$  is the hydraulic head in the time-averaged sea level model and  $h_{CMSL}$  is the hydraulic head in the constant mean sea level model, both at  $x = 0.5L$ . The rationale of defining a relative overheight is related to scaling; the absolute 'error' (i.e., the underestimated hydraulic head) that is introduced in a model if tidal forcing is neglected becomes less 'important' when the scale of the problem (and hence, the hydraulic head) increases. The absolute error can be estimated using the hydraulic head at  $x = 0.5L$  from the corresponding analytical solution. According to the analytical solution, the hydraulic head at  $x = 0.5L$  is equal to 1.56 m. Figure 5.9 shows that  $\Delta h'$  is approximately 4%. Hence, the hydraulic head at  $x = 0.5L$  in the simulation where tidal forcing is taken into account is 1.62 m.

Figure 5.9 shows that  $\Delta h'$  increases with increasing values of  $R$ . This behavior is different from the influence of  $R$  on the overheight at the high tide mark. The influence of the overheight at the high tide mark on the hydraulic heads further inland is larger when the hydraulic head at the groundwater divide in the CMSL simulation is relatively low. As a decrease of  $A_L$  and  $\alpha$  results in a larger overheight at the high tide mark, the influence also increases for  $\Delta h'$ . The sensitivity of  $A_L$  is larger than  $\alpha$ , similar as was observed for the influence on the overheight at the high tide mark.

Figure 5.10 shows the effect of the dimensionless groups on the relative change of the groundwater divide  $\Delta x'$  (analogous to the relative overheight), which was computed with:

$$\Delta x' = \frac{x_{wd-TASL} - x_{wd-CMSL}}{0.5L} 100 \quad (5.19)$$

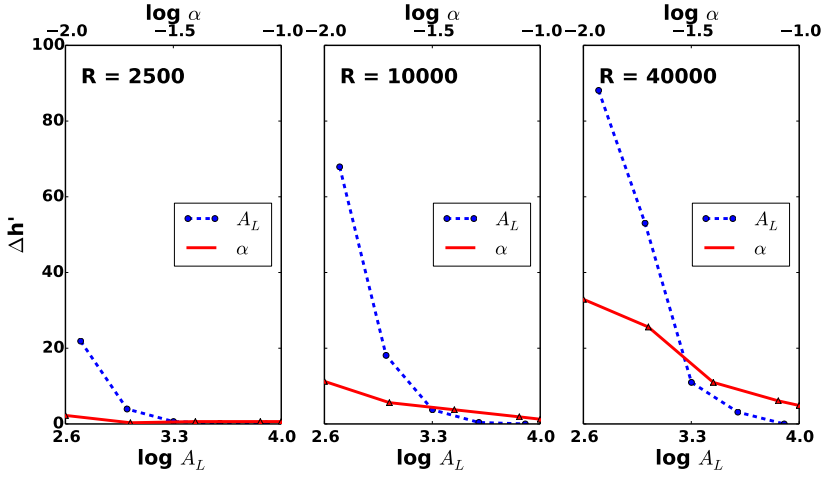


Figure 5.9: Relative change of the hydraulic head ( $\Delta h'$ ) at  $x = 0.5L$  for the combinations of the dimensionless groups  $R$ ,  $A_L$ , and  $\alpha$ .

where  $x_{wd-TASL}$  is the location of the groundwater divide in the time-averaged sea level model and  $x_{wd-CMSL}$  is the location of the groundwater divide in the constant mean sea level model. As expected, the effects of the dimensionless groups on the relative change of the groundwater divide are comparable to the effect on the relative overhead  $\Delta h'$ . The results of  $\Delta x'$  indicate how the distribution of fluxes to the hinterland and the sea change, when tidal forcing is taken into account.

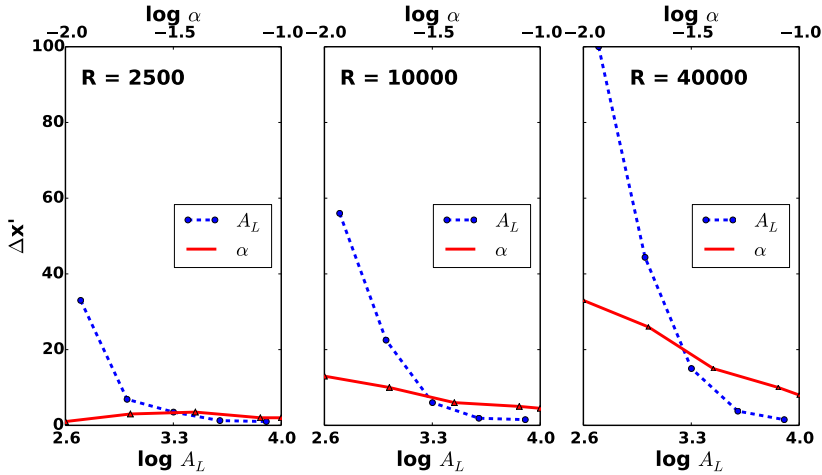


Figure 5.10: Relative change of the location of the groundwater divide ( $\Delta x'$ ) for the combinations of the dimensionless groups  $R$ ,  $A_L$ , and  $\alpha$ .

Table 5.3 shows the results of the comparison between the time-averaged sea level model and the corresponding analytical solution. The relative difference in hydraulic head at  $x = 0.5L$  ( $\Delta h'_{(num-ana)}$ ) is computed as:

$$\Delta h'_{(num-ana)} = \frac{h_{num} - h_{ana}}{h_{num}} 100 \quad (5.20)$$

where  $h_{num}$  is the hydraulic head at location  $x = 0.5L$  in the time-averaged sea level model and  $h_{ana}$  is the hydraulic head at location  $x = 0.5L$  in the corresponding analytical solution. The relative difference in location of the groundwater divide between these models  $\Delta x'_{(num-ana)}$  is computed with:

$$\Delta x'_{(num-ana)} = \frac{x_{num} - x_{ana}}{0.5L} \quad (5.21)$$

where  $x_{num}$  is the location of the groundwater divide in the time-averaged sea level model and  $x_{ana}$  is the location of the groundwater divide in the corresponding analytical solution.  $h_{num}$  and  $x_{num}$  are computed using interpolation of the two nodes of maximum hydraulic head. The estimated error due to this interpolation is in the order of 0.01 m for  $h_{num}$  and 5 m for  $x_{num}$ .

$\Delta x'_{(num-ana)}$  and  $\Delta h'_{(num-ana)}$  generally increase with increasing values of  $R$ , and decreasing values of  $\alpha$  and  $A_L$ . When the time-averaged hydraulic head at the high tide mark is high compared to the hydraulic head at the groundwater divide, the analytical model is less accurate. Negative values of  $\Delta x'_{(num-ana)}$  indicate that the computed change of the groundwater divide in the analytical equation is higher compared to the one computed with the numerical model.

Table 5.3:  $\Delta h'_{(num-an)}$  and  $\Delta x'_{wd(num-an)}$  for the combinations of dimensionless groups in the analysis of a freshwater lens in a thick aquifer.

| Dimensionless group | Group value | $\Delta h'_{(num-an)}$ | $\Delta x'_{wd(num-an)}$ |
|---------------------|-------------|------------------------|--------------------------|
| <i>R</i> = 2500     |             |                        |                          |
| $\alpha$            | 0.01        | 1.9                    | -1.5                     |
| $\alpha$            | 0.02        | 1.6                    | 0.8                      |
| $\alpha$            | 0.08        | 1.9                    | 0.8                      |
| $\alpha$            | 0.10        | 2.2                    | 0.9                      |
| $A_L$               | 500         | 1.5                    | 4.5                      |
| $A_L$               | 1000        | 0.4                    | -0.3                     |
| $A_L$               | 2000        | 1.9                    | 1.8                      |
| $A_L$               | 4000        | 1.2                    | 0.8                      |
| $A_L$               | 8000        | 1.3                    | 0.9                      |
| <i>R</i> = 10000    |             |                        |                          |
| $\alpha$            | 0.01        | 8.4                    | 3.6                      |
| $\alpha$            | 0.02        | 3.6                    | 2.7                      |
| $\alpha$            | 0.08        | 1.8                    | 2.0                      |
| $\alpha$            | 0.10        | 1.9                    | 1.9                      |
| $A_L$               | 500         | 10.3                   | -19.4                    |
| $A_L$               | 1000        | 2.7                    | 2.5                      |
| $A_L$               | 2000        | 2.4                    | 1.0                      |
| $A_L$               | 4000        | 1.6                    | 0.6                      |
| $A_L$               | 8000        | 1.3                    | 1.2                      |
| <i>R</i> = 40000    |             |                        |                          |
| $\alpha$            | 0.01        | 12.8                   | 1.9                      |
| $\alpha$            | 0.02        | 13.6                   | 7.8                      |
| $\alpha$            | 0.08        | 4.6                    | 2.5                      |
| $\alpha$            | 0.10        | 4.7                    | 1.5                      |
| $A_L$               | 500         | -7.6                   | 2.8                      |
| $A_L$               | 1000        | 14.9                   | -1.5                     |
| $A_L$               | 2000        | 6.6                    | 4.3                      |
| $A_L$               | 4000        | 3.0                    | 0.6                      |
| $A_L$               | 8000        | 2.5                    | 0.8                      |

### 5.3.3 Freshwater lens in the shallow aquifer

Figure 5.11 shows  $\Delta x'$  and  $\Delta h'$  for the dimensionless groups that were considered for the freshwater lens in the shallow aquifer. Similar to what was observed for the freshwater lens in the deep aquifer is that  $A_L$  is more sensitive than  $\alpha$ . Although different values of  $R$  were not considered for the freshwater lens in the shallow aquifer, a similar behavior can be expected as was described for the freshwater lens in the deep aquifer. Comparing the results of a deep and shallow aquifer for  $A_L = 500, 1000,$  and  $2000$  with  $R = 10000$  and  $\alpha = 0.04$ , reveals that although the absolute overheight at the high tide mark is larger in the shallow aquifer (Nielsen, 1990),  $\Delta h'$  and  $\Delta x'$  differ no more than 5 %. This is because the reduced thickness of the aquifer not only increases the overheight at the high tide mark, but also increases the hydraulic head at the groundwater divide, so that the influence of the overheight at the high tide mark on the relative regional scale overheight decreases. The difference in  $h_{HTM}$  between the cases of the deep and the shallow aquifer is within 0.05 m, except for  $A_L = 500$ , for which it is 0.21 m.

In the simulations with a higher water level in the region  $P$ ,  $\Delta h'$  was computed using the hydraulic head at the groundwater divide in the mean sea level model, because the groundwater head was not located at  $x = 0.5L$ . The values of  $\Delta h'$  for the hydraulic head at the region  $P$  of 0.5 m, 1.0 m and 1.5 m are 18 %, 10% and 5%, respectively. Hence,  $\Delta h'$  increases as the hydraulic head in the region  $P$  decreases, just like what was observed for the previous cases. Not surprisingly,  $\Delta x'$  behaves similarly.

The differences between the numerical and the corresponding analytical solutions considering the relative difference in hydraulic head at location  $x = 0.5L$ , are minor (Table 5.4). The absolute difference in hydraulic head at location  $x = 0.5L$  is within 0.1 m for all combinations of dimensionless groups. The difference regarding the location of the groundwater divide is somewhat larger, but the relative difference is  $\leq 10\%$ . The relative difference of the groundwater divide for the cases where  $P > \text{msl}$  was not considered, because the location of the groundwater divide varied between the simulations. Note that for the dimensionless group  $A_L = 1000$  the analytical solution could not be computed since  $\frac{h_{HTM}}{\delta} < D$ .

Table 5.4:  $\Delta h'_{(num-ana)}$  and  $\Delta x'_{(num-ana)}$  for the considered combination of dimensionless groups in the analysis of the freshwater lens in the shallow aquifer.

| Dimensionless group | Group value | $\Delta h'_{wd(num-ana)}$ | $\Delta x'_{wd(num-ana)}$ |
|---------------------|-------------|---------------------------|---------------------------|
| $\alpha$            | 0.08        | 1                         | 6                         |
| $\alpha$            | 0.02        | 2                         | 7                         |
| $A_L$               | 2000        | -                         | -                         |
| $A_L$               | 1000        | 2                         | 6                         |
| $A_L$               | 500         | 1                         | 7                         |
| $A_L(P = 0.5)$      | 1000        | 1                         | -                         |
| $A_L(P = 1.5)$      | 1000        | 3                         | -                         |
| $A_L(P = 2.0)$      | 1000        | 1                         | -                         |

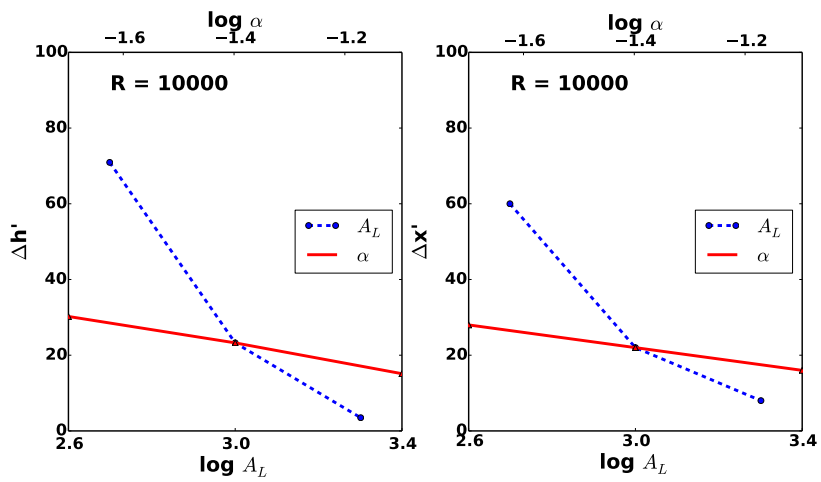


Figure 5.11: Results of the numerical simulations of the freshwater lens in the shallow aquifer.

### 5.3.4 Freshwater lens in the heterogeneous subsurface

For the freshwater lens in the heterogeneous subsurface, the time-averaged sea level model and the constant mean sea level model indicate that the regional scale overheight is minor; the difference in the computed groundwater divide is 42 m and the difference in hydraulic head is 0.01 m. Not surprisingly, the regional groundwater salinity distribution is also comparable. Figure 5.12 shows the simulated groundwater salinity distribution and the inversion model of the airborne electromagnetic (AEM) data. The 10  $\Omega\text{m}$  contour in the AEM model served as calibration for the position of the deep groundwater salinity transition zone in the numerical model. It should be noted here that this case only serves as an illustration of how to apply the findings of the previously discussed, synthetic cases to a real world case which is less idealized.

As the subsurface is heterogeneous, the analytical solutions that were derived for the shallow and the thick aquifer cannot be used directly. However, the analytical solution for the thick aquifer is used as an estimate. The harmonic average of the hydraulic conductivity and aquifer thickness of the first, second, and third aquifer is used to determine  $K$  at  $13 \text{ m d}^{-1}$ .  $A = \sim 0.8 \text{ m}$  and  $\alpha = 0.04$  because  $\sim B = 50 \text{ m}$ . From equation 5.17 the time-averaged head at high tide mark is estimated around 0.5 m. This is 0.1 m higher than the hydraulic head that was measured with pressure transducer data, which can be explained by the higher hydraulic conductivity of the intertidal sediments compared to the hydraulic conductivity of the aquifer (Pauw et al., 2009). Using equation 5.11, the absolute hydraulic head at location  $x = 0.5L$  is determined at 2.76 m msl. This is much lower than in the numerical model (4.7 m msl), and can be explained by the presence of a semi-permeable layer and the high hydraulic head that at the boundary  $P$ . The analytical solution indicates that the influence of the overheight is minor; the shift of the groundwater divide is 16 m, whereas there is essentially no difference in hydraulic head at location  $x = 0.5L$ . This estimate is within the error range of the analytical solution. Moreover, if  $R$  is increased by adjusting  $K$  to  $4.5 \text{ m d}^{-1}$ , such that hydraulic head increases according to the measured value, the analytical solution indicates an even smaller influence on the groundwater divide.

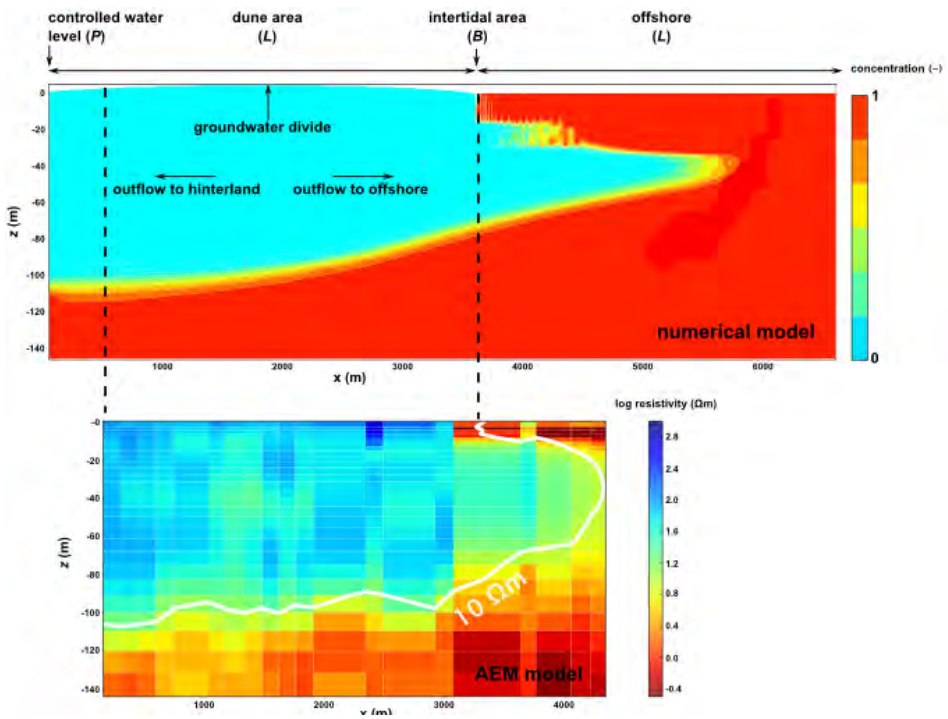


Figure 5.12: Results of the numerical simulation of the time-averaged sea level model of a regional scale freshwater lens in a heterogeneous subsurface (above), and the inversion model of AEM survey across this transect (below). Both the AEM model and numerical model indicate the presence of a freshwater tongue below the sea floor.

## 5.4 Discussion

To date, the numerical modeling of variable density groundwater flow and salt transport on a regional scale is still strongly influenced by computation time constraints (Post, 2005; Werner et al., 2013). Many studies have aimed at reducing this computational effort. Examples are vertical averaging of the governing equations (Pool et al., 2011) and sharp interface modeling (Essaid, 1986; Bakker, 2003). The computational effort is also the reason why tides are rarely taken into account in regional scale studies. Instead, the boundary condition at the land-sea boundary is often based on a constant mean sea level. The validation example of the stepwise approach nicely illustrated such a difference in computation time; on a 3 GHz desktop computer, the simulation of the model with only periodic sea level variation took approximately 6.5 days, whereas the three models in the step-wise approach together took about 8 hours. The implications for three-dimensional models are evident.

The results in this chapter can be used to estimate the effect of tidal forcing on groundwater flow. Important assumptions that were made are a constant (both in space and time) slope of the intertidal area, a diurnal tidal cycle without changes in tidal amplitude, no effects of waves and storms, a constant and equally distributed groundwater recharge and a homogeneous and isotropic porous medium. In addition, the influence of phreatic storage on the overheight was not considered. These complications may be the subject of further investigations, in particular, the effect of wave runup on the time-averaged hydraulic head at the high tide mark. In a comparison of watertable time series from a wave-exposed site and an unexposed site of the Palm Beach Isthmus (Australia), Nielsen (1999) showed that the contribution of waves on the time-averaged hydraulic head in the nearshore region was significantly larger than the contribution of tides. Despite the potential contribution of wave runup, a detailed analysis on its influence on the time-averaged hydraulic head in the nearshore region for different hydrogeological conditions is beyond the scope of this work. The results of this chapter should be considered as a conservative estimate of the overheight, especially when there is frequent wave action and the wave height is equal to or larger than the tidal amplitude.

The emphasis of this study was on the regional scale impact of tidal forcing. For local scale studies (Robinson et al., 2007; Li et al., 2009; Xin et al., 2010) the results are less relevant because the computation time is a smaller problem. In addition, in local scale studies the explicit modeling of tides is often needed to capture the governing processes of the problem at hand. Nevertheless, the results in this chapter can be used to determine the boundary conditions in the local scale model, such as the amount of fresh groundwater that flows from the groundwater divide to the intertidal area.

The analytical studies by Nielsen (1990) and Teo et al. (2003) have previously addressed the effect of tidal forcing on unconfined aquifers. The results in this chapter are complementary to the results presented in those studies, because here variable density groundwater flow, salt transport, a seepage face, precipita-

tion excess in the hinterland and other different hydrogeological conditions are considered. A comparison with the results of Teo et al. (2003), which can be considered as an extension of the work by Nielsen (1990), is not straightforward. The difficulty is due to the validity of the analytical solutions of Teo et al. (2003). Their solutions are valid for small values of the shallow water parameter  $\epsilon$  and the amplitude parameter  $\alpha$ :

$$\epsilon = \sqrt{\frac{D\omega n_e}{2K}} \quad (5.22)$$

and

$$\alpha = \frac{A}{D} \quad (5.23)$$

where  $D$  is the still water table height,  $\omega$  is the tidal wave frequency,  $n_e$  is the porosity,  $K$  is the hydraulic conductivity of the aquifer and  $A$  is the tidal amplitude. For the hydrogeological conditions that were considered,  $D$  is often hard to determine and, more important,  $\epsilon$  is not much smaller than 1. In fact, most parameter combinations result in values of  $\epsilon$  around 1, which is representative for dissipative beaches.

Nielsen (1990) already indicated that the analytical solution yields large discrepancies with field observations when a seepage face is present in the intertidal area. Comparison with field data showed an underestimation of the hydraulic heads by the analytical solution of up to 0.3 m, for a (small) tidal amplitude of 0.5 m and a (large) beach slope of 0.06. Because the overheight increases when the tidal amplitude increases and beach slope decreases, it is advised here that for comparable hydrogeological conditions as the ones considered in this study, the seepage face should be taken into account.

## 5.5 Summary and conclusions

The scope of this chapter was to provide a quantitative indication of the bias that is introduced in a groundwater flow model of an unconfined coastal aquifer if tides are neglected. Numerical, variable density groundwater flow and salt transport models were used to determine this bias for a wide range of hydrogeological conditions. Both a shallow and a deep aquifer were investigated with regard to three dimensionless parameter groups that determine the groundwater flow to a large extent. Analytical expressions were presented that allow for a quick estimate of the regional scale effect of tidal forcing under the same conditions as used in the numerical simulations.

The numerical model results indicated that the time-averaged hydraulic head at the high tide mark increases with a decrease of each of the three considered dimensionless parameter groups:  $R$  (the ratio of the hydraulic conductivity and the precipitation excess),  $\alpha$  (the slope of the intertidal area), and  $A_L$  (the ratio of the width of the freshwater lens and the tidal amplitude). The time-averaged hydraulic head at the high tide mark is little influenced by the flow of fresh groundwater from the hinterland. From the results of the numerical simulations, an empirical relationship was derived which can be used to estimate the time-averaged hydraulic head at the high tide mark from the slope of the intertidal area, the tidal amplitude and the hydraulic conductivity of the intertidal sediment. The time-averaged hydraulic head was used in analytical models as a boundary condition.

The relative change of the location and the hydraulic head of the groundwater divide, which were jointly referred to as 'regional scale overheight' and were used to characterize regional groundwater flow, increased as  $\alpha$  and  $A_L$  decreased, but decreased as  $R$  decreased. In case of a shallow aquifer, the time-averaged hydraulic head at the high tide mark was larger compared to a deep aquifer. However, the regional scale overheight was comparable. In case the controlled water level in the hinterland was larger than mean sea level, the regional scale overheight decreased.

The difference between the numerical model results of the deep and shallow aquifer and the corresponding analytical solutions was small. Therefore, the presented analytical solutions can be used to estimate the bias that is introduced in a numerical model if tidal forcing is neglected, for a wide range of hydrogeological conditions. However, one should be aware of the fact that this study has considered tidal forcing only. In case of significant wave action, the results in this chapter should be considered as conservative estimates.

## 5.6 Appendix

For  $[-A \leq z \leq A]$ , the position  $x$  in the intertidal area is defined as:

$$x = \frac{z}{\tan \alpha} \tag{5.24}$$

with  $z$  being the vertical coordinate (elevation relative to mean sea level) and  $\alpha$  the slope of the intertidal area. At mean sea level,  $z = 0$  and  $x = 0$ . In dimensionless form, whereby reference values are denoted by a subscript ( $_r$ ) and dimensionless quantities by  $'$ , equation 5.24 becomes:

$$\frac{x_r}{z_r} \tan \alpha = \frac{z'}{x'} \quad (5.25)$$

Choosing  $x_r$  and  $z_r$  as the already defined reference length  $L$ , the dimensionless group  $\tan \alpha$  appears.

A pressure ( $P_b(x, t)$ ) [ $M L^{-1} T^{-2}$ ] is prescribed for the surface of the intertidal area, as a function of position  $x$  and time  $t$ . When the sea level is lower than or equal to the elevation at point  $x$  in the intertidal area,  $P_b$  equals 0. In this way a seepage face is simulated (Mulligan et al., 2011). When the sea level is higher than the elevation at point  $x$  in the intertidal area, the pressure equals:

$$P_b(x, t) = A \sin(2\pi ft) \rho_{max} g - \rho g z(x) \quad (5.26)$$

where  $A$  is the tidal amplitude,  $f$  is the frequency, and  $g$  is the gravitational acceleration. If  $z$  is referenced to tidal amplitude  $A$  and both sides are divided by  $A \Delta \rho_{max} g$ , the Rayleigh number defined by Eeman et al. (2011) appears. After introduction of reference values, the left hand side of equation 5.26 becomes:

$$\frac{P_b}{A_r \Delta \rho_{max} g} \quad (5.27)$$

with  $P_b$  being equal to the reference pressure (Eeman et al., 2011):

$$\frac{\mu N L}{k} \quad (5.28)$$

whereby  $N$  is the recharge rate,  $k$  is the permeability of the porous medium and  $\mu$  is the viscosity of freshwater. The left hand side becomes:

$$\frac{\mu N L}{k A_r \Delta \rho_{max} g} \quad (5.29)$$

which equals:

$$\frac{L}{A_r R} \quad (5.30)$$

$R$  is the dimensionless Rayleigh number defined by Eeman et al. (2011) and the dimensionless group  $A_L$  appears.

If the definition for the reference time by Eeman et al. (2011) is adopted:

$$t_r = \frac{nL}{N} \quad (5.31)$$

the following dimensionless group appears from right hand side of equation 5.26:

$$f_{ps} = \frac{fLn}{N} \quad (5.32)$$

# Chapter 6

## Discussion

In Chapters 2 - 5, the four specific research questions that were formulated in the Introduction were addressed. The results of these chapters were discussed in view of related previous studies. However, the results were not, or only little, discussed in view of the two main objectives of this thesis. These objectives were:

1. To improve the insight into the modeling of freshwater lenses.
2. To define measures to increase freshwater supply from freshwater lenses.

In this final chapter the results of the previous four chapters are discussed in relation to these two objectives, as well as in a broader context.

### 6.1 Modeling of freshwater lenses

#### 6.1.1 Application of groundwater models

In previous studies of freshwater lenses and coastal aquifers in general, groundwater models have been widely used for the quantification of groundwater flow and salt transport (Reilly and Goodman, 1985; Werner et al., 2013). In many of these studies, groundwater models were used for generic understanding of groundwater flow and salt transport processes (Henry, 1964; Elder, 1968; Wooding et al., 1997a,b). Such studies are indispensable for basic insights. However, in modern research it becomes more and more important to complement basic insights with their application to solve real world problems (Post, 2005; Hunt and Doherty, 2011). In many in coastal areas, aquifers and freshwater resources are already under stress, and it is expected that this stress will increase tremendously in the future (Werner et al., 2013).

In applying groundwater models to real world cases, numerical models are more often used than analytical models, as numerical models are generally better at representing field conditions. In many studies, numerical models have been

been successfully used to reproduce fresh-saline groundwater dynamics (e.g., (Li et al., 2009; De Louw et al., 2013a; Heiss and Michael, 2014; Zuurbier et al., 2014b)), yielding quantitative insights of processes at site. However, complex models can be misleading, even in case of abundant data, because conceptualizing and parameterizing the subsurface in the model is always a deficient representation of reality (Voss, 2011a). For example, in Chapter 3 a rather complex numerical model was used to simulate groundwater flow and salt transport below a creek ridge. This model did not incorporate the heterogeneity that was inferred from the cone penetration tests, which appeared to locally influence the increase of the freshwater lens. On the other hand, the level of complexity that was used in the model was appropriate to simulate the general groundwater salinity dynamics at the field site.

The numerical model that was described in Chapter 3 had a long simulation time, which is typical for complex numerical models of coastal aquifers (Carrera et al., 2009). Long simulation times restrict extensive model calibration and parameter sensitivity analyses. Consequently, the uncertainty assessment of complex models is often limited. Model uncertainty amongst others involves conceptual uncertainties (Carrera, 1993; Delsman et al., 2013) and parameter uncertainties (De Marsily et al., 2005; Haitjema, 2006). Considering the latter, in saltwater intrusion studies the choice of the initial conditions (i.e., the groundwater salinity distribution (Faneca Sánchez et al., 2012; Delsman et al., 2014)) and the boundary conditions is often very important. Overviews of the difficulties in applying a model to a field situation and dealing with uncertainty can amongst others be found in Anderson and Woessner (2002) and Zheng and Bennett (2002).

As an alternative for complex models, many studies have described the advantages of using more simple models, which represent the system in a simple way, but adequate enough to capture the features that are essential for the model purpose (Konikow, 2010; Voss, 2011b). Simple models are relatively easy to understand, and computationally efficient. The analytical solutions presented in Chapter 4 are examples of simple models. These analytical solutions could under certain conditions can be used as an appropriate and computationally efficient tool to estimate the saltwater upconing of a horizontal well in a freshwater lens. Field data play an important role in such models in validating the assumptions that are made for the simplifications.

A simple model requires many assumptions, for example on the initial and boundary conditions, the hydrogeology and the grid resolution. As was shown in Chapter 5, it is important that such assumptions are quantitatively supported. This does not always require numerical modeling; in many cases quantitative insight can be obtained by using simple analytical solutions, such as using a characteristic leakage length for determining the boundary of a numerical model (Haitjema, 2006).

Assumptions and computational limitations are also aspects that have to be dealt with in regional scale investigations, such as was described in Chapter 2. When applying a low grid resolution in a numerical model of an area with a dense

drainage network in a confining layer, it cannot be assumed that the hydraulic resistance to groundwater-surface water is restricted to the hydraulic resistance of the surface water bed. If this is nevertheless assumed, serious errors in the estimation of fluxes or errors in model calibration can be expected.

In Chapters 2 and 5, improved groundwater model insights were presented. These improved insights are illustrated in the next two sections using two examples.

## 6.1.2 Examples of improved insights

### Chapter 2

In the introduction of Chapter 2, an example of a cross-sectional model of thin rainwater lenses (recall Figure 2.1) was given. It was shown that when the conductance for the drains and ditches in the model with a low grid resolution was based on the classical method of McDonald and Harbaugh (1988), the resistance to groundwater-surface water interaction was tremendously underestimated. Consequently, the upward flow of saline groundwater was overestimated, which had important implications for the quantification of water fluxes and salt loads to the surface water system.

However, little attention was given to the implications of the overestimation of the upward flux of saline groundwater regarding the estimation of the thickness of the thin rainwater lenses. For the estimation of the thickness of the thin rainwater lenses, the upward flux from the low grid resolution model can be used as a boundary condition for a more detailed model (downscaling), which can be used to determine the thickness of the thin rainwater lenses. Eeman et al. (2011) and De Louw et al. (2011) also used such detailed models in their investigations of thin rainwater lenses.

Here, for illustration purpose, the upward flux from the low-resolution model of the example in the introduction of Chapter 2 is used in combination with a downscaled model to estimate the thickness of the thin rainwater lens. The analytical solution of Maas (2007) is used as a downscaled model. This analytical solution is based on the interface approach (Chapter 4). The analytical solution of Maas (2007) requires the hydraulic conductivity ( $K$ ), groundwater recharge ( $N$ ), drain distance ( $L_{dr}$ ), the densities of the fresh and saline groundwater ( $\rho_f$  and  $\rho_s$ ) and the upward (saline) groundwater flow rate ( $S$ ) as input parameters for estimating the thickness of the rainwater lens. These parameters can all be taken from the model of Figure 2.1, i.e.,  $K = 0.01 \text{ m d}^{-1}$ ,  $N = 0.0003 \text{ m d}^{-1}$ ,  $L_{dr} = 10 \text{ m}$ ,  $\rho_f = 1000 \text{ kg m}^{-3}$  and  $\rho_s = 1025 \text{ kg m}^{-3}$ .  $S$  is taken as the specific discharge towards the drain in the model with a low grid resolution, and therefore depends on which kind of conductance method is used. The two conductance methods that were used in the example (the conductance methods of McDonald and Harbaugh (1988) and De Lange (1999); see Figure 2.9) are used here, and  $S$  is taken from these two models with a low grid resolution.

In Figure 6.1, it is shown that the analytical solution of Maas (2007) nicely

resembles the thickness of the rainwater lens (approximated as 50% of the maximum standardized concentration in the model) in the reference example, when  $S$  is taken from the low grid resolution model using the conductance expression of De Lange (1999). Eeman et al. (2011) also showed nice comparisons between their numerical models and the analytical solution of Maas (2007), which indicates that  $S$  was appropriate. In contrast, in case the conductance method of McDonald and Harbaugh (1988) is used, there is no flux towards the drains, as all water is discharged by the ditches. In case the upward flow towards the ditches is taken as representative flux for  $S$ , the thickness of the lens is greatly underestimated.

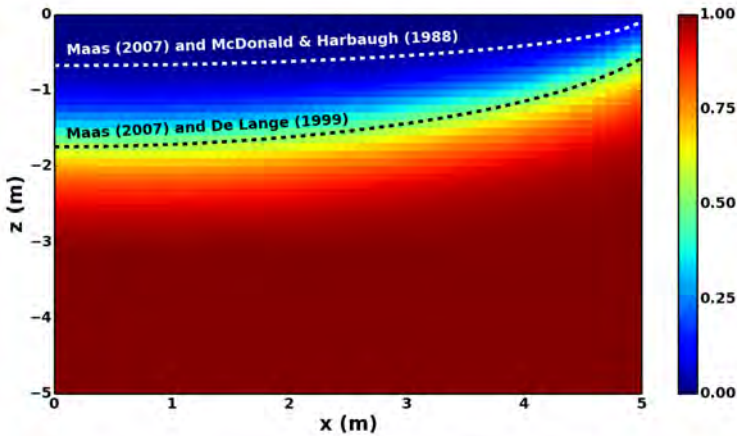


Figure 6.1: Scaled concentrations (shown in color, from 0 (minimum concentration) - 1 (maximum concentration)) of the model with a high resolution at  $x = 480 - 485$  m of the example of the introduction of Chapter 2. The black and white dashed lines indicate the estimated thickness of the freshwater lens using the analytical solutions of Maas (2007) when  $S$  is taken from the upscaled model using the conductance expressions of (De Lange, 1999) and McDonald and Harbaugh (1988), respectively. The drain tile is located at  $x = 5$  m.

This example shows that, in theory, a regional scale investigation of the thickness of shallow rainwater lenses can be made by combining a regional scale groundwater model using the conductance expression of De Lange (1999) in conjunction with the downscaled of Maas (2007). In practice, however, many complexities introduce uncertainty in this approach. For example, the thickness of the thin rainwater lens shows seasonal variation (De Louw et al., 2013a), and mixing processes in the unsaturated zone likely influence the salinity of the groundwater recharge (De Louw, 2013), which both pose questions to the appropriateness of the analytical solution of Maas (2007). Nevertheless, it is evident that the conductance expression of De Lange (1999) leads to a much better estimate of the flux of upward flowing saline groundwater compared to classical expressions for the

conductance, and therefore a better boundary condition for downscaled models.

## Chapter 5

This example considers a groundwater flow model of a freshwater lens in an unconfined coastal aquifer, with the key parameters as shown in Figure 6.2. The freshwater lens is bordered at the land-ocean boundary by an intertidal area, and the groundwater flow is influenced by tides. In Chapter 5, it was described that under these conditions, tides influence the time-averaged hydraulic heads near the shore and that under certain conditions this effect can also have an important influence further inland.

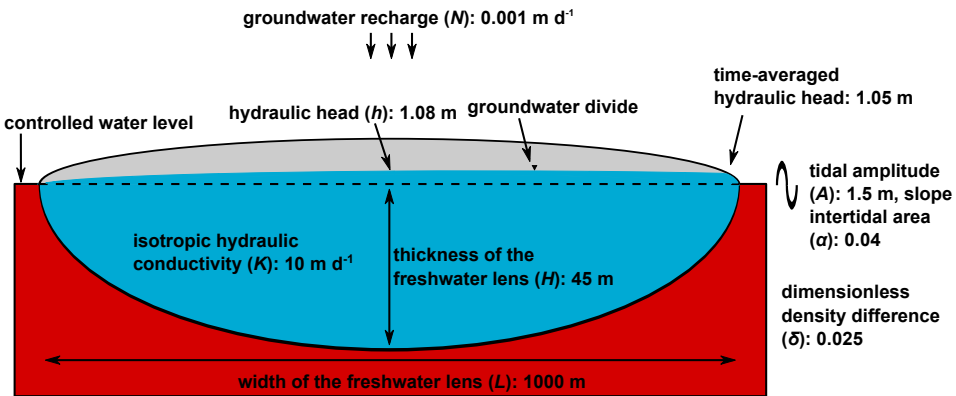


Figure 6.2: Concept of a freshwater lens subjected to tides in a homogeneous aquifer.

In case the tidal effect is neglected in the model, the groundwater divide will be exactly halfway the freshwater lens ( $0.5L$ ). The hydraulic head at this location can be calculated using Equation 5.11<sup>1</sup> using  $N = 0.001 \text{ m d}^{-1}$ ,  $K = 10.0 \text{ m d}^{-1}$ ,  $L = 1000 \text{ m}$  and  $\delta = 0.025$ , which results in  $0.78 \text{ m}$ . Equation 5.17 using  $A = 1.5 \text{ m}$  and  $\alpha = 0.04$  indicates that the tides have a significant effect on the time-averaged hydraulic head at the high tide mark ( $1.05 \text{ m}$ ). Furthermore, Equation 5.11 shows that at the location  $0.5L$ , the hydraulic head ( $1.08 \text{ m}$ ) caused by these tidal conditions is also significantly higher ( $0.3 \text{ m}$ ) compared to a situation with a static mean sea level. Moreover, the freshwater lens is  $12 \text{ m}$  thicker.

Now, suppose that field data is available to calibrate the model, then ignoring the effect of tides in the model calibration results in erroneous estimation of other parameters. For example,  $K$  should be decreased with a factor of 2 or  $N$  should be increased by a factor of 2 to yield an hydraulic head of  $1.08 \text{ m}$  at the location  $0.5L$ . Such erroneous model parameters may then influence other model outcomes, such as quantifying saltwater intrusion rates (Watson et al., 2010; Webb and Howard,

<sup>1</sup>That is, by adopting the assumptions underlying this equation

2011) or free convection of seawater as a result of marine inundations (Gingerich and Voss, 2014).

Although this example is simple and idealized, it does indicate the importance of quantitative support when doing assumptions in models, even when data is available for calibration.

## 6.2 Measures to increase freshwater supply

### 6.2.1 Example of improved insight

In Chapter 3 the potential of a Controlled Artificial Recharge and Drainage (CARD) system for increasing a freshwater lens below a creek ridge was described. The increase of the freshwater lens was realized by increasing the groundwater table in winter, when there is a precipitation excess. It was briefly described in Chapter 3 that from thicker freshwater lenses more fresh groundwater can be extracted compared to thinner freshwater lenses. From the analytical solutions of Dagan and Bear (1968) that were described in Chapter 4, it can be deduced that this is mainly because in thicker freshwater lenses the distance between the depth of the well and the bottom of the freshwater lens is larger than in thinner freshwater lenses.

The analytical solutions of Dagan and Bear (1968) can also be used to conveniently estimate the extra amount of fresh groundwater that can be extracted as a function of the increase of the freshwater lens. For illustration purpose, the increase of the freshwater below the creek ridge at measurement location 1 (Chapter 3) is considered here. Before the installation of the CARD system, the thickness of the freshwater lens was about 13 m at measurement location 1. In case a horizontal well at a distance of 5 m above the bottom of the freshwater lens is present, application of Equation 4.4 using a porosity of 0.38, a horizontal hydraulic conductivity of  $7.0 \text{ m d}^{-1}$ , a vertical hydraulic conductivity of  $7.0 \text{ m d}^{-1}$ , and a relative density difference of 0.0223, indicates that in case of steady pumping for a period of 180 days the maximum pumping rate<sup>2</sup> is  $0.27 \text{ m}^3\text{d}^{-1}$  per unit length of the horizontal well. In Figure 6.3, it is shown how this maximum pumping rate approximately linearly increases with the increase of the freshwater lens. If the lens at measurement location 1 is increased by 4.5 m, about twice as much water can be extracted.

---

<sup>2</sup>The maximum pumping rate is when the dimensionless interface upconing using the equation of Dagan and Bear (1968) is equal to 0.25, based on the results of Chapter 4.

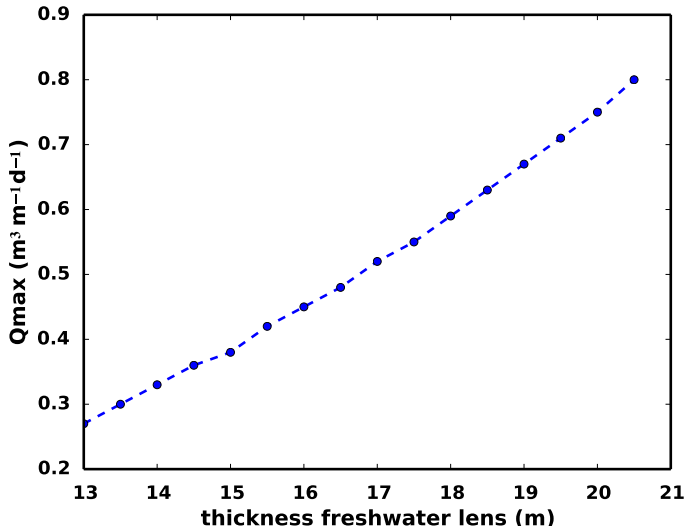


Figure 6.3: Illustrative example on increasing freshwater supply from freshwater lenses below creek ridges using artificial infiltration via the CARD system and recovery using horizontal wells.

As was described in Chapters 3 and 4 further research is needed for better understanding of the long-term effects of the artificial infiltration using the CARD system and the long-term effects of saltwater upconing. Nevertheless, the results of Figure 6.3 indicate the potential of increasing freshwater supply by artificial recharge below creek ridges using the CARD system and recovery using horizontal wells.

### 6.2.2 Additional insights

Although artificial recharge has been applied for decades in many coastal areas (Lebbe, 1978; Stuyfzand, 1993; Bouwer, 2002), the CARD system and its application to a creek ridge have not been described before. Furthermore, in Chapter 3, the negative effect of ditches that cut through creek ridges regarding the thickness of the freshwater lenses was discussed. Visser (2012) showed that removing such a ditch can lead to a significant increase of the freshwater lens. Similar conclusions were drawn by Langevin et al. (1998), in their study on the effect of canals on the freshwater lens below Big Pine Key, an island located in the southern part of Florida Keys, USA. Drainage of freshwater lenses below creek ridges should therefore be prevented as much as possible, without losing track of their main functions (e.g., preventing flooding and undesired high surface water levels).

Regarding the results of Chapter 4, perhaps the most apparent result is that the numerical model and the analytical solutions nicely compare with the numer-

ical simulations in many situations that were investigated (e.g., cyclic pumping), provided that the saltwater upconing remains limited. This is a valuable insight, as it enables a fast computation of the safe yield of (horizontal) wells. The relative short computation time can help in investigations to better determine the uncertainties in the model (section 6.1.1) or better determine the most optimal configuration of (horizontal) wells, for example using an optimization modeling procedure (Das and Batta, 2000; Kourakos and Mantoglou, 2009).

### **6.3 Recommendations for future studies**

The results that have been presented in Chapters 2 - 5 have increased the insights into the modeling of freshwater lenses, as well as into measures to increase freshwater supply from freshwater lenses. However, various challenges remain for further research.

Although the conductance expression of De Lange (1999) (Chapter 2) has proven its potential for a wide range of conditions, its applicability in case of other conditions needs to be investigated, for example, its use in case of a heterogeneous confining layer, deeper (partial) penetration of the surface water features in the confining layer, irregularly distributed surface waters (3D models) and various horizontal grid resolutions. Regarding thin rainwater lenses, it is recommended to continue research on on adaptive drainage systems to increase their thickness. Research on adaptive drainage systems is currently carried out in the southwestern part of the Netherlands, within the project Drains2Buffer (Oude Essink et al., 2014). The basic idea behind the adaptive drainage system is that in times of precipitation excess when drainage is needed, the saline groundwater is drained rather than the fresh groundwater. Conclusive results on the feasibility of this measure can be expected at the end of 2017.

As was described in Chapter 3, a disadvantage of the three-dimensional numerical model that was used to investigate the effect of the CARD system is the long simulation time. For investigating the potential of the CARD system elsewhere, it is recommended to develop a model with a much shorter runtime. Using such a model, effects of fresh surface water availability and the hydrogeology, as well as parameter uncertainty can be better quantified. Regarding the future investigation of the CARD system in the field, it is advised to continue the monitoring of the groundwater levels and groundwater salinity distribution to determine the long term effects of the measure.

In Chapter 4, analytical solutions based on the interface approach were used to quantify saltwater upconing. Although guidelines for the safe yield (i.e., when the salinity of the extracted water remains sufficiently low) on the short term (i.e., a year) were provided for a large range of conditions, the safe yield on the longer term was not determined. This long-term aspect would be a useful topic for future research. In addition, it is also recommended to develop cheap and effective monitoring systems that allow users (e.g., farmers) to keep track of the saltwater upconing due to pumping from freshwater lenses.

Regarding the simulation of the influence of tides on groundwater flow below the intertidal area (Chapter 4) using SEAWAT (Langevin et al., 2007), it is advised to develop a new version of SEAWAT that is better capable of simulating periodic groundwater flow. The MODFLOW version of Niswonger et al. (2011) is already available for a robust simulation of periodic flow.

A recommendation related to all four chapters of this thesis is on numerical models. Currently, the application of such models in (real) coastal aquifers is amongst others still seriously hampered by computational effort. For a better quantification of fresh groundwater resources in coastal areas, future research should pay attention to improving the computational efficiency of these numerical models (Langevin and Panday, 2012).

Last but not least, for practical hydrogeological research it is recommended to stimulate the collaboration between practical oriented professionals and theoretical oriented researchers (Hunt and Doherty, 2011).



# Chapter 7

## English summary

Freshwater lenses are convex bodies of fresh groundwater that are underlain by groundwater with a significant higher salinity. In coastal areas, freshwater lenses are of vital importance for ecosystems and freshwater supply. A major problem of sustaining freshwater supply from freshwater lens is saltwater intrusion, i.e., the invasion of saline groundwater into a fresh groundwater body. In many coastal areas saltwater intrusion has led to well closure and reduced freshwater supply. Furthermore, in the future saltwater intrusion is expected to increase due to sea level rise, climate change, land subsidence, and increasing population density in coastal areas.

In the Netherlands, these stresses will also have a severe impact on the fresh coastal groundwater reserves. In view of this, a research project within the Dutch research program 'Knowledge for Climate' was defined in 2010, aimed at:

1. Improving the insight into the modeling of freshwater lenses.
2. Defining measures to increase freshwater supply from freshwater lenses.

In Chapters 2-5 of this thesis, the results four studies related to these objectives are presented.

### Chapter 2

The study described in Chapter 2 is related to thin rainwater lenses. Thin rainwater lenses are found in low-lying areas where the upward flow of brackish or saline groundwater limits the downward flow of the groundwater recharge. The thickness of thin rainwater lenses is important to study, as vegetation that depends on the limited amount of freshwater is at risk by a high salinity in the root zone. An important driver for the thickness of the thin rainwater lens is the upward flow of saline groundwater. In case regional scale models are used to quantify the upward flow of saline groundwater, it is important that the groundwater-surface water interaction (GW-SW) is properly simulated. However, quantitative guidelines for

simulating GW-SW interaction in regional scale models appear to be missing in literature.

It was shown in Chapter 2 that the classical method for simulating GW-SW interaction of McDonald and Harbaugh (1988) leads to serious errors. Furthermore, it was shown that the overlooked method of De Lange (1999) leads to much better simulation of GW-SW interaction, and that the influence of variable groundwater density flow, vertical grid discretization and simulation of both ditches and drain tiles on the accuracy of the method of De Lange (1999) was minor. In the discussion chapter of this thesis, it was shown that the method of De Lange (1999) also leads to a much better estimation of the thickness of thin rainwater lens compared to the classical method of McDonald and Harbaugh (1988).

### **Chapter 3**

Freshwater lenses below creek ridges were considered in Chapter 3. Creek ridges are typical geomorphological features that lie up to 2 meters higher than the surroundings in the polders of the southwestern part of the Netherlands. Below the creek ridges freshwater lenses are present with a maximum thickness between 5 and 30 meters, depending mainly on the drainage (i.e., ditches and drain tiles) and the width of the creek ridge. The freshwater lenses are exploited for irrigation, but at many places the permissible rate and amount of fresh groundwater extraction is insufficient to meet the irrigation demand during droughts, which leads to freshwater scarcity and, hence, crop damage.

For increasing freshwater supply, a new Controlled Artificial Recharge and Drainage system for increasing a freshwater lens below creek ridges was investigated. The CARD system is used for artificial recharge below the higher parts of the creek ridge and for keeping the groundwater level below the lower parts as well as higher parts of the creek ridge as high as possible. The CARD system was tested on a creek ridge in the southwestern part of the Netherlands. Field data was collected during a 1.5 year period and was used in combination with numerical models to investigate the CARD system. The numerical simulations reasonably reproduced the field measurements, and indicated that over a period of 10 years, the 10-15 meters thick freshwater lens below the creek ridge can increase up to 10 meters. It is expected that the most important factors that influence the effect of the CARD system on the increase of the freshwater lens are low permeable layers, the drainage resistance, the water availability for artificial recharge and the thickness of the unsaturated zone to accommodate the increase of the groundwater table.

### **Chapter 4**

The exploitation of freshwater lenses using horizontal wells was considered in Chapter 4. New insights in using analytical solutions for calculating saltwater upconing below horizontal wells in freshwater lenses were presented, i.e., 1) cyclic pumping, 2) dispersion, and 3) finite horizontal wells in a finite domain

(a freshwater lens). The accuracy of the analytical calculations regarding these three aspects was determined by comparison with numerical simulations. A major advantage of analytical solutions over numerical models is the much shorter computation time.

The results of Chapter 4 indicated that regarding cyclic pumping, the accuracy of the analytical calculations of the interface depth were little influenced by the storage parameters and closely resembled all numerical simulations as long as the dimensionless interface upconing was below  $1/3$ . Accounting for mixing below the well using an analytical solution was accurate in case the vertical flow velocity around the interface was nearly constant, but inaccurate for estimating the salinity of the pumped groundwater. The analytical calculation of interface upconing below a finite horizontal well was accurate in case the distance below the horizontal well and the initial interface in the freshwater lens did not vary, and in case the natural fluctuation of the freshwater lens was small. For a low salinity in the well in case of cyclic pumping, it is advised to keep the dimensionless analytically calculated interface upconing below 0.25. In the discussion chapter of this thesis, the combined insights of Chapters 3 and 4 were shown.

## **Chapter 5**

In Chapter 5, the impact of tidal forcing on regional groundwater flow in an freshwater lens in an unconfined coastal aquifer was considered. Numerical models were used to quantify this impact for a wide range of hydrogeological conditions. Both a shallow and a deep aquifer were investigated with regard to three dimensionless parameter groups that determined the groundwater flow to a large extent. Analytical expressions were presented that allow for a quick estimate of the regional scale effect of tidal forcing under the same conditions as used in the numerical models.

The results indicated that the difference between the analytical solutions and numerical results were small. Therefore, the presented analytical solutions can be used to estimate the bias that is introduced in a numerical model if tidal forcing is neglected. In the discussion chapter of this thesis, the added value for this bias estimation was described in view of parameter estimation.



# Dank- en nawoord

Zo'n zes jaar geleden, voordat ik aan mijn afstudeeronderzoek aan de Vrije Universiteit Amsterdam begon, had ik geen interesse om verder te gaan in de wetenschap. Mijn mening veranderde tijdens mijn afstudeeronderzoek op het strand van Castricum, waar ik gefascineerd raakte door de interactie tussen zoet en zout grondwater. Het verzamelen van verschillende soorten gegevens, het vastbijten in de data en theorie en het proberen te begrijpen van het grondwatersysteem bij de kust bracht veel voldoening en werkte bovendien verslavend. Nadat ik was afgestudeerd vroeg ik een van mijn toenmalige begeleiders (Vincent Post) om advies, omdat ik een baan wilde met ruimte voor inhoudelijke diepgang. Vincent raadde me aan eens te gaan praten bij Deltares, met Gu Oude Essink. Van het een kwam het ander, en ongeveer een half jaar na mijn afstuderen begon ik bij Deltares en de Universiteit Wageningen (WUR) aan mijn promotie-onderzoek binnen het Kennis voor Klimaat (KvK) Programma.

Dit promotieonderzoek duurde ruim vier jaar. Ik heb dit als een zeer prettige en leerzame periode ervaren. Ik ben de verschillende partijen en leden van het consortium 'Climate Proof Fresh Water Supply' (KvK Programma), in het bijzonder Deltares en de WUR, dankbaar voor het mogelijk maken van dit onderzoek. Zoals bij veel promovendi ging het onderzoek niet vanzelf. Ik heb steun gehad van een groot aantal mensen. Mijn drie begeleiders hebben aan de basis van mijn onderzoek en het afronden van dit proefschrift gestaan. Ik wil jullie alle drie met name bedanken voor het vertrouwen dat jullie in mij hebben getoond. Sjoerd, jij stond als promotor altijd voor me klaar. Bedankt voor de talloze inhoudelijke discussies, jouw snelle commentaar op mijn concept artikelen en jouw geduld wanneer ik weer eens met glazige ogen naar vergelijkingen aan het kijken was. Gu, jij leerde mij als co-promotor bij Deltares vele dingen; van numeriek modeleren en figuren maken tot presenteren en projectmatig werken. Jouw enthousiasme omtrent 'zoet-zout' is onbegrensd en aanstekelijk. Verder heb ik genoten van, en gelachen om, de vele gesprekken die niet gerelateerd waren aan werk. Toon, jij was als co-promotor bij de WUR altijd in staat om mijn soms warrige bevindingen kort en duidelijk samen te vatten. Ik wil je bedanken voor de heldere uitleg tijdens de vele discussies in Wageningen en Utrecht, jouw scherpe blik op resultaten en jouw nuttige suggesties tijdens mijn onderzoek.

Naast mijn begeleiders heb ik ook veel steun gehad van mijn collega's bij

Deltares, in het bijzonder van de afdeling Grondwaterbeheer. Zonder anderen tekort te doen, noem ik een aantal hier apart. Joost, jij was als AIO binnen hetzelfde werkpakket nauw betrokken bij mijn onderzoek. Ik heb prettig met je samengewerkt en gediscussieerd, en veel van jouw geleerd, o.a. Python, numeriek opschalen en papers schrijven. Ik ben ook erg blij dat je hebt bijgedragen aan mijn tweede paper en dat jij een van mijn paranimfen wilde zijn. Esther, jij was ook een zeer fijne en competente collega. Jouw drive was vaak ongekend, en ik heb het samenwerken met jou, vooral het werk dat beschreven staat in hoofdstuk 3, als zeer prettig en leerzaam ervaren. Perry, jouw onderzoek was nog gaande toen ik begon. Ook van jou heb ik veel geleerd. Ik wil je bedanken voor jouw scherpe blik op mijn resultaten en de vele inhoudelijke discussie die wij hebben gevoerd. Jarno, onze discussies over numerieke modellen waren altijd interessant en vaak grappig, dank daarvoor. Ik vind dat jij promoveren serieus moet overwegen. Wim en Jacco, dank voor jullie inhoudelijke discussies over opschaling (hoofdstuk 2). Wijb: ook discussiëren met jou was altijd leuk en interessant, en ik ben erg blij dat jij een van mijn paranimfen wilde zijn. Rein, Pieter en Mike, ik wil jullie bedanken voor de ondersteuning van het veldwerk (hoofdstuk 3).

In Wageningen heb ik altijd heerlijk rustig kunnen werken. Hennie, Harm, Piet, Bram en Dieuwke, dank voor jullie prettige gezelschap. Annelies, jij stond altijd klaar als ik een vraag had, dank daarvoor.

Ik heb vier studenten begeleid, die allen zeer nuttig werk hebben verricht. Martijn, jij was bijzonder snel en scherp met het maken van het model dat de basis is geweest voor het model dat beschreven staat in hoofdstuk 3. Ik wil je bedanken hiervoor, en ik ben blij dat jij co-auteur bent geworden van het artikel. Maitri, jij werkte prima samen met Martijn, en hebt uiteindelijk ook een mooi model kunnen maken om het grondwatersysteem rondom het gebied van de Waterhouderij beter te begrijpen. Marjan en Thomas, ook jullie wil ik bedanken voor het verzamelen van gegevens in het veld, analyseren van de data en het maken van modellen. Gerben Willems, ook al begeleidde ik jou niet, toch wil ik ook jou bedanken voor de inhoudelijke discussies over opschaling (hoofdstuk 2).

Velen waren betrokken bij de infiltratieproef op de kreekrug (hoofdstuk 3). Ik wil alle leden van de Waterhouderij, in bijzonder Werner Louwerse en Johan Sanderse, bedanken voor hun tijd, energie, hulp maar vooral ook hun enthousiasme rondom de proef. Ik vind de Waterhouderij een prachtige samenwerking, en ik ben er van overtuigd dat dit op veel andere plekken ook kan leiden tot een flinke verbetering m.b.t. (zoet)waterbeheer. Ik dank meneer Rutten voor zijn tijd en energie en fantastische werk bij de aanleg van de drainage. Peter Meeuwse, dank voor de aanleg van de pompinstallatie. Lodewijk Stuyt, dank voor het sparren over de infiltratieproef. Ik dank Imageau en Fugro voor het verzorgen van de SMD metingen en de geleidbaarheidsonderingen. De Provincie Zeeland (Vincent Klap en Andre van der Straat) en Waterschap Scheldestromen (Acronius Kramer en Rene Geschiere) hebben een groot aandeel gehad in het mogelijk maken van de proef, dank daarvoor!

Het werk dat beschreven staat in hoofdstuk 5 vloeit voort uit mijn afstudeerw-

erk. Vincent, Koos en Michel, dank voor jullie bijdragen tijdens mijn afstudeerproject en jullie steun en tijd daarna, wat geleid heeft tot mijn eerste artikel. Het doet pijn om te zien hoe het bestuur van de VU de een na de andere onbegrijpelijke beslissing heeft gemaakt omtrent de Master Hydrology, waar jullie en jullie collega's uiteindelijk de dupe van zijn geworden. En dat terwijl de Master Hydrology aan de VU een internationaal zeer gewaardeerde opleiding is.

Alexander, ik wil jou ook bedanken voor jouw bijdrage aan hoofdstuk 5. Verder wil ik Arjen Kok, Frans Schaars, Igor Mendizabal, Sander de Haas en Harry Rolf bedanken voor het beschikbaar stellen van data gerelateerd aan dit hoofdstuk.

Ik wil de leescommissie, bestaande uit Prof. Dr J. Molenaar, Prof. Dr M.Th. van Genuchten, Prof. Dr S.M. Hassanizadeh en Prof. Dr. T.H. Olsthoorn bedanken voor het evalueren van mijn proefschrift. Verder wil ik de (vaak anonieme) reviewers van de vier papers van hoofdstukken 2 tot en met 5 bedanken voor hun commentaar. Dank ook aan de ontwikkelaars van het FloPy project, waar ik veel gebruik van heb gemaakt voor het maken en analyseren van mijn numerieke modellen.

Rest mij de mensen te bedanken die minder inhoudelijk betrokken waren bij mijn onderzoek, maar zeker niet minder belangrijk waren. Vrienden en familie, dank voor jullie frisse kijk op dingen en het aanhoren van mijn enthousiasme en (ook vaak) geklaag, zodat ik kon relativiseren en uiteindelijk niet ben verdrongen in mijn werk. Pa en ma, jullie hebben me vanaf het begin af aan fantastisch gesteund. Jullie zijn geweldige ouders. Maarten en Liselotte, ook jullie wil ik bedanken.

Marta, gràcies por tot el seu suport i amor. T'estimo.



# Bibliography

- Anderson, E.I., 2005. Modeling groundwater-surface water interactions using the Dupuit approximation. *Advances in Water Resources* 28, 4, 315–327.
- Anderson, M.P. and Woessner, W.W., 2002. *Applied groundwater modeling: simulation of flow and advective transport*. Academic Press, San Diego, California, USA.
- Archie, G.E., 1942. The electrical resistivity log as an aid in determining some reservoir characteristics. *Journal of Petroleum Technology* 5, 1–8.
- Ataie-Ashtiani, B., Volker, R. and Lockington, D., 1999. Tidal effects on sea water intrusion in unconfined aquifers. *Journal of Hydrology* 216, 1-2, 17–31.
- Ataie-Ashtiani, B., Ketabchi, H. and Rajabi, M.M., 2014. Optimal Management of a Freshwater Lens in a Small Island Using Surrogate Models and Evolutionary Algorithms, February, 339–354.
- Ataie-Ashtiani, B., Werner, A.D., Simmons, C.T., Morgan, L.K. and Lu, C., 2013. How important is the impact of land-surface inundation on seawater intrusion caused by sea-level rise? *Hydrogeology Journal* 21, 7, 1673–1677.
- Bakker, M., 2003. A Dupuit formulation for modeling seawater intrusion in regional aquifer systems. *Water Resources Research* 39, 5, 1–10.
- Bakker, M., Oude Essink, G.H.P. and Langevin, C.D., 2004. The rotating movement of three immiscible fluids a benchmark problem. *Journal of Hydrology* 287, 1-4, 270–278.
- Bakker, T., 1981. *Nederlandse Kustduinen: Geohydrologie*. Ph.D. thesis, PUDOC Wageningen.
- Barlow, P.M., Norton, G.A. and Groat, C., 2003. *Ground Water in Freshwater-Saltwater Environments of the Atlantic Coast*. Technical report, U.S. Department of the Interior.
- Barlow, P.M. and Reichard, E.G., 2009. Saltwater intrusion in coastal regions of North America. *Hydrogeology Journal* 18, 1, 247–260.
- Bear, J., Cheng, A.D., Sorek, S., Ouazar, D. and Herrera, I., 1999. *Seawater Intrusion in Coastal Aquifers. Concepts, Methods and Practices*. Kluwer Academic Publishers.
- Bear, J., 1972. *Dynamics of Fluids in Porous Media*. Dover Publications., New York.
- Bear, J. and Dagan, G., 1965. The relationship between solutions of flow problems

- in isotropic and anisotropic soils. *Journal of Hydrology* 3, 88–96.
- Belcher, H. and D'Itri, F., 1995. *Subirrigation and controlled drainage*. Lewis Publishers.
- Bierkens, M.F.P., 1994. *Complex confining layers: A stochastic analysis of hydraulic properties at various scales*. Ph.D. thesis, Utrecht University.
- Bouwer, H., 2002. Artificial recharge of groundwater: hydrogeology and engineering. *Hydrogeology Journal* 10, 1, 121–142.
- Bower, J.W., Motz, L.H. and Durden, D.W., 1999. Analytical solution for determining the critical condition of saltwater upconing in a leaky artesian aquifer. *Journal of Hydrology* 221, 43–54.
- Bruggeman, G., 1972. *Twee-dimensionale Stroming in Semi-spanningwater (Two-Dimensional Flow in a Semi-confined Aquifer) Appendix to Report De Groeve*. Technical report, National Institute for Water Supply, Leidschendam, The Netherlands.
- Carrera, J., 1993. An overview of uncertainties in modelling groundwater solute transport. *Journal of Contaminant Hydrology* 13, 23–48.
- Carrera, J., Hidalgo, J.J., Slooten, L.J. and Vázquez-Suñé, E., 2009. Computational and conceptual issues in the calibration of seawater intrusion models. *Hydrogeology Journal* 18, 1, 131–145.
- Cartwright, N., 2004. *Groundwater dynamics and the salinity structure in sandy beaches*. Ph.D. thesis, University of Queensland.
- Cobaner, M., Yurtal, R., Dogan, A. and Motz, L.H., 2012. Three dimensional simulation of seawater intrusion in coastal aquifers: A case study in the Goksu Deltaic Plain. *Journal of Hydrology* 464-465, 262–280.
- Custodio, E., 2009. Coastal aquifers of Europe: an overview. *Hydrogeology Journal* 18, 1, 269–280.
- Custodio, E. and Bruggeman, G., 1987. *Groundwater problems in coastal areas: a contribution to the International Hydrological Programme*. Studies and reports in hydrology. vol. 45. Paris.
- Dagan, G. and Bear, J., 1968. Solving The Problem Of Local Interface Upconing In A Coastal Aquifer By The Method Of Small Perturbations. *Journal of Hydraulic Research* 6, 1, 15–44.
- Dagan, G., Fiori, A. and Jankovic, I., 2013. Upscaling of flow in heterogeneous porous formations: Critical examination and issues of principle. *Advances in Water Resources* 51, 67–85.
- Das, A. and Batta, B., 2000. Optimization based solution of density dependent seawater intrusion in coastal aquifers. *Journal of Hydrologic Engineering* 5.
- Davis, S., 1978. Floation of fresh water on sea water, a historical note. *Ground water* 16, 6, 444–445.
- De Lange, W.J., 1996. *Groundwater modelling of large domains with analytic elements*. Ph.D. thesis, Delft, University of Technology.
- De Lange, W.J., 1998. On the errors involved with the parameterization of the MODFLOW river and drainage packages. In E. Poeter, Z. Zheng and M. Hill, editors, *MODFLOW98 Proceedings of the 3rd International Conference of the*

- International Ground Water Modeling, Vol. 1. Golden, Colorado.
- De Lange, W.J., 1999. A Cauchy boundary condition for the lumped interaction between an arbitrary number of surface waters and a regional aquifer. *Journal of Hydrology* 226, 3-4, 250–261.
- De Lange, W.J., Prinsen, G.F., Hoogewoud, J.C., Veldhuizen, A.A., Verkaik, J., Oude Essink, G.H.P., Van Walsum, P.E.V., Delsman, J.R., Hunink, J.C., Massop, H.T.L. and Kroon, T., 2014. An operational, multi-scale, multi-model system for consensus-based, integrated water management and policy analysis: The Netherlands Hydrological Instrument. *Environmental Modelling & Software* 59, 98–108.
- De Louw, P.G.B., 2013. Saline seepage in deltaic areas. Ph.D. thesis, VU University Amsterdam.
- De Louw, P.G.B., Eeman, S., Oude Essink, G.H.P., Vermue, E. and Post, V.E.A., 2013a. Rainwater lens dynamics and mixing between infiltrating rainwater and upward saline groundwater seepage beneath a tile-drained agricultural field. *Journal of Hydrology* 501, 133–145.
- De Louw, P.G.B., Eeman, S., Siemon, B., Voortman, B.R., Gunnink, J., Van Baaren, E.S. and Oude Essink, G.H.P., 2011. Shallow rainwater lenses in deltaic areas with saline seepage. *Hydrology and Earth System Sciences* 15, 12, 3659–3678.
- De Louw, P.G.B., Vandenbohede, A., Werner, A.D. and Oude Essink, G.H.P., 2013b. Natural saltwater upconing by preferential groundwater discharge through boils. *Journal of Hydrology* 490, 74–87.
- De Marsily, G., 1995. A Discussion on Upconing of Freshwater-Seawater Interfaces - Comment by an Editor. *Journal of Contaminant Hydrology* 18.
- De Marsily, G., Delay, F., Gonçalves, J., Renard, P., Teles, V. and Violette, S., 2005. Dealing with spatial heterogeneity. *Hydrogeology Journal* 13, 1, 161–183.
- Delsman, J.R., Hu-a ng, K.R.M., Vos, P.C., De Louw, P.G.B., Oude Essink, G.H.P., Stuyfzand, P.J. and Bierkens, M.F.P., 2014. Paleo-modeling of coastal saltwater intrusion during the Holocene: an application to the Netherlands. *Hydrology and Earth System Sciences* 18, 10, 3891–3905.
- Delsman, J.R., Oude Essink, G.H.P., Beven, K.J. and Stuyfzand, P.J., 2013. Uncertainty estimation of end-member mixing using generalized likelihood uncertainty estimation (GLUE), applied in a lowland catchment. *Water Resources Research* 49, 8, 4792–4806.
- Domenico, P. and Schwartz, F.W., 1990. *Physical and Chemical Hydrology*. John Wiley & Sons Ltd, New York.
- Drabbe, J. and Badon Ghijben, W., 1888. Nota in verband met de voorgenomen put boring nabij Amsterdam. *Tijdschrift Koninklijk Instituut voor Ingenieurs* 8–22.
- Du Commun, J., 1828. On the cause of fresh water springs, fountains, etc. *American Journal of Sciences* 14.
- Eeman, S., Leijnse, A., Raats, P.A.C. and Van der Zee, S.E.A.T.M., 2011. Analysis of the thickness of a fresh water lens and of the transition zone between this lens and upwelling saline water. *Advances in Water Resources* 34, 2, 291–302.

- Eeman, S., Van der Zee, S.E.A.T.M., Leijnse, A., De Louw, P.G.B. and Maas, C., 2012. Response to recharge variation of thin rainwater lenses and their mixing zone with underlying saline groundwater. *Hydrology and Earth System Sciences and Earth System Sciences* 16, 10, 3535–3549.
- Elder, J., 1968. The unstable thermal interface. *Journal of Fluid Mechanics* 32, 69–96.
- Ervinck, A., Beateman, C., Demiddelde, H., Hollevoet, Y., Pieters, M., Schelvis, J., Tys, D., Van Strydonk, M. and Verhaege, F., 1999. Human occupation because of regression, or the cause of a transgression? A critical review of the interaction between geological events and human occupation in the Belgian coastal plain during the first millenium AD. *Probleme der Kustenforsch im Sudlich Nordseegebiet* 26, 97–121.
- Essaid, H., 1986. A comparison of the coupled fresh water-salt water flow and the Ghyben-Herzberg sharp interface approaches to modeling of transient behavior in coastal aquifer systems. *Journal of Hydrology* 86, 1-2, 169–193.
- Faneca Sánchez, M., Gunnink, J.L., Van Baaren, E.S., Oude Essink, G.H.P., Siemon, B., Auken, E., Elderhorst, W. and De Louw, P.G.B., 2012. Modelling climate change effects on a Dutch coastal groundwater system using airborne electromagnetic measurements. *Hydrology and Earth System Sciences* 16, 12, 4499–4516.
- FAO, 1997. Seawater intrusion in coastal aquifers: guidelines for study, monitoring and control. *FAO Water Reports* 11. Rome Italy.
- Garabedian, S.P., 2013. Estimation of salt water upconing using a steady-state solution for partial completion of a pumped well. *Ground water* 51, 6, 927–34.
- Gelhar, L.W., Welty, W. and Rehfeldt, K., 1992. A critical review of data on field-scale dispersion of aquifers. *Water Resources Research* 28, 4, 1955–1974.
- Gingerich, S. and Voss, C.I., 2014. Sea-level rise and seawater inundation of an atoll island, Roi-Namur, Kwajalein Atoll, Republic of the Marshall Islands. In 23rd Salt Water Intrusion Meeting. Husum, Germany.
- Ginkel, M.V., Olsthoorn, T.N. and Bakker, M., 2014. A New Operational Paradigm for Small-Scale ASR in Saline Aquifers. *Groundwater* 52, 5.
- Goes, B.J.M., Oude Essink, G.H.P., Vernes, R.W. and Sergi, F., 2009. Estimating the depth of fresh and brackish groundwater in a predominantly saline region using geophysical and hydrological methods, Zeeland, the Netherlands. *Near Surface Geophysics* 401–412.
- Green, T.R., Taniguchi, M., Kooi, H., Gurdak, J.J., Allen, D.M., Hiscock, K.M., Treidel, H. and Aureli, A., 2011. Beneath the surface of global change: Impacts of climate change on groundwater. *Journal of Hydrology* 405, 3-4, 532–560.
- Haitjema, H., 2006. The role of hand calculations in ground water flow modeling. *Ground water* 44, 6, 786–91.
- Healy, R.W., 2010. *Estimating Groundwater Recharge*. Cambridge University Press.
- Heiss, J. and Michael, H.A., 2014. Saltwater-freshwater mixing dynamics in a sandy beach aquifer over tidal, spring-neap and seasonal cycles. *Water Re-*

- sources Research 50, 6747–6766.
- Henry, H., 1964. Effects of dispersion on salt encroachment in coastal aquifers. In H. Cooper jr., F. Kohout, H. Henry and R. Glover, editors, US Geological Survey Water Supply paper 1613-C.
- Herzberg, A., 1901. Die Wasserversorgung einiger Nordseebäder. *Gasbeleuchtung und Wasserversorgung* 44, 815–819.
- Hooghart, J. and Lablans, W., 1988. Van Penman naar Makkink: een nieuwe berekeningswijze voor de klimatologische verdampingsgetallen. Technisch rapport TR-111. Technical report, KNMI, De Bilt.
- Hooghoudt, S., 1940. General consideration of the problem of field drainage by parallel drains, ditches, watercourses and channels. In *Contribution to the Knowledge of Some Physical Parameters of the Soil*, Publ No. 7. Groningen, The Netherlands.
- Horn, D., 2006. Measurements and modelling of beach groundwater flow in the swash-zone: a review. *Continental Shelf Research* 26, 5, 622–652.
- Houben, G.J., Koeniger, P. and Sultenfuss, J., 2014. Freshwater lenses as archives of climate, groundwater recharge, and hydrochemical evolution: Insights from depth-specific water isotope analysis and age determination on the island of Langeoog, Germany. *Water Resources Research* 1–13.
- Hunt, R.J. and Doherty, J., 2011. Interesting or Important? Resetting the Balance of Theory and Application. *Ground water* .
- Hunt, R.J., Haitjema, H., Krohelski, J.T. and Feinstein, D.T., 2003. Simulating Ground Water-Lake Interactions: Approaches and Insights. *Groundwater* 41, 2, 227–237.
- ILRI, 1973. *Drainage Principles and Applications*. Technical report, International Institute for Land Reclamation and Improvement, Wageningen, The Netherlands.
- Jakovovic, D., Werner, A.D. and Simmons, C.T., 2011. Numerical modelling of saltwater up-coning: Comparison with experimental laboratory observations. *Journal of Hydrology* 402, 3-4, 261–273.
- Janković, I., Steward, D.R., Barnes, R.J. and Dagan, G., 2009. Is transverse macrodispersivity in three-dimensional groundwater transport equal to zero? A counterexample. *Water Resources Research* 45, 8, n/a–n/a.
- Kaleris, V., 2006. Submarine groundwater discharge: Effects of hydrogeology and of near shore surface water bodies. *Journal of Hydrology* 325, 1-4, 96–117.
- Kang, H., 1995. *Water Table Dynamics Forced by Waves*. Ph.D. thesis, University of Queensland.
- KNMI, 2015. Royal Netherlands Meteorological Institute.
- Konikow, L.F., 2010. The Secret to Successful Solute-Transport Modeling. *Groundwater* 1–16.
- Kooi, H. and Groen, J., 2001. Offshore continuation of coastal groundwater systems; predictions using sharp-interface approximations and variable-density flow modelling. *Journal of Hydrology* 246, 1-4, 19–35.
- Kooi, H. and Groen, J., 2003. Geological processes and the management of

- groundwater resources in coastal areas. *Journal Of Geosciences* 82, 1, 31–40.
- Kooi, H., Groen, J. and Leijnse, A., 2000. Modes of seawater intrusion during transgressions. *Water Resources Research* 36, 12, 3581.
- Kourakos, G. and Mantoglou, A., 2009. Pumping optimization of coastal aquifers based on evolutionary algorithms and surrogate modular neural network models. *Advances in Water Resources* 32, 4, 507–521.
- Krantz, D.E., Manheim, F.T., Bratton, J.F. and Phelan, D.J., 2004. Hydrogeologic Setting and Ground Water Flow Beneath a Section of Indian River Bay, Delaware. *Ground Water* 42, 7, 1035–1051.
- Kuan, W.K., Jin, G., Xin, P., Robinson, C., Gibbes, B. and Li, L., 2012. Tidal influence on seawater intrusion in unconfined coastal aquifers. *Water Resources Research* 48, 2, 1–11.
- Langevin, C.D., 2003. Simulation of submarine ground water discharge to a marine estuary: Biscayne Bay, Florida. *Ground water* 41, 6, 758–71.
- Langevin, C.D. and Panday, S., 2012. Future of groundwater modeling. *Ground water* 50, 3, 334–9.
- Langevin, C.D., Stewart, M. and Beaudoin, C., 1998. Effects of Sea Water Canals on Fresh Water Resources: An Example from Big Pine Key, Florida. *Ground Water* 36, 3, 503–513.
- Langevin, C.D., Thorne, D.T., Dausman, A.M., Sukop, M.C. and Guo, W., 2007. SEAWAT Version 4: A Computer Program for Simulation of Multi-Species Solute and Heat Transport: US Geological Survey Techniques and Methods Book 6, Chapter A22. Technical report.
- Langevin, C.D. and Zygnerski, M., 2013. Effect of sea-level rise on salt water intrusion near a coastal well field in southeastern Florida. *Ground water* 51, 5, 781–803.
- Langseth, D.E., Smyth, A.H. and May, J., 2004. A Method for Evaluating Horizontal Well Pumping Tests. *Groundwater* 42, 5, 689–699.
- Lebbe, L.C., 1978. Hydrogeologie van het duingebied ten westen van De Panne. Ph.D. thesis, Rijksuniversiteit Gent.
- Lebbe, L.C., 1983. Mathematical model of the evolution of the fresh water lens under the dunes and beach with semi-diurnal tides. In 8th Salt Water Intrusion Meeting, Bari, *Geologia Applicata e Idrogeologia*, volume XVIII, parte II, 211–226.
- Lebbe, L.C., 1999. Parameter identification in fresh-saltwater flow based on borehole resistivities and freshwater head data. *Advances in Water Resources* 22, 8.
- Li, X., Hu, B.X., Burnett, W.C., Santos, I.R. and Chanton, J.P., 2009. Submarine ground water discharge driven by tidal pumping in a heterogeneous aquifer. *Ground water* 47, 4, 558–68.
- Loke, M., Chambers, J. and Ogilvy, R., 2006. Inversion of 2D spectral induced polarization imaging data. *Geophysical Prospecting* 54, 3, 287–301.
- Lunne, T., Robertson, P. and Powell, J., 1997. Cone penetration testing in geotechnical practice. In *Cone penetration testing in geotechnical practice*, 312. Blackie

- Academic & Professional.
- Maas, E., 1990. Crop salt tolerance, American Society of Civil Engineers, Manuals and Reports on Engineering Practice. Technical report.
- Maas, E. and Hoffman, G., 1977. Crop salt tolerance - current assessment. *Journal of Irrigation and Drainage Division* 103, 115–134.
- Maas, K., 2007. Influence of climate change on a GhijbenHerzberg lens. *Journal of Hydrology* 347, 1-2, 223–228.
- Makkink, G., 1957. Testing the Penman formula by means of lysimeters. *Journal of Institution of Water Engineers* 11, 277–288.
- Masterson, J.P., 2004. Simulated Interaction Between Freshwater and Saltwater and Effects of Ground-Water Pumping and Sea-Level Change, Lower Cape Cod Aquifer System, Massachusetts. Technical report, US Geological Survey, Denver, Colorado, USA.
- McDonald, M. and Harbaugh, A., 1988. A Modular Three-Dimensional Finite-Difference Ground-Water Flow Model. US Geological Survey Techniques of Water-Resources Investigations, Book 6. Technical report, U.S. Geological Survey, Reston, Virginia.
- McNeill, J., 1980. Electromagnetic Terrain Conductivity at Low Induction Numbers, Geonics Ltd. Technical Note TN-6. Technical report, Geonics Ltd., Mississauga, Ontario, Canada.
- Mehl, S. and Hill, M.C., 2010. Grid-size dependence of Cauchy boundary conditions used to simulate stream-aquifer interactions. *Advances in Water Resources* 33, 4, 430–442.
- Miotlinski, K., Dillon, P., Pavelic, P., Barry, K. and Kremer, S., 2013. Recovery of Injected Freshwater from a Brackish Aquifer with a Multiwell System. *Groundwater* 54, 4, 495–502.
- Moody, W., 1966. Nonlinear differential equation of drain spacing. *Journal of Irrigation and Drainage Engineering* 92, 2, 1–10.
- Moore, W., 1996. Large groundwater inputs to coastal waters revealed by <sup>226</sup>Ra enrichments. *Nature* 380.
- Morel-Seytoux, H.J., 2009. The turning factor in the estimation of stream-aquifer seepage. *Ground water* 47, 2, 205–12.
- Morel-Seytoux, H.J., Mehl, S. and Morgado, K., 2014. Factors influencing the stream-aquifer flow exchange coefficient. *Ground water* 52, 5, 775–81.
- Motz, L.H., 1992. Salt-Water Upconing in an Aquifer Overlain by a Leaky Confining Bed. *Ground Water* 30, 2.
- Mulligan, A.E., Evans, R. and Lizarralde, D., 2007. The role of paleochannels in groundwater/seawater exchange. *Journal of Hydrology* 335, 3-4, 313–329.
- Mulligan, A.E., Langevin, C. and Post, V.E.a., 2011. Tidal boundary conditions in SEAWAT. *Ground water* 49, 6, 866–79.
- Nielsen, P., 1990. Tidal Dynamics of the Water Table in Beaches Beach. *Water Resources Research* 26, 9, 2127–2134.
- Nielsen, P., 1999. Groundwater dynamics and salinity in coastal barriers. *Journal of Coastal Research* 15, 3, 732–740.

- Niswonger, R.G., Panday, S. and Ibaraki, M., 2011. MODFLOW-NWT, A Newton formulation for MODFLOW-2005; US Geological Survey Techniques and Methods 6-A37. Technical report.
- Oude Essink, G.H.P., Van Baaren, E.S. and De Louw, P.G.B., 2010. Effects of climate change on coastal groundwater systems: A modeling study in the Netherlands. *Water Resources Research* 46, 10.
- Oude Essink, G.H.P., Van Baaren, E.S., Zuurbier, K.G., Velstra, J., Veraart, J., Brouwer, W., Faneca Sánchez, M., Pauw, P.S., Vreke, J. and Schroevers, M., 2014. GO-FRESH: Volarisatie kansrijke oplossingen voor robuuste zoetwatervoorziening, KvK rapport. Technical report.
- Oude Essink, G.H.P., 1996. Impact of Sea Level Rise on Groundwater Flow Regimes. A Sensitivity Analysis for the Netherlands. Ph.D. thesis, Delft University of Technology.
- Overeem, I. and Syvitski, J.P.M., 2009. Dynamics and Vulnerability of Delta Systems. 35. GKSS Research Center, Geesthacht, Germany.
- Pauw, P.S., De Louw, P.G.B. and Oude Essink, G.H.P., 2012. Groundwater salinisation in the Wadden Sea area of the Netherlands : quantifying the effects of climate change , sea-level rise and anthropogenic interferences. *Netherlands Journal of Geosciences* 91, 3.
- Pauw, P.S., Post, V.E.A., Groen, M.M.A. and Groen, J., 2009. The onshore and offshore groundwater salinity distribution between Egmond aan Zee and Catriicum aan Zee, MSc. thesis VU University Amsterdam. Technical report.
- Pauw, P.S., Van der Zee, S.E.A.T.M., Leijnse, A., Delsman, J.R., De Louw, P.G.B., De Lange, W.J. and Oude Essink, G.H.P., 2014. Low-Resolution Modeling of Dense Drainage Networks in Confining Layers. *Groundwater* .
- Philip, J., 1973. Period nonlinear diffusion: an integral relation and its physical consequences. *Australian Journal of Physics* 26, 513–519.
- Pool, M., Carrera, J., Dentz, M., Hidalgo, J.J. and Abarca, E., 2011. Vertical average for modeling seawater intrusion. *Water Resources Research* 47, 11, 1–12.
- Post, V.E.A., 2003. Groundwater salinization processes in the coastal area of the Netherlands due to transgressions during the Holocene. Ph.D. thesis, VU Amsterdam.
- Post, V.E.A., 2005. Fresh and saline groundwater interaction in coastal aquifers: Is our technology ready for the problems ahead? *Hydrogeology Journal* 13, 1, 120–123.
- Post, V.E.A., 2012. Electrical conductivity as a proxy for groundwater density in coastal aquifers. *Ground water* 50, 5, 785–92.
- Post, V.E.A., Groen, J., Kooi, H., Person, M., Ge, S. and Edmunds, M., 2013. Offshore fresh groundwater reserves as a global phenomenon. *Nature* 504, 71–78.
- Price, R.M., Top, Z., Happell, J.D. and Swart, P.K., 2003. Use of tritium and helium to define groundwater flow conditions in Everglades National Park. *Water Resources Research* 39, 9.
- Province of Zeeland, 2002. Samen omgaan met (grond)water (in Dutch). Technical report, Zierikzee.

- Pyne, R., 2005. Aquifer storage and recovery - a guide to groundwater recharge through wells. ASR Systems LLC, Gainesville, Florida, USA.
- REGIS, 2004. The Hydrogeological model of the Netherlands.
- Reilly, T.E., Franke, L. and Bennett, G.D., 1987a. The principle of superposition and its application in ground-water hydraulics. U.S. Geological Survey Techniques of Water- Resources Investigations Book 3, Chapter B6. Technical report, USGS.
- Reilly, T.E., Frimpter, M., LeBlanc, D. and Goodman, A.S., 1987b. Analysis of Steady-State Salt-Water Upconing with Application at Truro Well Field, Cape Cod, Massachusetts. *Groundwater* 25, 2.
- Reilly, T.E. and Goodman, A.S., 1985. Quantitative analysis of saltwater-freshwater relationships in groundwater systems-a historical perspective. *Journal of Hydrology* 80, 125–160.
- Reilly, T.E. and Goodman, A.S., 1987. Analysis of saltwater upconing beneath a pumping well. *Journal of Hydrology* 89, 169–204.
- Reis, A.H. and Gama, C., 2010. Sand size versus beachface slope An explanation based on the Constructal Law. *Geomorphology* 114, 3, 276–283.
- Renard, P. and de Marsily, G., 1997. Calculating equivalent permeability: a review. *Advances in Water Resources* 20, 5/6, 253–281.
- Reynolds, J.M., 1997. *Introduction to Applied and Environmental Geophysics*. John Wiley.
- Robinson, C., Gibbes, B. and Li, L., 2006. Driving mechanisms for groundwater flow and salt transport in a subterranean estuary. *Geophysical Research Letters* 33, 3, 3–6.
- Robinson, C., Li, L. and Barry, D., 2007. Effect of tidal forcing on a subterranean estuary. *Advances in Water Resources* 30, 4, 851–865.
- Ruppel, C., Schultz, G. and Kruse, S., 2000. Anomalous Fresh Water Lens Morphology on a Strip Barrier Island. *Groundwater* 38, 6, 872–881.
- Rushton, K., 2007. Representation in regional models of saturated riveraquifer interaction for gaining/losing rivers. *Journal of Hydrology* 334, 1-2, 262–281.
- Rushton, K. and Brassington, F., 2013. Significance of hydraulic head gradients within horizontal wells in unconfined aquifers of limited saturated thickness. *Journal of Hydrology* 492, 281–289.
- Schmorak, S. and Mercado, A., 1969. Upconing Fresh Water-Sea Water Interface Below Pumping. *Water Resources Research* 5, 6.
- Schneider, J.C. and Kruse, S.E., 2005. Assessing selected natural and anthropogenic impacts on freshwater lens morphology on small barrier Islands: Dog Island and St. George Island, Florida, USA. *Hydrogeology Journal* 14, 1-2, 131–145.
- Smiles, D. and Stokes, A., 1976. Periodic solutions of a nonlinear diffusion equation used in groundwater flow theory: Examination using a Hele-Shaw model. *Journal of Hydrology* 31, 27–35.
- Stafleu, J., Maljers, D., Gunnink, J.L., Menkovic, A. and Busschers, F.S., 2011. 3D modelling of the shallow subsurface of Zeeland, the Netherlands. *Netherlands*

- Journal of Geosciences 90, 4, 293–310.
- Stuyfzand, P.J., 1993. Hydrochemistry and Hydrology of the Coastal Dune area of the Western Netherlands. Ph.D. thesis, Vrije Universiteit Amsterdam.
- Stuyfzand, P.J., 1996. Salinization of drinking water in the Netherlands: anamnesis, diagnosis and remediation. In Proceedings of the 14th Salt Water Intrusion Meeting. Malmo, Sweden.
- Sulzbacher, H., Wiederhold, H., Siemon, B., Grinat, M., Igel, J., Burschil, T., Günther, T. and Hinsby, K., 2012. Numerical modelling of climate change impacts on freshwater lenses on the North Sea Island of Borkum using hydrological and geophysical methods. *Hydrology and Earth System Sciences* 16, 10, 3621–3643.
- Telford, W., Gelart, W. and Sheriff, R.E., 1990. Applied Geophysics. Cambridge University Press.
- Teo, H., Jeng, D., Seymour, B., Barry, D. and Li, L., 2003. A new analytical solution for water table fluctuations in coastal aquifers with sloping beaches. *Advances in Water Resources* 26, 12, 1239–1247.
- Thorn, P. and Urish, D., 2012. Preliminary Observation of Complex Salt-Fresh Water Mixing in a Beach Aquifer. *Ground water* 1–6.
- TNO, 1997. Holocene evolution of Zeeland (SW Netherlands). Mededelingen Nederlands Instituut voor Toegepaste Geowetenschappen TNO nr. 59. Technical report, Haarlem.
- Tredoux, G., Murray, E. and Cave, L., 2003. Infiltration Basins and Other Recharge System in South Africa. In: Management of Aquifer Recharge and Subsurface Storage. Netherlands Committee of IAH, Utrecht, The Netherlands.
- Turner, I.L., Coates, B.P. and Acworth, R., 1995. Tides, waves and the super-elevation of groundwater at the coast. *Journal of Coastal Research* 13, 1, 46–60.
- Urish, D.W. and Melih, M.O., 1989. The coastal ground-water boundary. *Ground Water* 27, 3, 310–315.
- Van Baaren, E.S., Oude Essink, G.H.P., Janssen, G.M.C.M., De Louw, P.G.B., Heerdink, R. and Goes, B., 2011. Freshening/salinization of phreatic groundwater in the province of Zeeland: Results of 3-D density dependent groundwater model. Deltares Report (in Dutch). Technical report, Deltares.
- Van Dam, J.C., 1983. The shape and position of the salt water wedge in coastal aquifers. In Proceedings of the Hamburg Symposium on Relation of Groundwater Quantity and Quality. IAHS 146, 59–75.
- Van der Veer, P., 1977. Analytical solution for steady interface flow in a coastal aquifer involving a phreatic surface with precipitation. *Journal of Hydrology* 34, 1–11.
- Van Meerten, J.J., 1986. Kunstmatige Infiltratie in Kreekruggen. Technical report, Technische Hogeschool Delft, Delft.
- Van Meir, N., 2001. Density-Dependent Groundwater Flow: Design of a Parameter Identification Test and 3D-Simulation of Sea-Level Rise. Ph.D. thesis, Ghent University.
- Vandenbohede, A. and Lebbe, L., 2002. Numerical modelling and hydrochemical

- characterisation of a fresh-water lens in the Belgian coastal plain. *Hydrogeology Journal* 10, 5, 576–586.
- Vandenbohede, A. and Lebbe, L., 2005. Occurrence of salt water above fresh water in dynamic equilibrium in a coastal groundwater flow system near De Panne, Belgium. *Hydrogeology Journal* 14, 4, 462–472.
- Vandenbohede, A. and Lebbe, L., 2006. Effects of tides on a sloping shore: groundwater dynamics and propagation of the tidal wave. *Hydrogeology Journal* 15, 4, 645–658.
- Vandenbohede, A., Luyten, K. and Lebbe, L., 2008. Effects of Global Change on Heterogeneous Coastal Aquifers: A Case Study in Belgium. *Journal of Coastal Research* 24, 160–170.
- Vermeulen, P.T.M., Te Stroet, C.B.M. and Heemink, A.W., 2006. Limitations to upscaling of groundwater flow models dominated by surface water interaction. *Water Resources Research* 42, 10, 1–12.
- Verruijt, A., 1968. a Note on the Ghyben-Herzberg Formula. *International Association of Scientific Hydrology. Bulletin* 13, 4, 43–46.
- Viezzoli, A., Tosi, L., Teatini, P. and Silvestri, S., 2010. Surface water-groundwater exchange in transitional coastal environments by airborne electromagnetics: The Venice Lagoon example. *Geophysical Research Letters* 37, 1, 1–6.
- Visser, M., 2012. Aquifer storage and recovery in a fossil creek bed managing droughts in a brackish environment. MSc thesis Utrecht University. Technical report, Deltares.
- Voortman, B., 2010. De invloed van gebiedseigenschappen en klimaatverandering op de dikte en vorm van regenwaterlenzen in de Provincie Zeeland.
- Voss, C.I., 2011a. Editors message: Groundwater modeling fantasies part 1, adrift in the details. *Hydrogeology Journal* 19, 7, 1281–1284.
- Voss, C.I., 2011b. Editors message: Groundwater modeling fantasies part 2, down to earth. *Hydrogeology Journal* 19, 8, 1455–1458.
- Voss, C.I. and Souza, R., 1987. Variable Density Flow and Solute Transport Simulation of Regional Aquifers Containing a Narrow Freshwater-Saltwater Transition Zone. *Water Resources Research* 23, 10, 1851–1866.
- Ward, J., Simmons, C. and Dillon, P., 2007. A theoretical analysis of mixed convection in aquifer storage and recovery: How important are density effects? *Journal of Hydrology* 343, 3-4, 169–186.
- Watson, T.A., Werner, A.D. and Simmons, C.T., 2010. Transience of seawater intrusion in response to sea level rise. *Water Resources Research* 46, 12, 1–10.
- Webb, M.D. and Howard, K.W.F., 2011. Modeling the transient response of saline intrusion to rising sea-levels. *Ground water* 49, 4, 560–9.
- Werner, A.D. and Gallagher, M.R., 2006. Characterisation of sea-water intrusion in the Pioneer Valley, Australia using hydrochemistry and three-dimensional numerical modelling. *Hydrogeology Journal* 14, 8, 1452–1469.
- Werner, A.D., Bakker, M., Post, V.E.A., Vandenbohede, A., Lu, C., Ataie-Ashtiani, B., Simmons, C.T. and Barry, D.A., 2013. Seawater intrusion processes, investigation and management: Recent advances and future challenges. *Advances in*

- Water Resources 51, 3–26.
- Werner, A.D., Jakovovic, D. and Simmons, C.T., 2009. Experimental observations of saltwater up-coning. *Journal of Hydrology* 373, 1-2, 230–241.
- White, I. and Falkland, T., 2009. Management of freshwater lenses on small Pacific islands. *Hydrogeology Journal* 18, 1, 227–246.
- WHO, 2011. Guidelines for drinking-water quality, 4th ed. Technical report.
- Wirojanagud, B.P. and Charbeneau, R.J., 1983. Saltwater Upconing in Unconfined Aquifers. *Journal of Hydraulic Engineering* 111, 3, 417–434.
- Wooding, R.A., Tyler, S.W. and White, I., 1997a. Convection in groundwater below an evaporating Salt Lake: 1. Onset of instability. *Water Resources Research* 33, 6, 1199.
- Wooding, R.A., Tyler, S.W., White, I. and Anderson, P.A., 1997b. Convection in groundwater below an evaporating Salt Lake: 2. Evolution of fingers or plumes. *Water Resources Research* 33, 6, 1219.
- Wright, L. and Short, A., 1984. Morphodynamic variability of surf zones and beaches: a synthesis. *Marine Geology* 56, 93–118.
- Xin, P., Robinson, C., Li, L., Barry, D.A. and Bakhtyar, R., 2010. Effects of wave forcing on a subterranean estuary. *Water Resources Research* 46, 12, 1–17.
- Yeh, H.D. and Chang, Y.C., 2013. Recent advances in modeling of well hydraulics. *Advances in Water Resources* 51, 27–51.
- Zhang, H., Hocking, G.C. and Barry, D.A., 1997. An analytical solution for critical withdrawal of layered fluid through a line sink in a porous medium. *Journal of Australian Mathematical Society Series B* 39, March 1996, 271–279.
- Zheng, C. and Bennett, G., 2002. *Applied Contaminant Transport Modeling*. John Wiley & Sons Ltd, 2 edition.
- Zhou, Q., Bear, J. and Bensabat, J., 2005. Saltwater Upconing and Decay Beneath a Well Pumping Above an Interface Zone. *Transport in Porous Media* 61, 3, 337–363.
- Zuurbier, K.G., Kooiman, J.W., Groen, M.M.A., Maas, B. and Stuyfzand, P.J., 2014a. Enabling Successful Aquifer Storage and Recovery of Freshwater Using Horizontal Directional Drilled Wells in Coastal Aquifers. *Journal of Hydrologic Engineering* 1–7.
- Zuurbier, K.G., Zaadnoordijk, W.J. and Stuyfzand, P.J., 2014b. How multiple partially penetrating wells improve the freshwater recovery of coastal aquifer storage and recovery (ASR) systems: A field and modeling study. *Journal of Hydrology* 509, 430–441.

